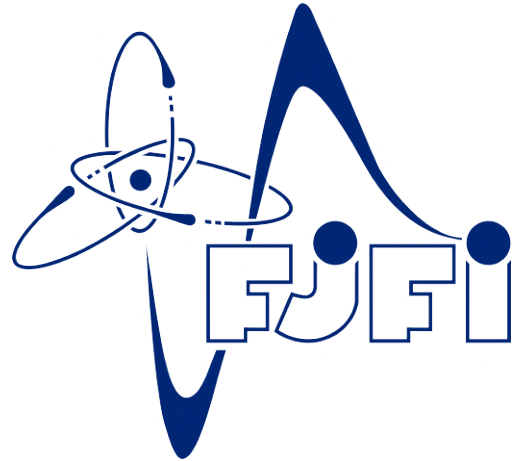# CZECH TECHNICAL UNIVERSITY IN PRAGUE

FACULTY OF NUCLEAR SCIENCES AND PHYSICAL ENGINEERING

Department of Physical Electronics
Laser Physics and Technology

MASTER'S THESIS

LASER-DRIVEN ION ACCELERATION: ANALYSIS AND THEORETICAL INTERPRETATION OF EXPERIMENTAL DATA

Author: **Bc. Arsenios Hadjikyriacou**
Supervisor: Lorenzo Giuffrida, Ph.D.
Consultant: doc. Ing. Jan Pšikal, Ph.D.

Prague, 2022

Acknowledgment

I would firstly like to thank my supervisors, Dr. Lorenzo Giuffrida and Dr. Jan Pšikal, for their invaluable guidance, patience and encouragement throughout my studies. Special thanks to Dr. Andriy Velyhan, Dr. Maksym Tryus and Dr. Vasiliki Kantarelou for sharing their expertise in TOF/TP diagnostics, lasers and CR39 detectors, respectively. Finally, I would also like to express my sincere gratitude towards the entire ELIMAIA team at ELI-beamlines for their support.

Declaration

This work has been composed solely by myself and it has not been submitted for another qualification to this or any other university. Except where stated otherwise by reference or acknowledgement, the work presented is entirely my own.

....
Date   Bc. Arsenios Hadjikyriacou

Title of thesis: **Laser-driven ion acceleration: analysis and theoretical interpretation of experimental data**

Author:	Bc. Arsenios Hadjikyriacou
Specialization:	Laser physics and technology
Type of work:	Master's thesis
Supervisor:	Lorenzo Giuffrida, Ph.D., FZÚ AV ČR, ELI-Beamlines
Consultant:	doc. Ing. Jan Pšikal, Ph.D., KFE FJFI ČVUT

Abstract: Advances in high-power laser technology seen in recent years have fueled research in the field of laser-driven ion acceleration. Laser-plasma interactions can produce short duration, high flux, high energy (tens of MeV) ion bunches with interesting properties for a range of applications. Leading the way in this rapidly growing field is the ELIMAIA group at ELI-Beamlines. The combination of ultra-high peak intensities ($> 10^{21}$ W/cm^2) and high repetition rates (up to 10 Hz) offered at the ELIMAIA beamline provides a unique tool for multidisciplinary applications of laser-accelerated ion beams. This master's thesis deals with the analysis of experimental results from the ELIMAIA commissioning, using the HAPLS laser system to accelerate protons above 10 MeV from thin foil targets. Selected ion diagnostics (time-of-flight based detectors and Thomson parabola spectrometer) are chosen to perform this analysis. Particle-in-cell (PIC) simulations are performed, with the final goal to demonstrate the experimental data and validate the acceleration mechanism relevant for this experiment. Particular emphasis is given to the effect of prepulses and rear-side preplasma in the TNSA (Target Normal Sheath Acceleration) regime, with the aim of optimizing the ion accelerator performance.

Keywords: ELIMAIA, ion diagnostics, laser-plasma, PIC, preplasma, prepulses, TNSA

Contents

This page was intentionally left blank.

Introduction

Ion acceleration driven by superintense laser pulses is attracting an impressive amount of research effort from groups all over the world. Inside laser-produced plasmas, strong electric fields are generated by a collective displacement of a large number of electrons, and such electric fields accelerate ions until charge neutrality is restored and ions move together with electrons in a ballistic way. Motivation to develop such technology stems from the potential for a number of foreseen applications, ranging from biomedical physics (e.g. hadron therapy) to nuclear and particle physics (e.g. nuclear fusion reactions). Experiments have demonstrated the generation of multi-MeV proton and ion beams with attractive properties such as ultrashort duration and high brightness. Despite significant progress in recent years, laser-driven ion acceleration remains in its infancy. A substantial amount of research and development (both on the experimental and theoretical front) still needs to be done before this technology matures to the point where it can be introduced to societal applications. The main direction proposed by the community of experts in the field of laser-driven ion acceleration is to improve particle beam features (maximum energy, emittance, divergence, monochromaticity, shot-to-shot stability) in order to demonstrate reliable and compact approaches to be used for multidisciplinary applications [1].

Leading this effort is Department 87 of FZU (Department of Ion Acceleration and Applications of High Energy Particles) based at the ELI-Beamlines facility in the Czech Republic. The mission of the laser-driven ion target area at ELI-Beamlines (Extreme Light Infrastructure) is to provide stable, fully characterized and tuneable beams of particles accelerated by Petawatt-class lasers and to offer them to the user community for multidisciplinary applications. The ion accelerator is currently in the commissioning stage. During this preliminary optimization phase, experiments aimed to demonstrate the capabilities and reliability of the beamline to the user base are performed.

This thesis is concerned with one such experiment carried out between October and December of 2021. The high-repetition-rate, high peak-power HAPLS laser system was used to accelerate ions from thin targets ($2 - 25\,\mu\text{m}$) of various compositions. The laser beam ($10\,\text{J}$, $30\,\text{fs}$) was tightly focused ($\sim 2\,\mu\text{m}$ FWHM) to reach ultrahigh intensity on target (above $10^{21}\,\text{W/cm}^2$). Protons with energy above $10\,\text{MeV}$ were detected. This work deals with characterization of the proton beams using a complete set of ion diagnostics, with emphasis on analysis of data obtained from time-of-flight diagnostics and Thomson parabola spectrometer. The aim of this analysis is to provide deeper understanding into the laser-plasma interaction and suggest improvements in order to optimize the performance of the ion accelerator for future experiments. This information is also used to design and perform 2D particle-in-cell simulations to validate the experiment and confirm TNSA (Target Normal Sheath Acceleration) as the acceleration mechanism. Finally, this work examines in detail the effect of prepulses on solid targets and, specifically, the effect of rear-side plasma formation on the efficiency of TNSA. Both the experimental results and the simulations bear witness to the competing effects of target thickness and rear-side plasma. In fact, it is verified that even short length plasma on the target rear has a detrimental impact on ion acceleration.

This thesis is divided into four parts. The first chapter studies the basic theory of laser-driven ion acceleration relevant to the experiment, with special emphasis on electron heating in preplasma and the TNSA mechanism. In addition, the effect of laser prepulses on solid targets is explained with reference to previous publications. Chapter two is an introduction to the particle-in-cell method for laser-plasma simulations. The relevant mathematical relations are provided and the basic structure of the PIC algorithm is laid out. Chapter three provides a brief overview of the ELIMAIA beamline, including diagnostics for ions accelerated by laser, with more detailed information about selected diagnostics. Finally, chapter four deals with the analysis of experimental data and presentation of results from the commissioning experiment. As part of this final chapter, the results of particle-in-cell simulations relevant for the experiment are presented, followed by discussion concerned with the theoretical interpretation of the experiment (acceleration mechanism, effect of target thickness and prepulses, etc.).
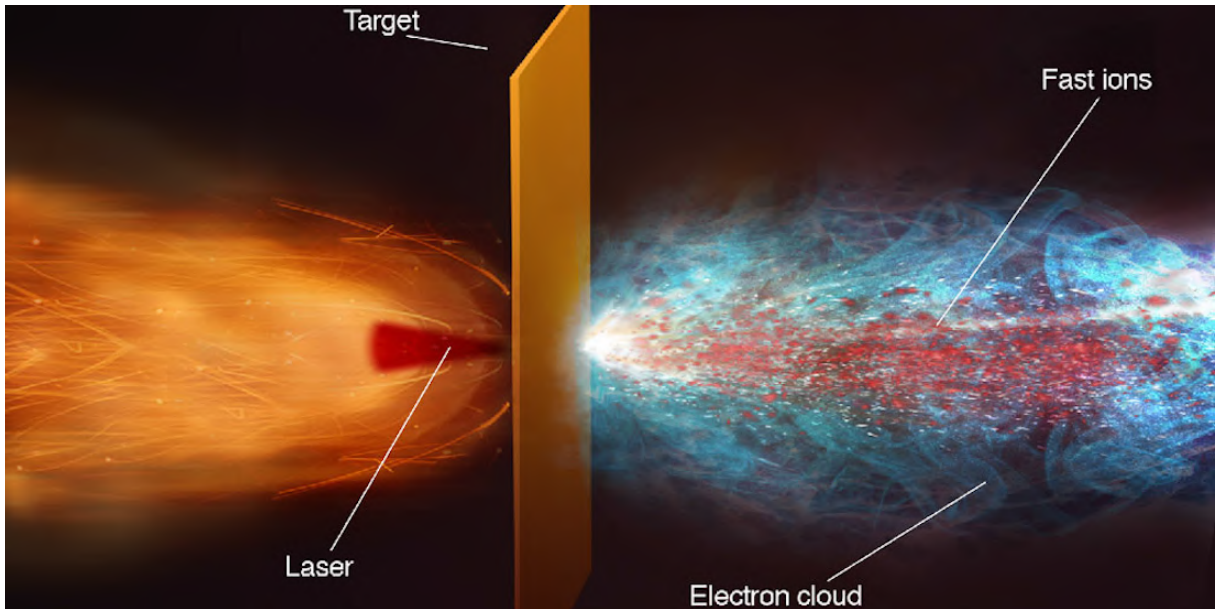

Figure 1: Artist's view of ion acceleration from laser-irradiated solid targets [2].

Chapter 1

Theory of Laser-Solid Interaction at Relativistic Intensities

This chapter will provide the theoretical background of the interaction between an intense laser beam and a solid target, which ultimately leads to ion acceleration. We will first discuss how a laser pulse can ionize matter to produce plasma. Then we will consider the properties of plasmas (both microscopic and macroscopic), the processes that allow them to absorb laser energy and, finally, the mechanisms by which the absorbed energy can be transferred to the ions in the process of ion acceleration. The following material is focused towards interactions at relativistic intensities ($I > 10^{18}\,\mathrm{Wcm^{-2}}$) using petawatt laser systems. However, we also attempt to briefly summarize phenomena which can only be observed using lower intensities ($I < 10^{15}\,\mathrm{Wcm^{-2}}$) often encountered in prepulses.

1.1 Ionization of matter by laser light

The photon energy of a high-power laser is usually too low to ionize the material directly. As an example, laser light of wavelength $\lambda = 1030\,\mathrm{nm}$ corresponds to a photon energy of $1.2\,\mathrm{eV}$, which is lower than the first ionization energy of any element. Fortunately, at high intensities alternative processes are possible, namely multiphoton ionization (MPI) and field ionization. These processes are illustrated in figure 1.1. We now introduce the Keldysh parameter γ_k [3], which distinguishes the ionization regimes:

$$\gamma_k = \omega\sqrt{\frac{2E_{ion}}{I}} = \sqrt{\frac{E_{ion}}{2\Phi_p}} \quad , \tag{1.1}$$

where ω, I, E_{ion} and Φ_p are the laser frequency, laser intensity, ionization potential and ponderomotive potential, respectively [4]. Generally, tunneling is more dominant for strong fields and long wavelengths (i.e. for $\gamma_k < 1$) while multiphoton ionization applies for weaker fields with a higher frequency (i.e. for $\gamma_k > 1$).

An electron is released from an atom if it absorbs enough energy to transition from a bound state to the continuum. The first free electrons can be produced by multiphoton ionization (MPI). MPI is a non-linear process which takes place by simultaneous absorption of $N \geq E_{ion}/\hbar\omega$ photons. Its probability is strongly dependent on the intensity as $P_n \simeq \sigma_N(I_L)^N$ [6]. The cross-section, σ_N, decreases with increasing N but the intensity dependence ensures that an Nth order ionization event will occur provided that the intensity is high enough. A related phenomenon is known as above-threshold ionization (ATI), where the electron absorbs more photons than is necessary for ionization.

After the first free electrons are released, the process of collisional or electron ionization can start. Electrons oscillate in response to an electromagnetic wave and occasionally collide with atoms and knock an electron out, losing some energy in the process. When
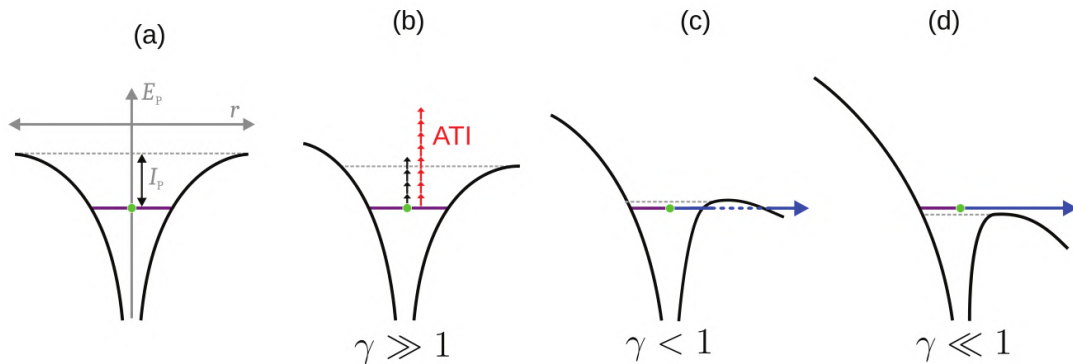
Figure 1.1: The atomic Coulomb potentials under the influence of intense laser fields are shown for the (a) field free, (b) multiphoton ionization, (c) tunnel ionization, and (d) over-the-barrier ionization cases [5]. The symbol γ refers to the Keldysh parameter.

the laser intensity exceeds a certain threshold value, an avalanche process begins, plasma is formed rapidly and a considerable number of free electrons is released.

The final ionization mechanism is field ionization. This refers to the distortion of the Coulomb field by a strong laser field, to the point the electron can escape the potential well. In this case, the laser field is strong enough to partially or totally depress one side of the potential well lower than the binding energy of the electron. Then the electron either can tunnel out (figure 1.1(c)) of the well or, when the whole barrier drops below the ionization potential, the electron can leave the nucleus even classically (figure 1.1(d)).

1.2 Fundamental concepts of laser-plasma physics

Plasma is a quasi-neutral system of charged particles (electrons and ions) that exhibit collective behavior. It follows that electromagnetic fields can couple strongly to plasma and influence its evolution. On a macroscopic level, certain plasma parameters (such as particle density and temperature) provide a straightforward description. However, we can gain deeper understanding of the underlying physics by first considering microscopic quantities and processes.

1.2.1 Single electron motion in electromagnetic field

The relativistic equations of motion for an electron in an electromagnetic (EM) field are[1]:

$$\frac{d\mathbf{p}}{dt} = -e[\mathbf{E}(\mathbf{r}, t) + \mathbf{v} \times \mathbf{B}(\mathbf{r}, t)] \quad ; \quad \mathbf{p} = \gamma m_e \mathbf{v} \quad , \tag{1.2}$$

where $\gamma = [1 - \mathbf{v}^2/c^2]^{-1/2} = [1 + \mathbf{p}^2/(m_e c)^2]^{1/2}$ is the Lorentz factor. An important figure-of-merit for laser-electron interaction is the dimensionless parameter a_0 defined as

$$a_0 = \frac{eE_0}{m_e \omega c} = \frac{eA_0}{m_e c} \propto \sqrt{I\lambda^2} \quad . \tag{1.3}$$

In the classical limit of an electron oscillating in an electric field of frequency ω and amplitude E_0, this parameter (known as dimensionless amplitude) is the peak electron momentum divided by $m_e c$ or, equivalently, the ratio of the peak electron oscillation velocity to the speed of light, i.e. v_0/c. It is a convenient measure of the importance of relativistic effects: the relativistic regime of laser-plasma interaction may be defined by the condition $a_0 > 1$, when the electric field drives the electrons close to the speed of light. In this regime the magnetic part of the Lorentz force ($\mathbf{v} \times \mathbf{B}$) cannot be ignored.

[1]Radiation reaction (force on charges due to acceleration-induced radiation emission) not included.

The relativistic motion of an electron in a monochromatic, plane-polarized wave is known to have analytical solutions [4]. Consider a plane EM wave (frequency ω) propagating in the z direction and an electron initially at rest in the lab frame. The plane wave can be described by the vector potential of the form

$$\mathbf{A}(t) = \frac{m_e c}{e} a_0 \left[\delta \cos \omega\tau \, \hat{\mathbf{x}} + \sqrt{1 - \delta^2} \sin \omega\tau \, \hat{\mathbf{y}} \right] \quad , \tag{1.4}$$

where $\tau \equiv t - z(t)/c$, the parameter δ determines the polarization state of the light (1 for linear and $1/\sqrt{2}$ for circular polarization) and $\mathbf{E} = \partial_t \mathbf{A}$, $\mathbf{B} = \nabla \times \mathbf{A}$. With the electron being initially at rest, the following relations are valid in the lab frame:

$$\mathbf{p}_\perp = e\mathbf{A} \quad ; \quad p_z = \frac{\mathbf{p}_\perp^2}{2m_e c} \quad . \tag{1.5}$$

Furthermore, using the definition of relativistic momentum $\mathbf{p} = m_e \gamma \, \mathbf{v} = m_e \gamma \, d\mathbf{r}/dt$, one can show that $\mathbf{p} = m_e \, d\mathbf{r}/d\tau$. Finally, integrating the last equation with respect to τ, we can obtain expressions for the trajectory of the electron:

$$kz = \frac{a_0^2}{8} \left[2\omega\tau + (2\delta^2 - 1) \sin 2\omega\tau \right] , \tag{1.6}$$

$$k\mathbf{r}_\perp = a_0 \left[\delta \sin \omega\tau \, \hat{\mathbf{x}} + \sqrt{1 - \delta^2} \left(1 - \cos \omega\tau \right) \hat{\mathbf{y}} \right] . \tag{1.7}$$

The angle θ between the trajectory and the z direction is given by $\tan \theta = \sqrt{2/(\gamma - 1)}$. Equation (1.6) for the longitudinal motion of the electron contains a term that increases linearly with time and an oscillatory term of frequency 2ω. By averaging this equation over one cycle, we obtain the drift velocity of the oscillation center as

$$v_d = \left(\frac{a_0^2}{a_0^2 + 4} \right) c \quad . \tag{1.8}$$
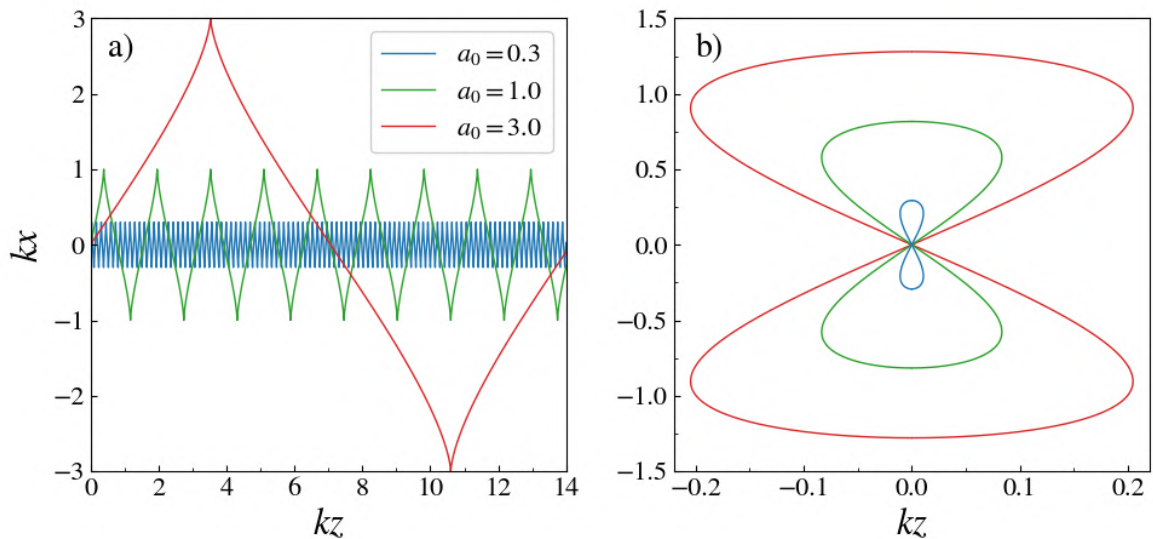
Figure 1.2: Free electron trajectories in the EM field of a linearly-polarized plane wave in: a) the lab frame and b) the moving frame with drift velocity v_d along the z direction. For a $1\,\mu$m laser wavelength, the dimensionless amplitudes $a_0 = 0.3, 1, 3$ correspond roughly to intensities of 10^{17}, 10^{18} and 10^{19} W/cm^2, respectively. In a) $\sim$ 100, 10 and 1 field periods of the electron motion are displayed for the same values of a_0.

Figure 1.2 is a picture of the electron motion in the case of linear polarization both in the lab frame and a Lorentz boosted frame co-moving with the oscillation center. For low field strength ($a_0 \ll 1$) the electron is mainly driven by the electric field and oscillates with frequency ω in the transverse direction ($x-y$ plane), with little longitudinal displacement. As the field strength increases ($a_0 \gtrsim 1$), the electron oscillation velocity approaches the speed of light and therefore the $\mathbf{v} \times \mathbf{B}$ force starts to become significant. To lowest order, this magnetic force points in the longitudinal direction and contains both a term oscillating with frequency 2ω and a constant term. As a result, the electron performs fast oscillations about a point that drifts with constant velocity in the z direction. For linear x polarization, the electron trajectory (in the frame co-moving with the oscillation center) is a "figure of 8" in the $x-z$ plane. For circular polarization, the fast $\mathbf{v} \times \mathbf{B}$ oscillations (sinusoidal term in equation (1.6)) are completely suppressed and the electron moves with constant velocity v_d in the z direction, tracing a helical path in space. However, such solutions also predict that, if the EM field is suddenly "switched-off", the electron should be found to be in its initial momentum state (i.e. at rest) but its final position in space can be different. This is a statement of the Lawson-Woodward theorem, which hypothesizes that a charge cannot be accelerated by a radiation field in vacuum extending over an infinite region (i.e. plane wave).

Nevertheless, electron acceleration in vacuum is indeed possible by violating one or more assumptions of the Lawson-Woodward theorem. For instance, the use of focused laser pulses in experiments means that the fields are space and time-limited. In such cases the electron acceleration may be well described using the concept of the Ponderomotive Force (PF). If we assume that the pulse envelope varies with time on a scale slower than the laser period, then we can describe the electron motion on two separate time scales. The PF is the slowly-varying, non-linear, effective force describing the cycle-averaged motion of the oscillation center of a charged particle in a non-uniform laser field, over a time scale longer than the laser period. The PF is given by the negative gradient of the ponderomotive potential Φ_p. In its non-relativistic form, the ponderomotive force and ponderomotive potential (for electrons) can be expressed as

$$\mathbf{F}_p = -\frac{e^2}{4m_e\omega^2}\nabla\langle E_0^2\rangle \quad ; \quad \Phi_p = \frac{e^2 E_0^2}{4m_e\omega^2} = \frac{2e^2}{c\epsilon_0 m_e}\frac{I}{4\omega^2} = \frac{a_0^2}{4}m_e c^2 \quad . \tag{1.9}$$

Note that this force is directed opposite to the intensity gradient. This means that when a laser beam propagates in plasma, electrons along its path feel a force pushing them away (either radially outward from the beam or in front of the beam). It is clear that this force is more effective at higher laser intensity because of the dependence on the gradient of amplitude squared. Moreover, the $1/m$ mass dependence favors electron acceleration. For relativistic intensities the ponderomotive force and potential take the shape

$$\mathbf{F}_p^r = -m_e c^2 \nabla\langle\gamma\rangle \quad ; \quad \Phi_p^r = m_e c^2(\langle\gamma\rangle - 1) \quad , \tag{1.10}$$

where $\langle\gamma\rangle \equiv \sqrt{1 + a_0^2/2}$. It is interesting to note that the PF is closely related to radiation pressure. In fact, in the case of normal incidence on a flat surface, the cycle-averaged value of the $\mathbf{v} \times \mathbf{B}$ force is the steady PF density on electrons, which is connected to the total radiation pressure on the surface [2, 7].

1.2.2 Basic plasma parameters

Plasmas have the ability to shield electric fields due to their quasi-neutrality and high conductivity. The length-scale associated with this shielding is known as Debye length, λ_D. Inside a plasma, the Coulomb potential of a point charge q is shielded over distances longer than the Debye length by a shielding cloud (known as the Debye sphere) of

approximate radius λ_D that consists of equal charge of the opposite sign. Using the Poisson equation and assuming the electrons to be in thermal equilibrium at temperature T_e, the Debye length for electrons can be expressed as

$$\lambda_D = \sqrt{\frac{\epsilon_0 k_B T_e}{e^2 n_e}} \quad \Rightarrow \quad N_D = \frac{4\pi}{3}\lambda_D^3 n_e \quad , \tag{1.11}$$

where n_e is the electron density. The plasma parameter, N_D, is a dimensionless parameter equal to the typical number of electrons contained in a Debye sphere. A fundamental timescale in plasma physics is the plasma frequency. This frequency corresponds to the natural electrostatic oscillation frequency of an electron in response to a small charge separation. Ions are naturally immobile on the time scale of the electron plasma frequency (due to their much higher mass and inertia). The electron plasma frequency, ω_p, is the fastest and is usually referred to simply as plasma frequency [8]

$$\omega_p = \sqrt{\frac{n_e e^2}{m_e \epsilon_0}} \quad . \tag{1.12}$$

For an ideal plasma ($N_D \gg 1$), the Debye sphere is densely populated and Coulomb scattering to small angles dominates large angle scattering. In this regime, the collision frequency, ν, is the inverse of the mean time required for the trajectory of a particle to undergo a major angular change ($> 90°$) due to multiple Coulomb collisions with other particles. For this reason, the collision frequency is sometimes referred to as the $90°$ scattering rate. The most common collisions are those between electrons and ions. Electron-ion collisions occur with a frequency

$$\nu_{ei} = \tau_c^{-1} = \frac{4\sqrt{2}}{3}\frac{Z_i^2 e^4 n_i \ln\Lambda}{(k_B T_e)^{3/2} m_e^{1/2}} \propto \frac{Z_i^2 e^4 n_i \ln\Lambda}{m_e^2 \mathrm{v}_e^3} \propto \frac{1}{\mathrm{v}_e^3} \propto \frac{1}{T_e^{3/2}} \quad , \tag{1.13}$$

where $\Lambda = b_{max}/b_{min} = \lambda_D/l_{ca}$, with b being the impact parameter and $l_{ca} = Ze^2/k_B T_e$ the classical distance of the closest electron-ion approach. The quantity $\ln\Lambda$ is known as the Coulomb logarithm [9]. Energy is transferred mainly in collisions of particles of the same type. Therefore, collisions between electrons and ions lead to only a small energy transfer to the ions because of the big mass difference. This means that collisions change the direction of electron motion without significantly affecting the electron energy. Finally, it can be inferred from equation (1.13) that at higher intensities the plasma becomes effectively "collisionless" since the velocity amplitude of electron oscillations increases with field strength and significant electron heating occurs.

1.2.3 Laser propagation in plasma

Consider a simple model where the plasma is infinite and homogeneous, the ions are infinitely heavy (i.e. their motion can be neglected) and no static magnetic or electric fields are present. We are only interested in the macroscopic motion because it contributes to the current density, while the thermal motion does not. Therefore, (neglecting thermal motion) the equation of an electron fluid is:

$$\frac{d\mathbf{v}}{dt} = -\frac{e\mathbf{E}}{m_e} - \frac{\mathbf{v}}{\tau_c} \quad , \tag{1.14}$$

where τ_c is the effective time between electron-ion collisions and $\mathbf{v}$ is the speed of the ordered motion of the fluid. If we solve the equation of motion (1.14) together with Maxwell's equations for a harmonic, monochromatic plane wave of frequency ω propagating in a homogeneous medium (i.e. the wave-vector amplitude, $k = 2\pi/\lambda$, is constant), we find the following dispersion relation

$$k^2 = \frac{\omega^2}{c^2} - \frac{\omega_p^2 \omega}{c^2(\omega + i\nu_{ei})} \tag{1.15}$$

In the absence of collisions, the dispersion relation reduces to

$$k^2 c^2 = \omega^2 - \omega_p^2 \quad \Rightarrow \quad n = \sqrt{1 - \left(\frac{\omega_p}{\omega}\right)^2} \quad, \tag{1.16}$$

where n is the refractive index at frequency ω in a collisionless plasma. Note that n implicitly depends on intensity through the plasma frequency ω_p and the relativistic electron mass ($m_e \to \gamma\, m_e$) in equation (1.12). The refractive index has a real solution only if $\omega \geq \omega_p$. In this regime, the plasma is transparent (known as underdense plasma) and an EM wave can propagate inside the plasma. In the opposite case when $\omega < \omega_p$, the plasma is opaque (known as overdense plasma) and the wave cannot propagate. Instead, the electric field inside the plasma is exponentially attenuated and penetrates over the skin depth, while the laser wave is reflected at the critical density (for normal incidence). The critical density is defined by $\omega = \omega_p$ and it can be expressed as

$$n_c = \frac{\epsilon_0 m_e \omega^2}{e^2} \quad \Rightarrow \quad n = \sqrt{1 - \frac{n_e}{n_c}} \quad. \tag{1.17}$$

It terms of n_c, the two regimes are: $n_e < n_c \Rightarrow$ underdense and $n_e \geq n_c \Rightarrow$ overdense. A non-linear phenomenon known as relativistically-induced transparency can occur when a relativistic laser pulse is incident on a classically overdense plasma. The relativistic laser pulse raises the critical density above its classical value ($m_e \to \gamma\, m_e \Rightarrow n_c \to \gamma\, n_c$) and above the local electron density, which allows the pulse to propagate through a relativistically underdense plasma.

Another interesting non-linear effect than can occur during propagation of relativistic pulses through underdense plasma is self-focusing. Self-focusing of light is the process in which an intense beam of light modifies the optical properties of plasma in such a manner that the beam is caused to come to a focus within the plasma [10]. More specifically, self-focusing is observed when a laser beam induces a refractive index variation within the plasma, with a larger refractive index at the center of the beam than at its periphery. The plasma thus acts as if it were a positive lens. In terms of ω_p, this corresponds to lower value at the center compared to the periphery (cf. equation (1.16)). Due to the Gaussian transverse structure of typical laser beams, self-focusing can arise either by ponderomotive or relativistic effects. Ponderomotive self-focusing occurs because of the expulsion of electrons from the center of the beam, lowering the electron density (and consequently the plasma frequency, cf. eqn. (1.12)) in the center. Relativistic self-focusing occurs because the high intensity at the beam center drives electrons close to the speed of light and therefore increases their relativistic mass γm_e (lowers the plasma frequency, cf. eqn. (1.12)) in the center. An important parameter is the critical power [7] given by

$$P_c = 17.5 \left(\frac{\omega}{\omega_p}\right)^2 \text{ GW} \quad. \tag{1.18}$$

For $P = P_c$ the beam is self-guided, whereas for $P > P_c$ and $P < P_c$ the beam is expected to self-focus and to diffract, respectively. In the case where $P \gg P_c$, the beam can breakup into many filaments (beam breakup or filamentation), each filament carrying a power of approximately P_c. Self-focusing can take place in the expanded preplasma on the front side of a solid target, thus increasing the effective intensity on the target surface.

1.3 Laser absorption and hot electron generation

As noted in the previous section, the laser pulse interacts mostly with electrons. In this section, we describe the mechanisms responsible for laser energy absorption to plasma electrons for originally solid targets. This is important because the temperature of hot electrons determines the cutoff energy of protons accelerated from the rear side of the target in the TNSA mechanism (section 1.4.1). The absorption starts from low intensity prepulses ($I \sim 10^{12} - 10^{16}\,\mathrm{W/cm^2}$). At this stage, it is dominated by inverse bremsstrahlung (also known as collisional absorption) and resonant absorption. Inverse bremsstrahlung becomes ineffective at higher intensities but the main laser pulse ($I > 10^{18}\,\mathrm{W/cm^2}$) can be absorbed by several other mechanisms. In the presence of preplasma, stochastic heating and direct laser acceleration (DLA) are the dominant absorption mechanisms [11]. For steep density gradients, vacuum heating becomes important, and for even higher relativistic intensities $\mathbf{J} \times \mathbf{B}$ heating is effective [12].

1.3.1 Resonant absorption

It can be shown that a linearly polarized EM wave with oblique incidence on expanded plasma will be reflected before the critical density is reached, at $n_e = n_c \cos^2 \theta_{in}$ depending on the angle of incidence. However, there will be an exponentially decaying evanescent field extending even deeper into the plasma. A p-polarized wave has an electric field z-component in the direction of the density gradient and can therefore separate negative and positive charges. At the turning point, the electric field component of the incident wave resonantly excites a standing electron plasma wave oscillating in the target-normal direction. The wave grows over a number of laser periods and is eventually damped by collisions (at low intensities) or particle trapping (at high intensities). These waves can accelerate a number of hot electrons which are pushed into the target. Using the correct laser polarization and angle of incidence, the absorption efficiency of this process can be as high as 50%. For s-polarization, the electric field points parallel to the target surface (perpendicular to density gradient) and no resonance occurs since the field cannot couple to the longitudinal plasma waves [4].
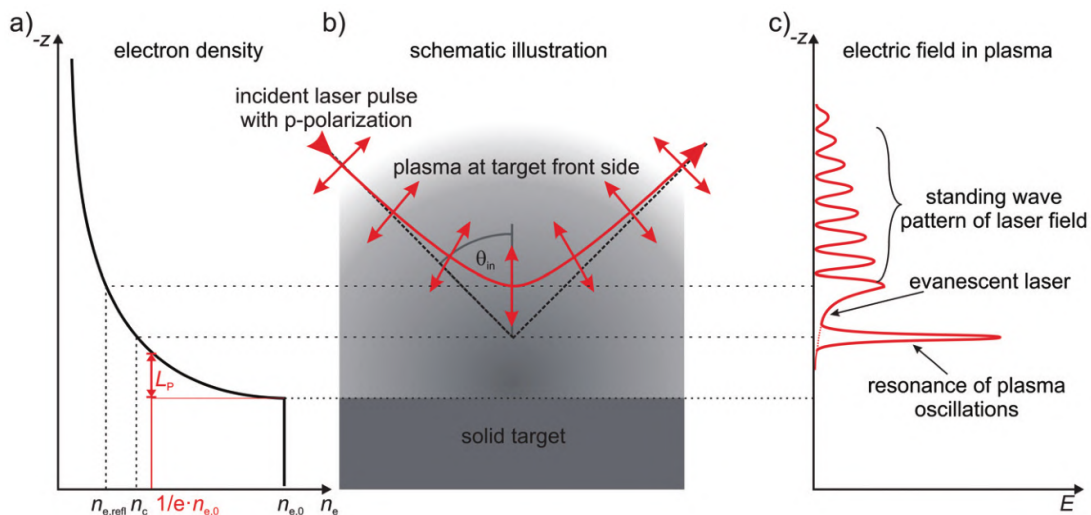

Figure 1.3: Reflection at an exponential plasma profile and resonance absorption. A p-polarized laser pulse obliquely incident on preplasma at the target front side. Reflection occurs before the critical density has been reached. The electron density profile is taken to be exponential with scale-length L_p [13].

1.3.2 Vacuum heating

This mechanism (also known as Brunel's mechanism) was first proposed by Brunel [14] in 1987. When a p-polarized laser field is incident obliquely on a sharply bounded overdense plasma, electrons near the surface will be directly exposed to the laser field. A thermal electron arriving near the edge at the right moment in the laser cycle may be dragged out violently into the vacuum by the electric field. As the field reverses its direction, the electron will be turned around and accelerated back into the plasma. Because the plasma is highly overdense, the electric field only penetrates to a skin depth, so the electron can continue traveling freely into the target [4].
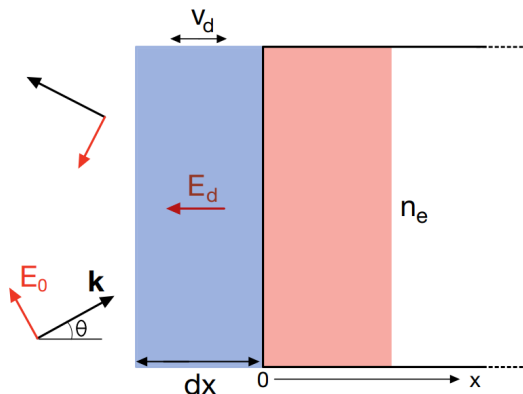

Figure 1.4: Capacitor model of the Brunel heating mechanism [4].

The Brunel model is based on the capacitor approximation ($\mathbf{v} \times \mathbf{B}$ force neglected). For oblique incidence of a p-polarized wave, a standing wave will be set up due to interference between the incident and reflected waves. The field amplitude in the standing wave is given by $E_d = 2E_0 \sin\theta$. This field pulls a sheet of electrons out to a distance dx. When the charge sheet returns to its original position, it will have acquired a velocity $v_d \simeq 2v_o \sin\theta$, where v_o is the electron oscillation velocity in the laser field. Using v_d, the hot electron temperature is thus found to be:

$$T_h^B = m_e v_d^2/2 \simeq 3.7\, I_{16}\lambda_\mu^2 \text{ keV} \quad . \tag{1.19}$$

1.3.3 Relativistic $\mathbf{J} \times \mathbf{B}$ heating

Physically, $\mathbf{J} \times \mathbf{B}$ heating is very similar to the Brunel mechanism, in the sense that electrons are directly accelerated by a laser field incident on a step-like density profile. The main difference is that the driving term is the high-frequency $\mathbf{v} \times \mathbf{B}$ component of the Lorentz force, which oscillates at 2ω. This high-frequency component leads to heating in an analogous fashion to the component of a p-polarized electric field parallel to the density gradient. $\mathbf{J} \times \mathbf{B}$ heating works for any polarization apart from circular, is most efficient for normal incidence and becomes significant at relativistic intensities.

It is interesting to note that the cycle-average of the $\mathbf{v} \times \mathbf{B}$ force is, in fact, the ponderomotive force which can also accelerate electrons. Therefore, if we want to avoid the heating by the high-frequency component, we can simply use circular polarization at normal incidence (cf. section 1.2.1). Several experimental observations and numerical simulations suggest that the typical order of magnitude of the fast electron temperature at relativistic intensities is of the order of the ponderomotive energy[2], Φ_p^r (1.10) [15, 16]:

$$T_h^P \simeq \Phi_p^r = m_e c^2 \left(\sqrt{1 + a_0^2/2} - 1 \right) \quad . \tag{1.20}$$

---

[2]This gives the so-called ponderomotive hot electron temperature scaling which is an assumption used by many scientists in the field of relativistic laser-plasma physics.

1.3.4 Stochastic heating and Direct Laser Acceleration

When preplasma is present, the laser energy coupling to hot plasma electrons is explained mostly by two mechanisms: stochastic heating or Direct Laser Acceleration (DLA) [11]. These mechanisms have been studied in numerous publications with the aid of PIC simulations [11, 17, 18, 19].

Relativistically intense laser pulses can form channels in sub-critical density plasma (by ponderomotive expulsion of electrons) and can accelerate electrons trapped in these channels in the process known as Direct Laser Acceleration (DLA). This coupling requires strong self-generated static electric and magnetic fields confining fast electrons in these plasma channels. A relativistic electron trapped in the channel oscillates radially at the betatron frequency ω_β due to the static fields. These oscillations are along the laser polarization, and thus efficient energy coupling with laser radiation is possible. An electron moving along the laser propagation direction with velocity v_x experiences a downshifted optical frequency. This shift can be so strong that the oscillations are in phase with the laser field at the electron position when the condition $\omega_\beta = (1 - v_x/v_{ph})\omega_0$ is satisfied. This is the inverse of the free electron laser mechanism [17, 18]. The resonance between electron betatron oscillations and the transverse laser field is shown in figure 1.5 below. As a result of the driven electron oscillation, there is a net energy gain each laser cycle.
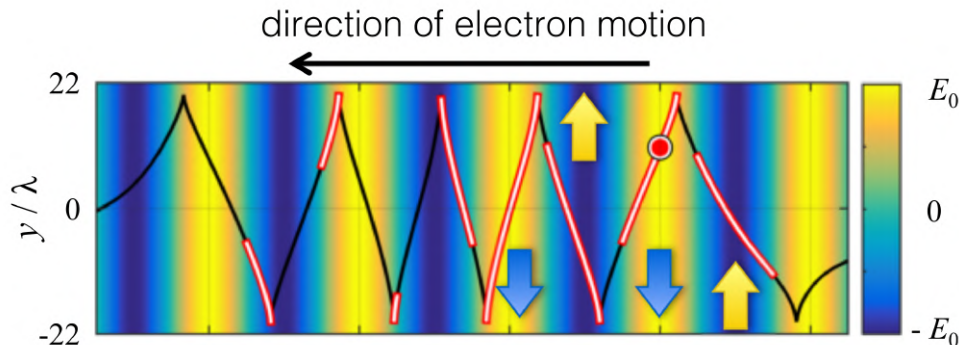

Figure 1.5: Trajectory of an electron irradiated by a plane wave with $a_0 = 11.5$ inside a sub-critical plasma channel. The color coding is the amplitude of the laser electric field in the y-direction. The arrows show the direction of the transverse electron velocity along the trajectory. The static channel fields cause betatron oscillations of the transverse electron velocity, allowing it to remain anti-parallel to the laser electric field over extended segments of the electron trajectory marked with white [19].

Stochastic heating is a chaotic effect which is responsible for the acceleration of electrons by the transverse electric field. This process only occurs in underdense preplasma where there is superposition of the incident and reflected waves, forming a standing wave pattern. Electrons are accelerated by the electric field of the standing wave and oscillate in the transverse direction while the magnetic field of the standing wave turns the motion into the longitudinal direction. This results in a chaotic sequence of accelerations and decelerations. PIC simulations have shown [11] that the net effect is a gain in momentum in the longitudinal direction. The final momentum gain is a result of several pushes by the standing wave field during propagation towards the overdense target. The energy that can be achieved by stochastic heating depends on the pulse length and the preplasma scale-length. Long interaction length between electrons and the standing wave favors higher electron energies. PIC simulations have demonstrated that the presence of preplasma and stochastic heating can significantly enhance hot electron temperature compared to the case of a target with steep front side density profile [11, 20]. It is a well known fact that in preplasma, hot electrons can be heated above the ponderomotive scaling (equation (1.20)) by stochastic (chaotic) heating and direct laser acceleration.

1.4 Ion acceleration regimes

As noted in the preceding sections, the laser field mainly transfers energy to electrons. However, the plasma electrons can mediate the forces of laser fields on ions by generation of quasi-static, collective EM fields arising from local charge separation [21]. The dominant physical process responsible for ion acceleration strongly depends on the specific laser and target parameters in the interaction under investigation (laser intensity, laser wavelength, target material composition and target geometry). In the process of solid-target irradiation by a powerful laser, the ion acceleration occurs in the following modes: in the electric field of charge separation on the target surface, by the radiation pressure of a strong EM wave and via the Coulomb explosion [22]. The focus of this chapter will mainly be the first of these modes, known as Target Normal Sheath Acceleration (abbreviated as TNSA).
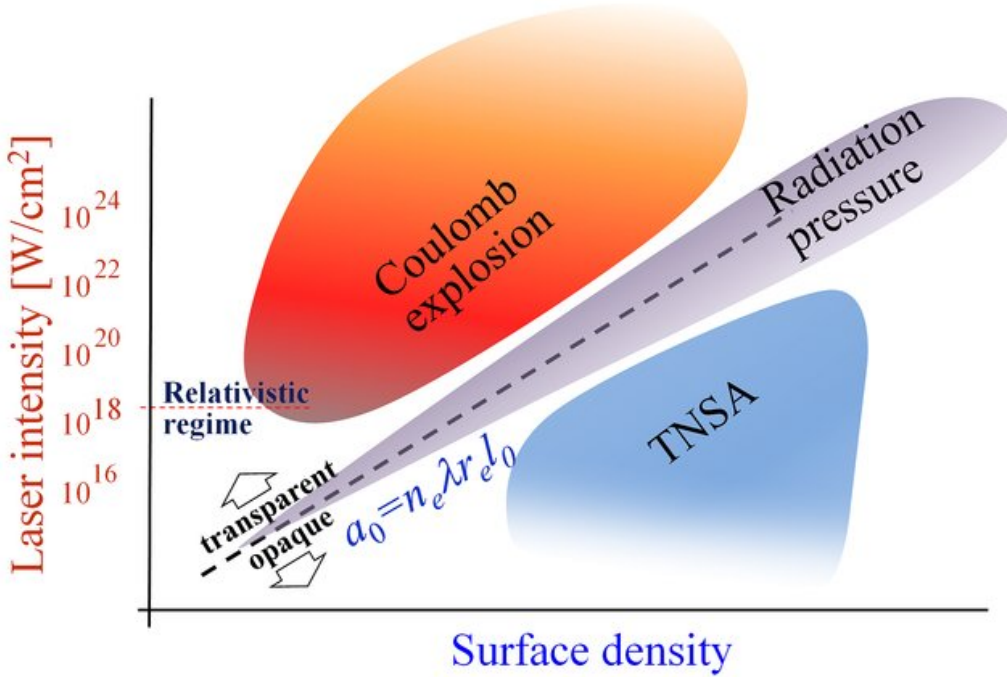

Figure 1.6: The ion acceleration regimes in the plane of the laser intensity, I, and the surface density of the target, $n_e l_0$ [23].

These modes are shown on the plane of the laser intensity and the target surface density, $n_e l_0$, in figure 1.6. Here, n_e and l_0 are the electron density and thickness of the target, respectively. The dashed line $a_0 = n_e \lambda r_e l_0$ (where $r_e = e^2/m_e c^2$ is the classical electron radius) separates the intensity-surface density plane into two domains. Below the line, plasma is opaque; above the line, plasma is relativistically transparent.

When the laser radiation interacts with an opaque target, a small sub-population of hot electrons can escape, forming a sheath with a strong electric charge separation on the target rear. The corresponding electric field accelerates ions in the Target Normal Sheath Acceleration (TNSA) regime (subsection 1.4.1). At the opaqueness-transparency threshold, the optimal conditions for Radiation Pressure-Dominated Acceleration (RPDA) are realized (subsection 1.4.2). Above the dashed line, the laser radiation is so intense that it blows out almost all electrons from the irradiated cluster target. The remaining positive ions undergo rapid expansion, known as Coulomb explosion (subsection 1.4.2), due to the repulsive forces.

1.4.1 Target Normal Sheath Acceleration

The TNSA model, originally proposed by Wilks et al. in 2001 [24], has been the most extensively studied ion acceleration mechanism in the last two decades. In TNSA, hot electrons (section 1.3) accelerated at the front side cross the bulk of the target and enter the vacuum region at the rear side, where a charged sheath (of length scale λ_D) is formed. This creates a space charge electric field, $E \sim T_h/\lambda_D$, which can reach values of the order of TV/m [25]. The electric field in the sheath is perpendicular to the target surface and back-holds electrons while accelerating ions outwards [7].
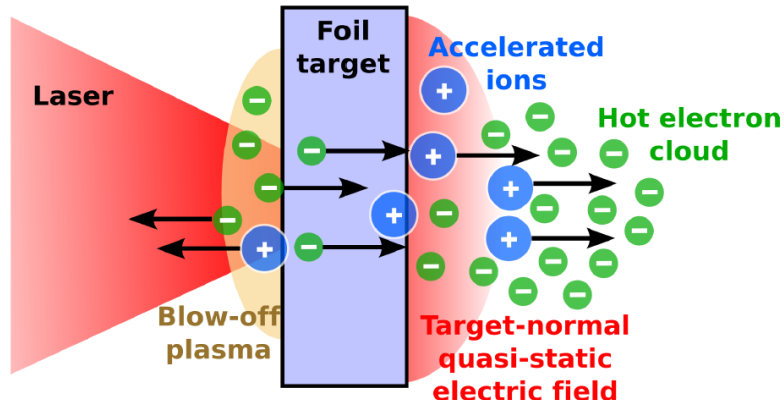

Figure 1.7: Ion acceleration in the target rear-surface layer. A possible prepulse creates a plasma corona on the target's front side. The main laser pulse generates hot electrons at the front side, which penetrate through the dense target. The acceleration of ions in the rear-surface layer occurs in the electric field which is generated by the fast electrons [26].

We can use a 1D hydrodynamic approach to describe the ion acceleration. This model is based on collisionless, isothermal expansion (in vacuum) of a plasma composed of two mutually attracting fluids, a one-temperature electron population and a single ion species (charge state Z). We make the additional assumption that the plasma is locally neutral, i.e. the relation $n_e = Zn_i$ must hold for all times on length scales bigger than the local Debye length. At time $t = 0$, the plasma is assumed to occupy the half-space $z < 0$. The ions are cold and initially at rest with density $n_i = n_{i0}$ for $z < 0$ and $n_i = 0$ for $z > 0$, with a sharp boundary. On the other hand the electron density is assumed to follow the Boltzmann distribution $n_e = n_{e0}\exp(e\phi/T_h)$ [27], where ϕ is the electrostatic potential. Then, the ion acceleration is governed by the equations of continuity and motion:

$$\left(\partial_t + u_i\partial_z\right)n_i = -n_i\partial_z u_i \quad , \tag{1.21}$$

$$\left(\partial_t + u_i\partial_z\right)u_i = -\partial_z\phi\left(Ze/m_i\right) = -c_s^2\partial_z n_i/n_i \quad , \tag{1.22}$$

where $c_s = \sqrt{ZT_h/m_i}$ is the ion-acoustic velocity. Careful analysis performed by Mora in 2003 [27] demonstrated that we can obtain approximate asymptotic solutions for the ion front velocity and field as

$$E_f \simeq 2E_0/(2e + \omega_{pi}^2 t^2)^{1/2} \quad , \tag{1.23}$$

$$u_f \simeq 2c_s \ln\left(\tau + \sqrt{\tau^2 + 1}\right) \quad , \tag{1.24}$$

where $\tau \equiv \omega_{pi}t/\sqrt{2e}$, $E_0 = (n_{e0}T_h/\epsilon_0)^{1/2}$, ω_{pi} is the ion plasma frequency and e is the euler constant. Finally, the high-energy cut-off in the energy spectrum for $\omega_{pi}t \gg 1$ is

$$\mathcal{E}_{max} \simeq 2\,Z\,T_h\,[\ln(2\tau)]^2 \quad , \tag{1.25}$$

where the expansion time, t, is often taken to be equal to the laser pulse duration.

Equation (1.25) shows that the maximum energy per charge state with the hot electron temperature, T_h. If we assume the ponderomotive hot electron temperature scaling and using the fact that $a_0 \propto \sqrt{I\lambda^2}$, we find that the maximum ion energy scaling for TNSA is $\mathcal{E}_{max} \propto \sqrt{I\lambda^2}$. In reality, empirical scaling laws from experimental data of the form $\mathcal{E}_{max} \propto I^\alpha$ (with α ranging from 1/3 to 1) have been proposed. It is worth noting that the intensity as a parameter is not sufficient to predict the proton cutoff energy. Other parameters, such as pulse energy and duration, also need to be taken into account [28].
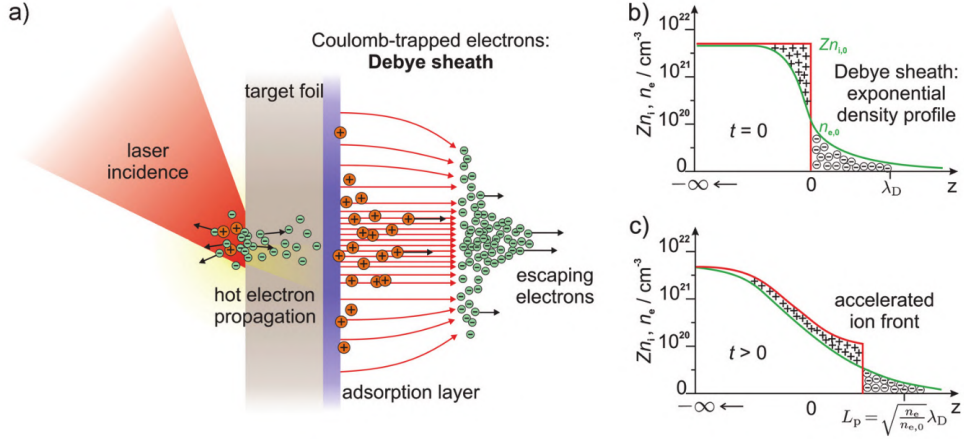

Figure 1.8: a) Schematics of the TNSA process and electron and ion density distribution at the beginning (b) and at a later time (c) of the acceleration. Protons are considered as the only ion species present, which come from a layer of water and other contaminants on the target surface [13].

The isothermal expansion model has two main drawbacks [21]. Firstly, it assumes a constant electron temperature, which is a reasonable assumption for the duration of the laser pulse, but is certainly violated for later times, as the plasma expands and cools. Secondly, the acceleration time is difficult to estimate. The best guess is the pulse length, eventhough the acceleration can continue even after the laser interaction has finished. The situation gets significantly more complicated when we want to analyze plasma composed of multiple ion species and/or two-temperature electron populations. Additionally, we should also consider the recombination processes that occur during expansion.

Interestingly, ions detected behind the target can also be accelerated from the target front side by the sweeping potential at the laser pulse front [29]. The PF sweeps some electrons and piles them at the pulse front. The electric field generated by this charge separation drags the ions behind the electrons. However, this effect is more closely related to front side acceleration due to radiation pressure (rather than rear sheath acceleration) and will be described in more detail in the next subsection.

Target thickness is a crucial parameter in TNSA. It has been demonstrated, both in simulations and experiments [30], that the proton cutoff energy increases in inverse proportion to the target thickness. Sentoku et al. [29] explained this behavior using the concept of hot electron re-circulation, which can enhance the peak proton energy. The hot electrons travel through the target and are then reflected at the target surface by a self-induced sheath field. This electron re-circulation process increases the effective electron density at the target edge, depending on the target thickness. It was verified in simulations that the re-circulation increases the number of hot electrons in the sheath (thus increasing the accelerating field), but it does not increase the electron temperature. However, there is a limit to how thin a target can be before other effects (related to prepulses) destroy the target prematurely and inhibit ion acceleration. For example, the dip in maximum proton energy for low thickness in figure 1.9 can be explained by the shock-wave break-out (see section 1.6).
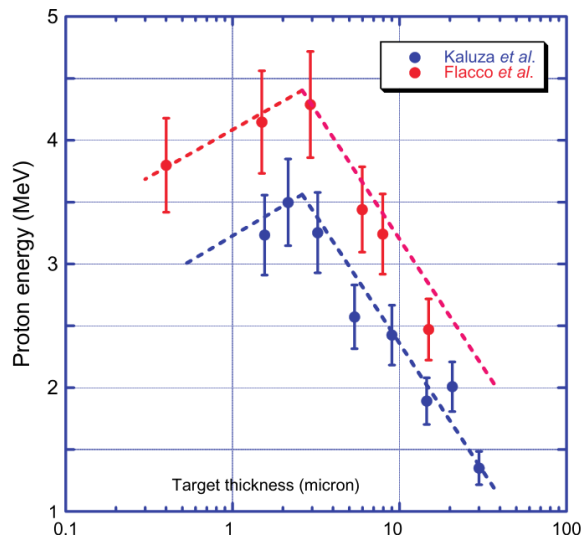
Figure 1.9: Correlation between the proton cut-off energy and the target thickness at $I \approx 10^{19}$ W/cm^2 with a pedestal duration of ≈ 0.5 ns (blue) and at $I \approx 5 \times 10^{19}$ W/cm^2 with pedestal duration ≈ 25 ps (red). There is a clear trend towards increasing proton energy when the target thickness is reduced. However, below a certain thickness, the trend is reversed due to prepulse effects (SBO) creating a plasma on the rear side. [30].

1.4.2 Other mechanisms

Electromagnetic waves carry momentum, which may be delivered to an opaque medium. This is the origin of radiation pressure. On a deeper level, radiation pressure is directly related to the ponderomotive force. At the surface of an overdense plasma the electrons are pushed inwards by the leading edge of the pulse, leaving a charge separation layer and creating an electrostatic field that acts on the ions and leads to acceleration [2]. Radiation Pressure-Dominant Acceleration (RPDA or RPA) is divided into two modes: Hole Boring (HB) for thick targets and Light Sail (LS) for thin targets. Notice that in the literature different terms, such as "sweeping acceleration" [29] or "laser piston" [31], are also used to refer to essentially the same family of processes, resulting from the effect of radiation pressure and the ponderomotive force.

RPA models have received significant attention in recent years due to favorable energy scaling with intensity, higher energy conversion efficiency (compared to TNSA) and the potential to produce high-quality, quasi-monoenergetic ion beams. Early analysis by Esirkepov et al. in 2004 [31] suggested that RPA becomes dominant (over mechanisms relying on hot electrons) at ultra-high intensities ($I \simeq 10^{23}$ W/cm^2). However, the scientific community soon realized [32] that pulses with circular polarization at normal laser incidence (which suppress hot electron generation) would enable investigation of RPA at lower intensities, available using present-day laser technology.

For mass-limited targets (usually micron size plasma clusters), a laser pulse may be intense enough to rapidly blow out almost all of the electrons under the action of the PF. The remaining ion core expands (explodes) due to the Coulomb repulsion of positive electric charges and the ions receive kinetic energy according to their initial position in the cluster. This is the so-called Coulomb Explosion regime.

Not all the observations of ion acceleration may be fully explained in terms of the mechanisms mentioned above. Depending on the laser and target parameters, the mechanism may be of hybrid nature, combining aspects of more than one "basic" acceleration mechanisms. Some other explored mechanisms include collisionless shock acceleration and mechanisms which exploit relativistic transparency in near-critical density and underdense plasmas (break-out afterburner, magnetic vortex acceleration).

1.5 Generation of ultrashort petawatt pulses

In order to achieve ultrahigh focused peak intensity on target, it is necessary to generate a laser pulse with short duration, high energy and good beam-quality. Therefore, we need a short-pulse oscillator that produces low energy, high-quality seed pulses which are then passed through a chain of optical power amplifiers. The limit to the maximum peak power that can be reached is set by the damage threshold of the amplifiers and other optical elements used. In 1985 the team of Mourou proposed the Chirped Pulse Amplification (CPA) technique for optical laser radiation [33] and in 1988 the first CPA laser was successfully demonstrated by Strickland [34]. A simplified diagram of a CPA laser system is presented in figure 1.10. This invention revolutionized the field of high-power laser systems and in 2018 Mourou and Strickland were awarded the Nobel prize in Physics.
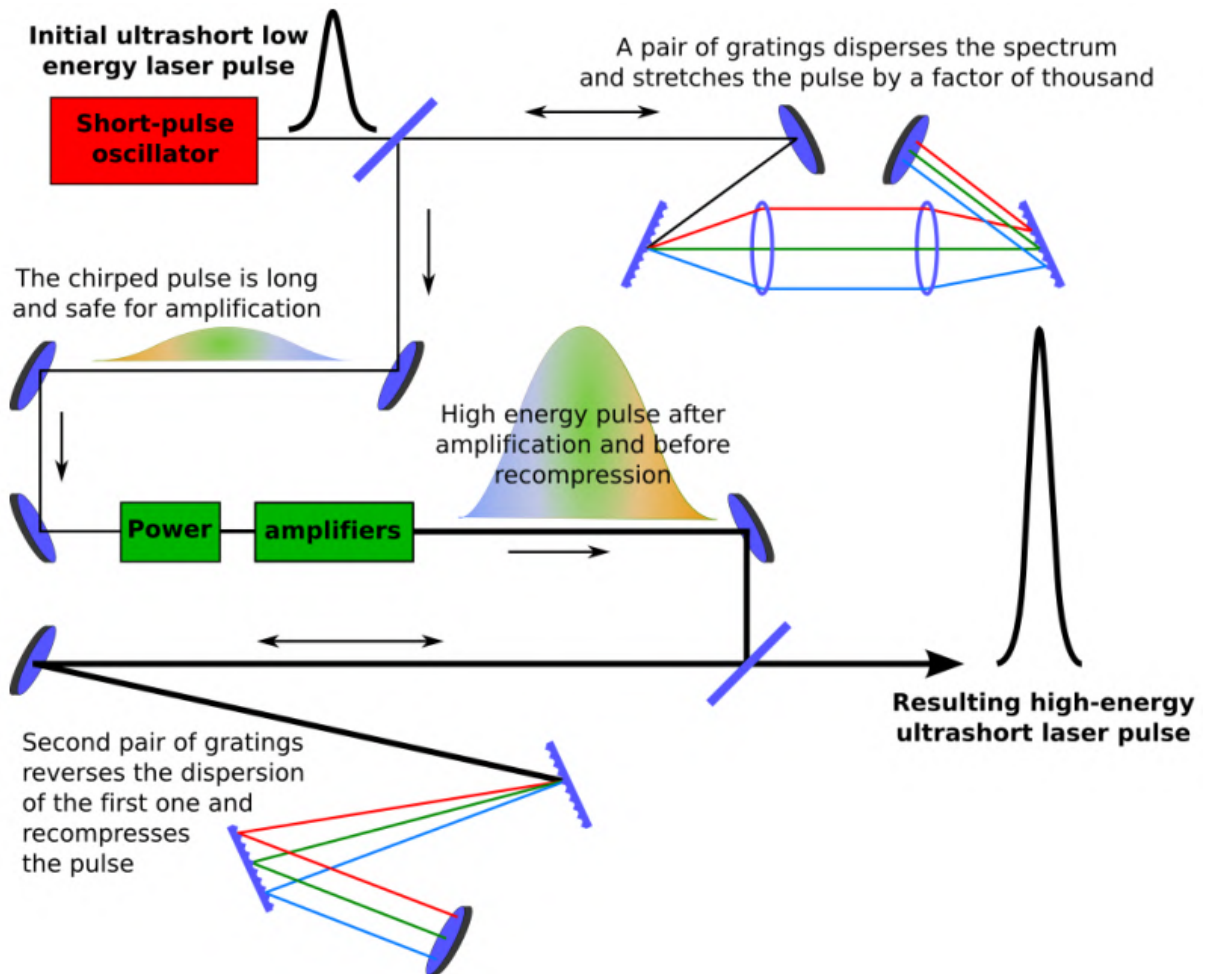
Figure 1.10: Schematic diagram of the CPA technique [26].

In CPA, the seed pulse produced by the laser resonator is first sent to the stretcher. The stretcher usually consists of a pair of gratings and has positive Group Delay Dispersion (GDD). This means that, inside this device, shorter wavelengths will be delayed more than longer wavelengths. Due to the large bandwidth of ultrashort pulses, the stretcher results in significant chirping and broadening of the pulse in time. The longer, low-intensity pulse can now be amplified to much higher energy without running the risk of optically-induced damage. Finally, the amplified pulse is passed through the compressor which removes the chirp and shortens the pulse. A common choice for seed oscillator is the diode-pumped Ti:Sapphire laser with passive Kerr lens mode-locking, which can produce a train of ultrashort pulses with duration in the tens of femtoseconds (cf. HAPLS laser system).

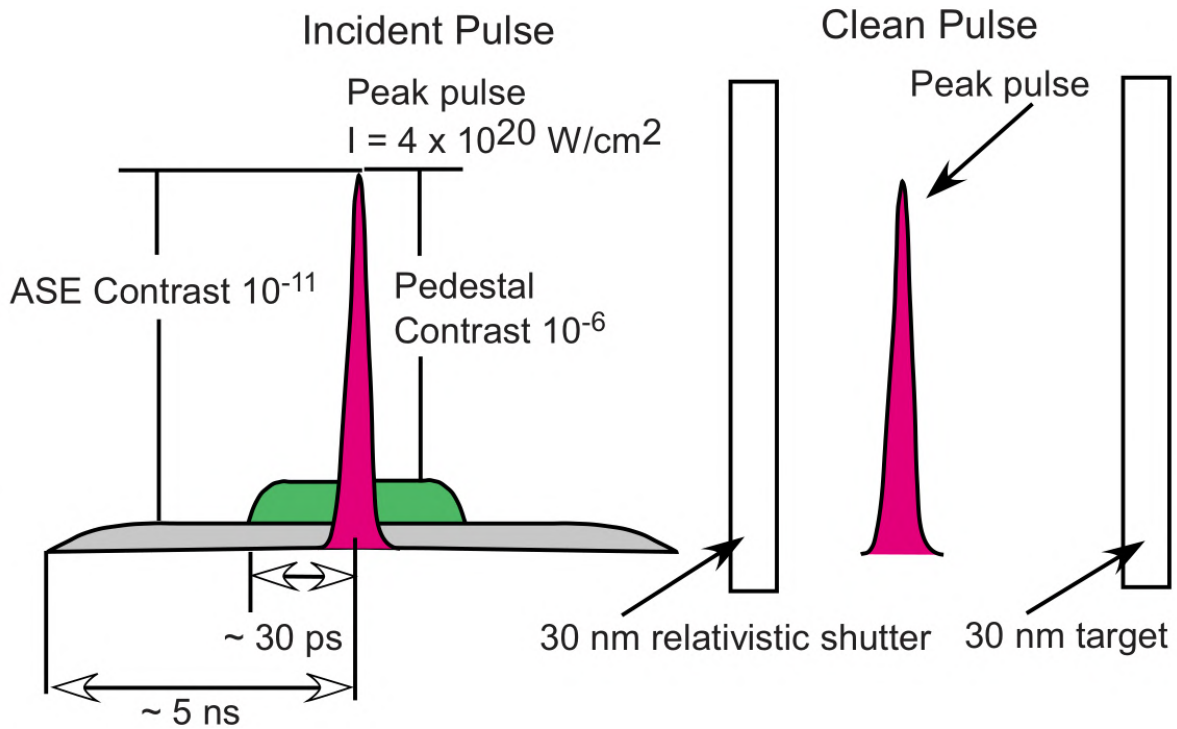Figure 1.11: Schematic of the temporal structure of ultra-intense laser pulses. Such pulses can be cleaned using, for example, a relativistic plasma shutter [35].

The amplification of short laser pulses via the CPA scheme introduces various parasitic effects which degrade the temporal profile of pulses. Unlike the idealized illustration of a perfect Gaussian shape in figure 1.10, a real pulse has a complicated structure. The main pulse is typically preceded by a picosecond pedestal (or picosecond ramp - slope which rises slowly compared to an ideal Gaussian pulse), a background of Amplified Spontaneous Emission (ASE) lasting for several nanoseconds and possibly some femtosecond prepulses (similar duration to main pulse but weaker). The pedestal is understood to originate from imperfect re-compression of the amplified pulse, while ASE originates from the amplifier chain and it is a general feature common to all amplification systems that rely on population inversion. There can be many sources of the aforementioned femtosecond prepulses, but often such prepulses are considered to be avoidable since they are mainly associated with spurious reflections at surfaces of transmissive optics in the system [36]. Figure 1.11 shows the typical profile of such pulses (femtosecond prepulses not shown). An important figure-of-merit is the temporal contrast, defined by the ratio of the peak intensity to the intensity at a given time before this maximum.

There exist several experimental techniques to enhance this intensity contrast. These cleaning methods include the use of: double CPA, Optical Parametric Amplification (OPA/OPCPA), Pockels cells, saturable absorbers and cross-polarized wave (XPW) [37]. We choose to explain in more detail two other cleaning methods, namely relativistic plasma shutters and plasma mirrors. A relativistic plasma shutter (cf. figure 1.11) is an ultra-thin foil placed before the target. This foil is ionized by the leading edge of the focused laser and expands into a relativistically underdense plasma for the peak intensity pulse but is overdense for the low intensity pedestal. Thus, the main pulse is transmitted while the pedestal is reflected [35]. A plasma mirror is an anti-reflection coated substrate. Light is focused on the substrate and is transmitted until the rising intensity ionizes the substrate's surface, creating plasma with overcritical density which reflects the high-intensity part of the pulse. A Double Plasma Mirror (DPM) setup is used in the ELIMAIA hall [1].

1.6 The effect of prepulses on ion acceleration

When a prepulse impacts the surface of a solid target it can have two direct effects, depending on its intensity and duration: it can firstly ablate and/or ionize the target front side and it can also launch a collisional shock (pressure) wave inside the target. Both phenomena can affect ion acceleration and will be discussed separately.

In order to remove an atom from a solid, one should deliver more energy than the binding energy of that atom. Thus, to ablate the same amount of material with a shorter pulse one should apply higher laser intensity approximately in inverse proportion to the pulse duration. For example, laser ablation with 100 fs pulses requires an intensity in the range $\sim 10^{13} - 10^{14}$ W/cm^2, while a 30-100 ns pulse ablates the same material at the intensities $\sim 10^8 - 10^9$ W/cm^2. At intensities above $\sim 10^{13} - 10^{14}$ W/cm^2 ionization of practically any target material takes place [38]. Therefore, we conclude that if we use ultrahigh peak intensities ($> 10^{20}$ W/cm^2) with 10^6 ASE contrast, it is expected that the front portion of the target will be ionized and a preplasma cloud will form. The preplasma expansion is usually modeled by hydrodynamic simulations. Alternatively, we can use the model of isothermal plasma expansion into vacuum (see section 1.4.1). This model is, however, only a rough estimate because plasma heating continues throughout the duration of the ASE pedestal. Typically, the preplasma assumes an exponential density profile with scale-length L_p (the distance at which the plasma density drops $e = 2.718$ times), with the critical surface located at the distance s_c from the plateau (remaining portion of the target). The scale-length of preplasma can extend from a few up to tens of μm, depending on prepulse intensity, duration and target material parameters.
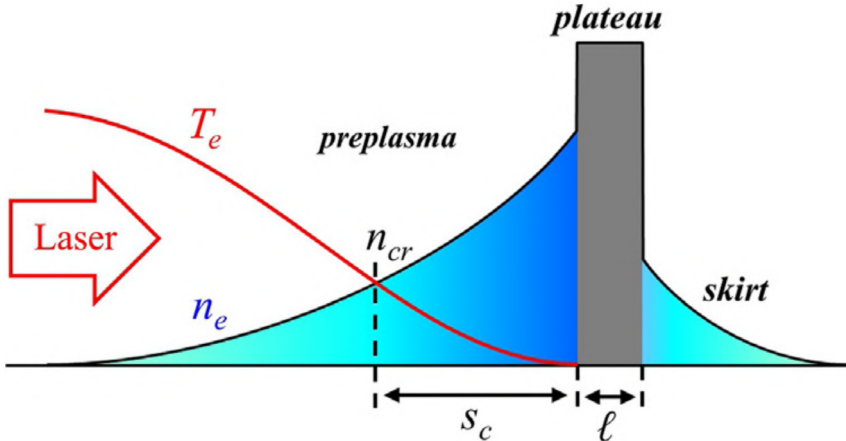

Figure 1.12: Schematic distributions of the electron density and temperature in a typical target structure created by a nanosecond prepulse. The plateau is surrounded by a preplasma at the front side and by a skirt at the back side [39].

The effect of preplasma on ion acceleration has been examined in several publications [29, 39, 40]. It is clear that, for low-contrast pulses, an ultra-thin target can be completely transformed into an underdense plasma which prevents TNSA or RPA. However, both experiments and simulations have demonstrated that, with the right combination of target thickness and prepulse intensity, ion acceleration can be significantly enhanced. This can be explained by different processes in the preplasma (e.g. resonant absorption, self-focusing, stochastic heating) which can increase the efficiency of laser energy absorption and thus result in more energetic ions. Figure 1.13 demonstrates that there can exist an optimal preplasma scale-length which affords the highest energy. Moreover, varying the preplasma scale-length, L_p, and plateau thickness, ℓ, can give access to different regimes of ion acceleration (both TNSA and RPDA). Therefore, if the preplasma thickness is optimal, the main pulse can reach the target accelerating fast ions more efficiently than an ideal, infinite contrast, laser pulse [39].
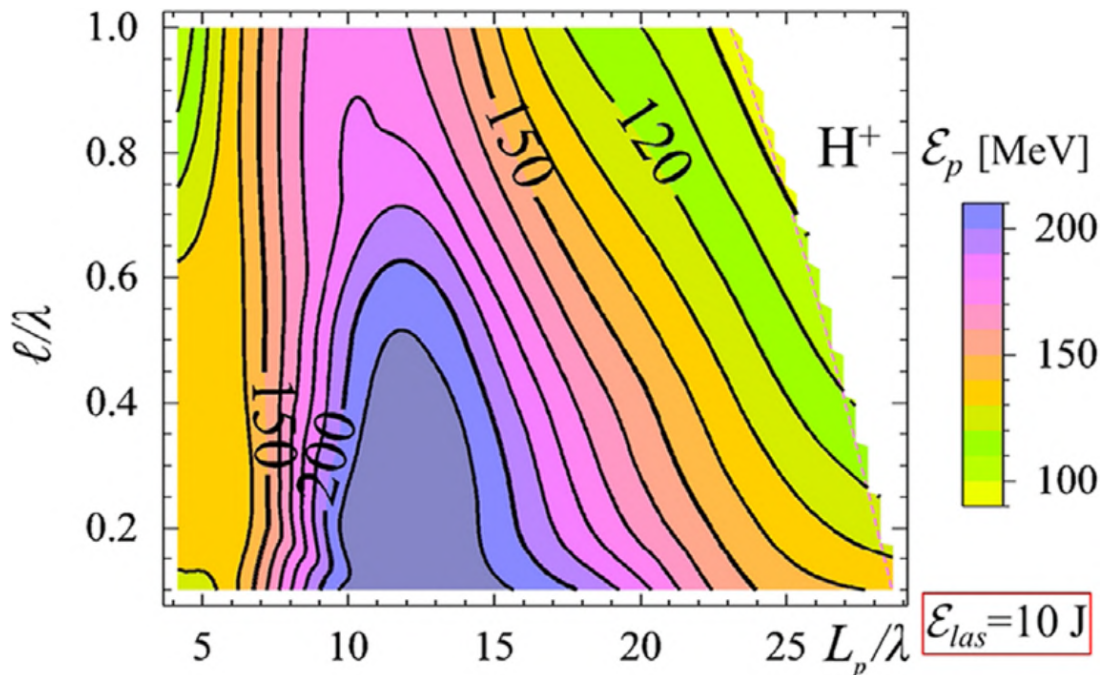
Figure 1.13: Maximum proton energy in MeV as a function of L_p and ℓ for a 30 fs, 10 J main pulse (2D multi-parametric PIC simulations) [39].

Finally, we will discuss the effect of the shock wave on the TNSA mechanism [30]. The shock wave has velocity D that depends on prepulse intensity, wavelength and target material. Shock Break-Out (SBO) occurs when this wave reaches the rear side of the target. The shock results in vaporization of the target rear side and plasma formation, known as the skirt (cf. figure 1.12). For TNSA it has been shown that an undisturbed rear target surface is strongly favorable since an extended skirt would attenuate the accelerating field, decreasing the maximum achievable ion energy [30, 41] (cf. figure 1.9). Therefore, for efficient TNSA the main pulse should arrive before SBO (i.e. $\ell_0 > D\tau$, where τ is the time-delay between the prepulse and main pulse and ℓ_0 is the original target thickness). The shock pressure from the prepulse can also deform and displace the target relative to the original geometry.

Unfortunately, the PIC method is not well suited for the interaction regime involving prepulses. Firstly, the low intensity implies that we need to take collisions into account and secondly the long (nanosecond) time-scales of interaction followed by expansion would make the PIC approach very computationally expensive. Instead, the effect of prepulses is typically analyzed using hydrodynamic simulations. This is a fluid description where the microscopic behaviour of the constituent particles is ignored and one only has to consider the macroscopic properties of particles, which include: the mass density, the fluid velocity and the pressure of the fluid. Generally, the fluid description of plasmas can include the possibility of magnetic fields as well (as in MHD, Magneto-Hydrodynamics). A detailed description of hydrodynamic codes is beyond the scope of this thesis and the interested reader can refer to chapter 14 in [42].

In summary, the use of ultra-thin targets imposes high demands on the temporal quality of laser pulses. Laser contrast has a major effect on laser-driven ion acceleration. At a given intensity level preceding the peak intensity, pre-ionization occurs leading to an expanded preplasma at the target surface. While for sufficiently thick targets this could even be beneficial since self-focusing and enhanced absorption in the preplasma might increase the hot electron temperature, this can be an issue for very thin targets, either due to complete target disintegration or SBO which interferes with TNSA [37].

Chapter 2

The Particle-In-Cell (PIC) Method for Laser-Plasma Simulations

2) Particle pusher

$$\frac{\mathrm{d}\mathbf{p}_p}{\mathrm{d}t} = r_s \left(\mathbf{E}_p^{(n)} + \langle \mathbf{v}_p \rangle^{(n)} \times \mathbf{B}_p^{(n)} \right)$$

$$\frac{\mathrm{d}\mathbf{x}_p}{\mathrm{d}t} = \mathbf{v}_p^{(n+1/2)} = \left(\frac{\mathbf{p}_p}{m_s \gamma_p} \right)^{(n+1/2)}$$

Update momentum and position $\forall p$
after Δt using a leap-frog solver:
$$\mathbf{p}_p^{(n-1/2)} \to \mathbf{p}_p^{(n+1/2)} \text{ and } \mathbf{x}_p^{(n)} \to \mathbf{x}_p^{(n+1)}$$

Diagnostic out

1) Field interpolation

$$F_p^{(n)} = \sum_i \langle F_i \rangle^{(n)} W\big(\mathbf{x}_i - \mathbf{x}_p^{(n)}\big)$$

Each field component F is
known on its own set of shifted
grid points $\mathbf{x}_i$ (Yee grid).
The fields are interpolated
on the particle position $\mathbf{x}_p$.

N cycles

Initialization

3) Charge deposition

$$\rho_i^{(n+1)} = \frac{1}{V_i} \sum_p q_p W\big(\mathbf{x}_i - \mathbf{x}_p^{(n+1)}\big)$$

Current densities on grid are
computed from the charge
flux through cell borders:
$$\left[\mathbf{x}_p^{(n)}, \mathbf{x}_p^{(n+1)}, \mathbf{p}_p^{(n+1/2)} \right] \to \mathbf{J}_i^{(n+1/2)}$$

4) Maxwell solver

$$\frac{\mathrm{d}\mathbf{E}}{\mathrm{d}t} = c^2 \left[(\nabla \times \mathbf{B})^{(n+1/2)} - \mu_0 \mathbf{J}^{(n+1/2)} \right]$$

$$\frac{\mathrm{d}\mathbf{B}}{\mathrm{d}t} = -(\nabla \times \mathbf{E})^{(n+1)}$$

The fields on the Yee grid are advanced
after Δt using the FDTD approach:
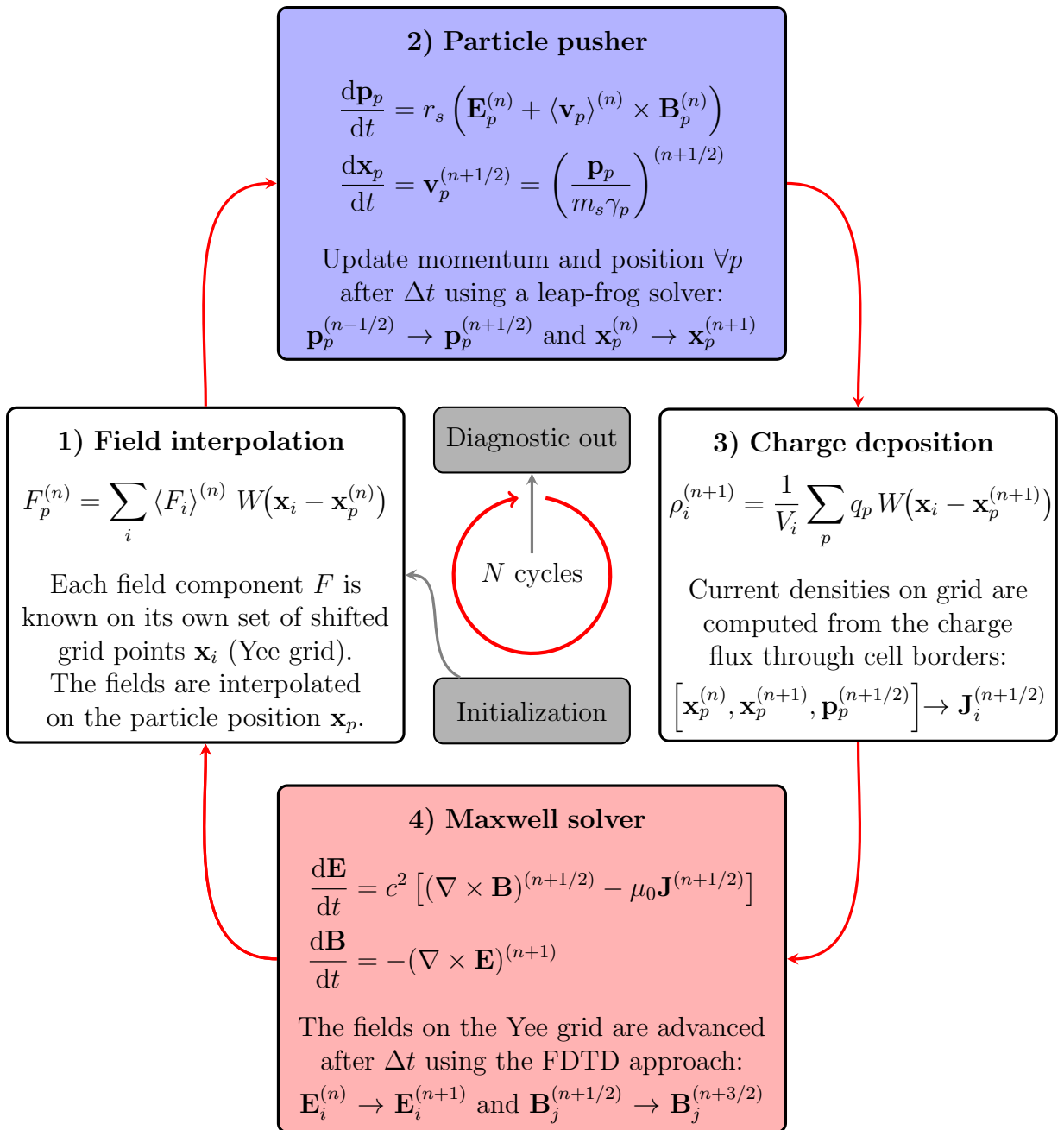$$\mathbf{E}_i^{(n)} \to \mathbf{E}_i^{(n+1)} \text{ and } \mathbf{B}_j^{(n+1/2)} \to \mathbf{B}_j^{(n+3/2)}$$

Figure 2.1: Flowchart showing the main steps of the PIC loop used in the Smilei code.

The physical system of ionized matter (plasma) interacting with ultra-short, intense laser pulses is intrinsically complex: large numbers of charged particles interacting with each other on femtosecond time-scales through strong electromagnetic fields. Therefore, any attempt to simulate such a system comes at great computational cost and can only be realized by utilizing High-Performance Computing (HPC).

Not all simulation approaches are suitable. For example, hydrodynamic theory is not applicable to the highly non-equilibrium plasma conditions [42] caused by ultra-short fs, intense laser pulses. Hydrodynamic simulations can be useful in the case of longer ps and ns prepulses, where there is thermal plasma expansion and collisions are significant. Plasma kinetic theory takes into account the motion of all particles. The Klimontovich equation describes the time evolution of point-particle trajectories and therefore provides (together with Maxwell's equations 2.3-2.6) an exact description of the plasma [43]:

$$\left[\partial_t + \mathbf{v} \cdot \nabla_{\mathbf{x}} + \frac{q_s}{m_s}\left(\mathbf{E} + \mathbf{v} \times \mathbf{B}\right) \cdot \nabla_{\mathbf{v}}\right] N_s(\mathbf{x}, \mathbf{v}, t) = 0 \quad , \tag{2.1}$$

where $N_s = \sum_i \delta(\mathbf{x} - \mathbf{X}_i(t))\delta(\mathbf{v} - \mathbf{V}_i(t))$ is known as the density functional and the sum runs over all point-particles belonging to species s. This is, however, very complex and far from being solvable in practice due to the high computational resource requirements.

We instead need a simplified system description that minimizes computational cost while preserving fidelity to the physical situation. The real usefulness of the Klimontovich equation (2.1) is as a starting point for the derivation of the simpler Vlasov equation (2.2) that describes the average properties of a plasma [44]. The Particle-In-Cell (PIC) method (which is based on the Vlasov equation 2.2) represents a powerful tool for kinetic plasma studies and is suitable for modeling intense laser-plasma interactions. PIC codes for simulating collisionless plasma kinetics are among the most widely used computational tools in plasma physics. With algorithmic development since the 1970s they are also one of the most studied plasma simulation techniques [45].

This chapter is thus devoted to the explanation of general aspects of the PIC method and the Smilei code which was used in this thesis. The following discussion is based on the original Smilei article [46]. The interested reader is referred to this article for a more detailed description of the Smilei PIC code implementation.

2.1 Vlasov-Maxwell equations and super-particles

The Vlasov equation describes the evolution of the single-species distribution function in position-momentum space. In the general 3D case, it has to be solved in 6-dimensional phase-space (three spatial and three momentum coordinates). The distribution function is a statistical description of a very large number of interacting particles. In this approach, $f_s(t, \mathbf{x}, \mathbf{p})\, d\mathbf{x}\, d\mathbf{p}$ is equal to the number of particles of species s in the phase-space domain $[(\mathbf{x}, \mathbf{x} + d\mathbf{x}), (\mathbf{p}, \mathbf{p} + d\mathbf{p})]$. The collisionless[1] Vlasov equation has the form

$$\left(\partial_t + \frac{\mathbf{p}}{m_s\gamma} \cdot \nabla_{\mathbf{x}} + \mathbf{F}_L \cdot \nabla_{\mathbf{p}}\right) f_s = 0 \quad , \tag{2.2}$$

where $\mathbf{p} = \gamma m_s \mathbf{v}$, $\gamma = [1 - \mathbf{v}^2/c^2]^{-1/2} = [1 + \mathbf{p}^2/(m_s c)^2]^{1/2}$ is the relativistic factor and $\mathbf{F_L} = q_s(\mathbf{E} + \mathbf{v} \times \mathbf{B})$ is the Lorentz force.

---

[1]If collisions are important (at lower intensities) the right-hand side of the Vlasov equation needs to be modified. The Smilei code implements special modules for processes such as collisions and ionization.

The Vlasov equation (2.2) together with the Maxwell equations (2.3-2.6) describe the self-consistent dynamics of the plasma, whose constituent particles are subject to the Lorentz force and in turn modify the electric and magnetic fields through their charge and current densities.

$$\nabla \cdot \mathbf{E} \;=\; \rho/\epsilon_0 \,, \tag{2.3}$$

$$\nabla \cdot \mathbf{B} \;=\; 0 \,, \tag{2.4}$$

$$\nabla \times \mathbf{E} \;=\; -\partial_t \mathbf{B} \,, \tag{2.5}$$

$$\nabla \times \mathbf{B} \;=\; \mu_0 \mathbf{J} + \mu_0 \epsilon_0 \partial_t \mathbf{E} \,. \tag{2.6}$$

The Vlasov equation is still quite complicated to solve numerically and codes that do so are resource intensive. Fortunately, there exists a more computationally efficient, finite-element method to solve equation (2.2). In this method the continuous distribution function can be approximated (sampled) in phase-space by a set of finite phase-fluid elements (FPFE) [21], each element having a finite spatial extent and representing a large number of real particles (see figure 2.3). In fact, the PIC method owes its name to this discretization of the distribution function f_s as a sum of N_s 'super-particles' (also referred to as 'macro-particles' or 'computational particles'):

$$f_s(t, \mathbf{x}, \mathbf{p}) = \sum_{p=1}^{N_s} w_p \, S(\mathbf{x} - \mathbf{x}_p(t)) \, \delta(\mathbf{p} - \mathbf{p}_p(t)) \quad , \tag{2.7}$$

where p is the particle[2] index, w_p its numerical 'weight', $\mathbf{x}_p$ its position and $\mathbf{p}_p$ its momentum. All particles have the same shape-function, $S(\mathbf{x})$, which usually belongs to the family of b-spline functions (figure 2.2). A δ-function is chosen for momentum, which ensures that the shape of particles and the volume in phase-space are conserved.

B-spline functions are defined recursively using the convolution $b_m = b_{m-1} * b_1$, where $b_1[(x - x_p)/\Delta x_p] = rect[(x - x_p)/\Delta x_p]$. Some properties of these functions are:

- Symmetric with respect to the argument x.

- Normalized so that $\int \mathrm{d}x \, b_m[(x - x_p)/\Delta x_p] = 1$.

- Finite extent: non-zero only within a region extending over $m\Delta x_p$ around $x = x_p$, where m is the order of the shape function (interpolation order).

The discretization of the physical situation in space (Cartesian grid) and time gives rise to a lack of energy conservation, known as numerical heating. This means that the kinetic energy increases linearly with time because the macroparticles are affected by a random, nonphysical grid force at each timestep. The interpolation order m is an important parameter since it determines the shape and spatial extent of the shape-function. This numerical noise can be greatly reduced by using higher order shape functions, at the cost of computational time (higher order $\Rightarrow$ greater spatial spread $\Rightarrow$ overlap with more cells $\Rightarrow$ field interpolation and current deposition is more demanding) [47, 48].

Using the decomposition of the distribution function given in equation (2.7), it can be shown that the Vlasov equation can be transformed into the following set of equations of motion for the super-particles:

$$\frac{\mathrm{d}\mathbf{u}_p}{\mathrm{d}t} \;=\; r_s \left(\mathbf{E}_p + \frac{\mathbf{u}_p}{\gamma_p} \times \mathbf{B}_p \right) \quad ; \quad \frac{\mathrm{d}\mathbf{x}_p}{\mathrm{d}t} \;=\; \frac{\mathbf{u}_p}{\gamma_p} \,, \tag{2.8}$$

where $r_s = q_s/m_s$, $\mathbf{u}_p = \mathbf{p}_p/m_s$ and $\mathbf{E}_p$, $\mathbf{B}_p$ are the fields interpolated at the particle position (more details about the field interpolation in the next section).

---

[2] For the rest of this chapter, the words 'particle' and 'super-particle' are used interchangeably for the sake of convenience and should be understood to mean the same thing.
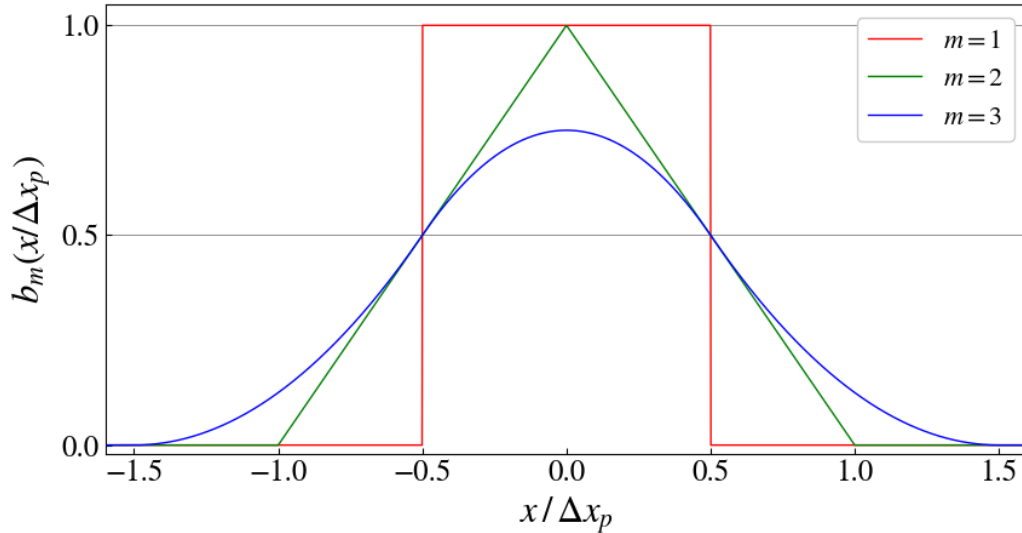
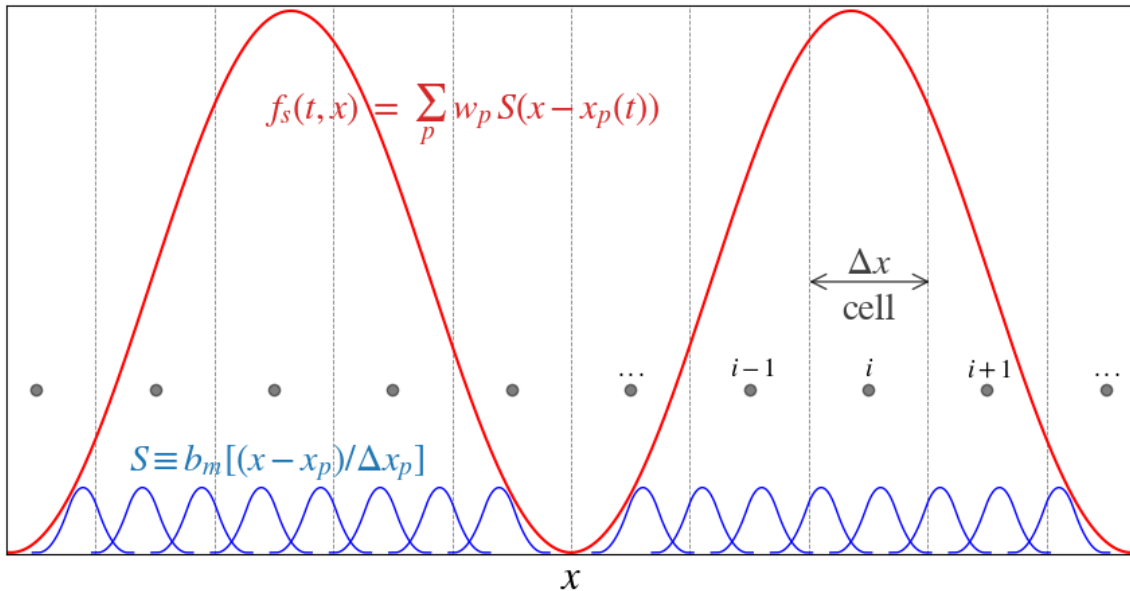Figure 2.2: B-spline functions of different interpolation orders.

Figure 2.3: Illustration of sampling an arbitrary distribution function in 1D space, $f_s(t, x) \equiv \int f_s(t, x, p)\, dp$ (red curve), using super-particle shape functions (blue curves). Note that, with proper choice of numerical weights, the sum of the shape-functions (blue) should reproduce the distribution function (red). Fields are solved on the discrete spatial grid points i, while super-particles can move continuously anywhere in the cells.

2.2 The Particle-In-Cell loop

The PIC algorithm consists of an initialization step followed by cycling over a computational loop for N time-steps. Each time-step consists of (i) interpolating the electromagnetic fields at the particle positions, (ii) computing the new particle velocities and positions, (iii) projecting the new charge and current densities on the grid, and (iv) computing the new electromagnetic fields on the grid. Additionally, we may choose to perform some diagnostic operation at selected times and output the results for later analysis. In this section, we describe these four steps taken to advance one time-step. The PIC loop is visually summarized in figure 2.1.

Before initialization, we need to set the simulation parameters. This choice is mostly based on the problem we want to investigate and the computational resources available. However there exist numerical criteria on some parameters which ensure the simulation will behave correctly. Firstly, Finite-Difference Time-Domain (FDTD) solvers are subject to the Courant-Friedrich-Lewy (CFL) condition[3], which sets limits on the length of time-step we can use:

$$c\,\Delta t < \left(\Delta x^{-2} + \Delta y^{-2} + \Delta z^{-2} \right)^{-1/2} \quad , \tag{2.9}$$

where $\Delta x, \Delta y, \Delta z$ is the cell size in each spatial dimension of the simulation. This condition guarantees that we can resolve the propagation of electromagnetic waves since they cannot travel a distance of more than one cell width during one time-step. Additionally, the time-step should be smaller than the free electron oscillation period in plasma to also resolve propagation of plasma waves ($\Delta t < 1/\omega_{pe}$) and the cell size should be smaller than the skin-depth in order to resolve the physics of absorption at the plasma-vacuum boundary ($\Delta x < c/\omega_{pe}$). Cell size should be comparable to the Debye length to reduce numerical heating ($\Delta x < \varsigma\lambda_D$[4]).

Finally, we need to decide on the boundary conditions we want to impose on particles and fields at the edges of the simulation box. Particles reaching the edge can either loop around the box (periodic), be stopped (momentum set to zero), suppressed (removed from memory), reflected (momentum and position follow specular reflection rules) or thermalized[5]. Boundary conditions for electromagnetic fields include periodic, injecting/absorbing and reflective.

Initialization of the simulation
The initialization of a PIC simulation requires the loading of particles followed by computing the initial electric and magnetic field at the grid points. The particle loading consists of creating N_s particles in each cell with either randomly chosen or regularly spaced positions, and with momenta randomly sampled from a distribution (the Maxwell-Jüttner distribution is a common choice for relativistic intensities since it describes the distribution of velocities in a gas of relativistic particles). The initial electric and magnetic fields are calculated through the total charge and current densities computed on the grid. Then, we can enter the main loop of the algorithm by performing field interpolation on the particle positions.

1) Field interpolation onto particles
We need to use knowledge of the fields at time-step n in order to advance the particle positions. However, the fields are calculated at discrete grid points $\mathbf{x}_i$ but we need to estimate the field acting on each super-particle at an arbitrary position $\mathbf{x}_p$. Therefore, we need to interpolate the discrete fields to the whole space and apply the following overlap integral:

$$F_p^{(n)} = \int \mathrm{d}\mathbf{x}\, S(\mathbf{x} - \mathbf{x}_p^{(n)})\, \langle F(\mathbf{x}) \rangle^{(n)} \quad , \tag{2.10}$$

where F represents a field component ($E_x, E_y, E_z, B_x, B_y, B_z$). The angle brackets $\langle...\rangle$ imply time-centered fields since not all quantities are calculated at integer time-steps (the leap-frog method advances the magnetic fields, current densities and velocities at half-integer time-steps). For example, a time-centered magnetic field component looks like $\langle B \rangle^{(n)} \equiv [B^{(n-1/2)} + B^{(n+1/2)}]/2$. Similarly, the time-centered velocity has the form $\langle \mathbf{v}_p \rangle^{(n)} \equiv [\mathbf{v}_p^{(n-1/2)} + \mathbf{v}_p^{(n+1/2)}]/2$. The continuous field $F(\mathbf{x})$ can be constructed from the

---

[3]Necessary condition for convergence when solving certain partial differential equations numerically.

[4]ς is a constant ranging from $\sim 1 - 10$, depending on the order of the interpolation function.

[5]Particle set back in the simulation box with momentum sampled from a Maxwellian distribution.

grid by assuming that the field throughout the cell is constant. If we also assume more neighboring cells with Cartesian symmetry, we have:

$$\langle F(\mathbf{x})\rangle^{(n)} = \sum_i \langle F_i\rangle^{(n)} \tilde{b}_1 \left[\frac{\mathbf{x} - \mathbf{x}_i}{\Delta x}\right] \equiv \sum_i \langle F_i\rangle^{(n)} \prod_j b_1 \left[\frac{(\mathbf{x} - \mathbf{x}_i)_j}{\Delta x}\right] \quad , \qquad (2.11)$$

where the sum runs over all grid points of component F and the product runs over the three Cartesian coordinates ($j = x, y, z$). i denotes the grid point index, $\mathbf{x}_i$ the ith grid point and Δx the cell size. Note that different fields are known on shifted grid points due to the use of a staggered grid, Yee's grid, so depending on the field, the set of points we sum over is different (cf. figure 2.5). In the above equation we have also defined the 3-dimensional b-spline for Cartesian symmetry ($\tilde{b}_m$) as the product of three, 1-dimensional b-splines. Upon plugging equation 2.11 into equation 2.10, one finds:

$$F_p^{(n)} = \sum_i \langle F_i\rangle^{(n)} \int d\mathbf{x}\, S(\mathbf{x} - \mathbf{x}_p^{(n)})\, \tilde{b}_1 \left[\frac{\mathbf{x} - \mathbf{x}_i}{\Delta x}\right] = \sum_i \langle F_i\rangle^{(n)} W\left(\mathbf{x}_i - \mathbf{x}_p^{(n)}\right) \quad , \quad (2.12)$$

where we have defined the interpolation function, $W(\mathbf{x}_i - \mathbf{x}_p^{(n)})$. Note that W is non-zero only over cells particle p is in contact with. Due to the limited spatial extent of S, we only have to consider few terms in the grid point summation of equation 2.12. If $S(\mathbf{x} - \mathbf{x}_p^{(n)})$ is an mth-order spline function that also possesses Cartesian symmetry[6] and has the same width as the cells, then by the definition of b-splines using convolution, we can write

$$W\left(\mathbf{x}_i - \mathbf{x}_p^{(n)}\right) = \tilde{b}_{m+1}\left(\frac{\mathbf{x}_i - \mathbf{x}_p^{(n)}}{\Delta x}\right) \quad . \qquad (2.13)$$

Therefore, we see that the interpolation function W is one order higher compared to the interpolation order of the shape function.

2) Particle push
Having knowledge of the fields acting on the particles, we can apply a finite-difference method to the equations of motion in order to advance velocity and position to the next time-step. Leap-frog integration is the method of choice because it is second-order accurate, it possesses global stability and approximately conserves energy[7].

In the leap-frog method position and velocity are calculated at shifted times. More specifically, position is known at integer time-steps and velocity at half-integer time-steps (cf. figure 2.4). Using finite differences, we evaluate the new velocity from equation (2.8)-left and then plug it into equation (2.8)-right to compute the next position:

$$\mathbf{u}_p^{(n+\frac{1}{2})} = \mathbf{u}_p^{(n-\frac{1}{2})} + r_s \Delta t \left[\mathbf{E}_p^{(n)} + \frac{\mathbf{v}_p^{(n+\frac{1}{2})} + \mathbf{v}_p^{(n-\frac{1}{2})}}{2} \times \mathbf{B}_p^{(n)}\right] , \qquad (2.14)$$

$$\mathbf{x}_p^{(n+1)} = \mathbf{x}_p^{(n)} + \Delta t \left[\frac{\mathbf{u}_p^{(n+\frac{1}{2})}}{\gamma_p}\right] , \qquad (2.15)$$

where n denotes the (integer) time-step index, Δt is the duration of a time-step and all other terms have been defined previously.

---

[6] If the super-particle is radially symmetric, then W cannot be simplified in this way.
[7] Some other methods, such as the RK family of integrators, are not suitable because the energy will deviate substantially from its initial value at sufficiently long times.
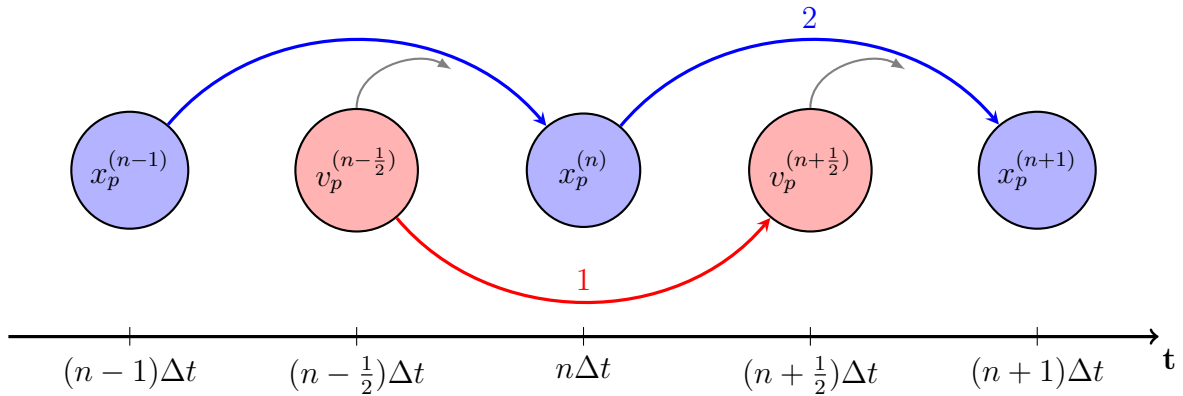
Figure 2.4: Visual representation of the leap-frog algorithm. During the particle push step of the PIC loop: (1) first the velocity is advanced to the next half-integer time-step and, (2) this velocity is then used to advance the position to the next integer time-step. A similar algorithm is also used for advancing electric and magnetic fields.

3) Current deposition onto grid

Smilei employs the method of charge conserving current deposition first proposed in [49]. This scheme allows one to implement the PIC code without solving Poisson's equation (2.3), since the current density computed at the grid points is sufficient to advance the field using the Faraday (2.5) and the Ampère (2.6) equations. The current densities in the dimensions of the grid are computed from the charge flux through the cell borders at half-integer time-steps: $[\forall p \; \mathbf{x}_p^{(n)}, \mathbf{x}_p^{(n+1)}, \mathbf{p}_p^{(n+1/2)}] \to \mathbf{J}_i^{(n+1/2)}$. Charge densities are only projected on the grid for diagnostics purposes (charge density is not used to advance the electromagnetic fields):

$$\rho_i^{(n+1)} = \frac{1}{V_i} \sum_p q_p \, W\big(\mathbf{x}_i - \mathbf{x}_p^{(n+1)}\big) \quad , \tag{2.16}$$

where V_i is the cell volume. Note that the interpolation function, W, is the same as the one defined previously for the fields.

4) Maxwell solvers

Now that the currents are known at time-step $(n + 1/2)$, the finite difference equations arising from the Faraday (2.5) and the Ampère (2.6) equations can be written like:

$$\mathbf{E}^{(n+1)} \;=\; \mathbf{E}^{(n)} \;+\; c^2 \Delta t \left[(\nabla \times \mathbf{B})^{(n+\frac{1}{2})} - \mu_0 \mathbf{J}^{(n+\frac{1}{2})} \right] , \tag{2.17}$$

$$\mathbf{B}^{(n+\frac{3}{2})} \;=\; \mathbf{B}^{(n+\frac{1}{2})} \;-\; \Delta t \, (\nabla \times \mathbf{E})^{(n+1)} . \tag{2.18}$$

First, the Ampère equation is solved, giving the advanced electric fields, and then the Faraday equation is computed, leading to the advanced magnetic fields. Note that a leap-frog scheme is employed for marching in time. This means that the **E**-field and **B**-field updates are staggered so that, during each time-step, **E**-field updates are conducted midway between successive **B**-field updates and vice-versa.

When multiple dimensions are considered, discretization and calculation of the numerical curl can become complicated. In 1966 Kane Yee proposed spatially staggering the vector components of the **E**-field and **B**-field about rectangular unit cells of the Cartesian computational grid, so that the **E**-field components form the edges of the cube and the **B**-field components form the normals to the faces of the cube [50]. This scheme, now known as a Yee grid (see figure 2.5), simplifies the curl calculation and remains at the core of many current FDTD software, including Smilei.
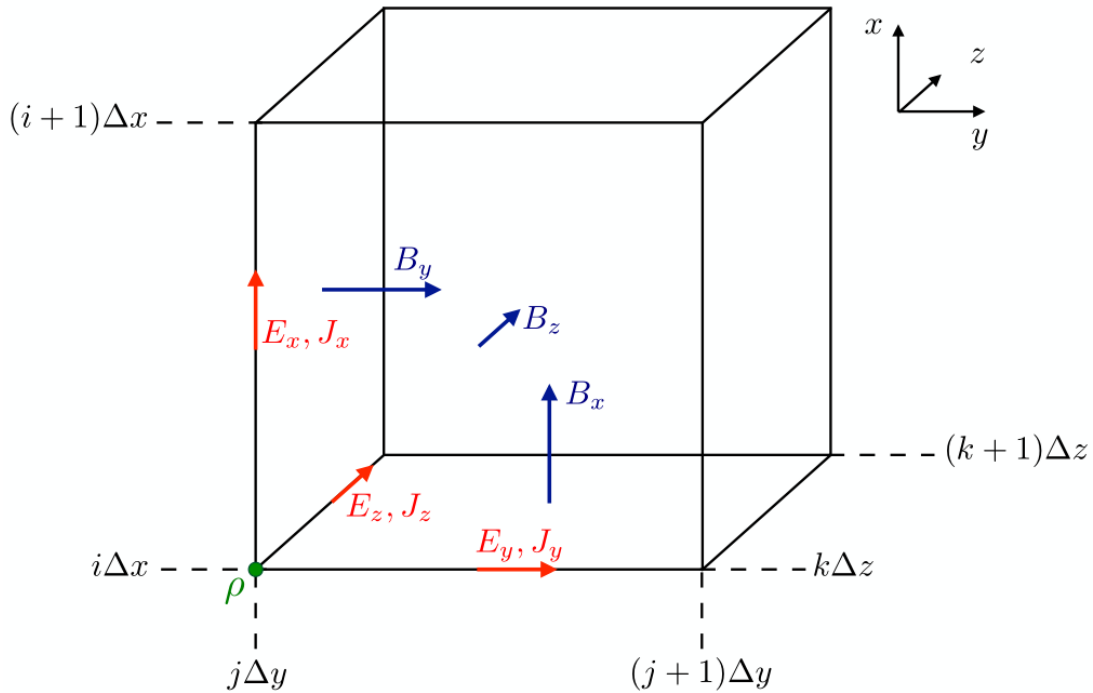
Figure 2.5: Representation of the staggered Yee-grid showing the positions of various field components [46, 50]. The **E**-field components are in the middle of the edges whereas the **B**-field components are in the center of the faces.

2.3   Smilei code and MetaCentrum grid

SMILEI (for Simulating Matter Irradiated by Light at Extreme Intensities) is a fully-relativistic electromagnetic PIC code that uses the Vlasov-Maxwell system to describe the evolution of collisionless plasmas. Additional physics modules can introduce other effects, such as collisions and ionization. To benefit from the latest advances in high-performance computing, Smilei is built with paralellization and workload-balancing capabilities in order to interface efficiently with modern supercomputer architectures.

The input to Smilei consists of an input file written in Python, where all required parameters are defined (for a sample script please see appendix A). It is important to note that the code does not use SI units and instead normalizes all variables to some reference quantities (e.g. velocity normalized to c, charge to e and mass to m_e). Moreover, Smilei offers a wide selection of diagnostic options, ranging from scalar diagnostic (total energy, kinetic energy, etc.) and field diagnostics (electromagnetic fields and charge densities) to more advanced diagnostics for tracking individual particles and introducing screens that filter particles based on some conditions.

MetaCentrum VO operates and manages distributed computing infrastructure consisting of computing and storage resources owned by CESNET as well as those of co-operative academic centers within the Czech Republic. MetaCentrum offers resources for grid computing, which were used to run simulations for the purposes of this thesis. The grid is a network of many interconnected computers, whose properties may differ and which may be located in different institutes in the Czech Republic. The scheduling system keeps track of the grid's resources (memory, CPU time, disk space) and keeps the computational jobs waiting in queues until there is enough resources free for them to run. The users prepare and submit their jobs on machines called front-ends. The rest of the grid's machines, known as computational nodes, do the computation. The interested reader can find more details on the MetaCentrum website at https://metavo.metacentrum.cz/en/.

Chapter 3

The ELIMAIA User Beamline and Ion Diagnostics

ELIMAIA stands for ELI Multidisciplinary Applications of laser-Ion Acceleration and is one of the secondary source beamlines of the ELI-Beamlines (Extreme Light Infrastructure) facility in the Czech Republic. The mission of this laser-driven ion target area is to provide stable, fully characterized and tuneable beams of particles accelerated by Petawatt-class lasers and to offer them to the user community for multidisciplinary applications. The main goal of the laser-driven ion acceleration community is to deliver reliable and very compact approaches to be possibly used for societal applications (e.g. hadron therapy), with the aim of reducing the overall cost of standard accelerator facilities. Currently ELIMAIA is in the commissioning stage in order to optimize the ion accelerator performance and demonstrate the capabilities of this beamline to the user base. In this chapter, the main components of the ELIMAIA beamline will be outlined and various diagnostic tools used for the characterization of the produced ion beams will be described.

3.1   Overview of experimental hall E4

The following description is based on an article by Margarone et. al. [1] titled "ELIMAIA: A Laser-Driven Ion Accelerator for Multidisciplinary Applications", outlining the most recent progress towards implementation of the beamline.
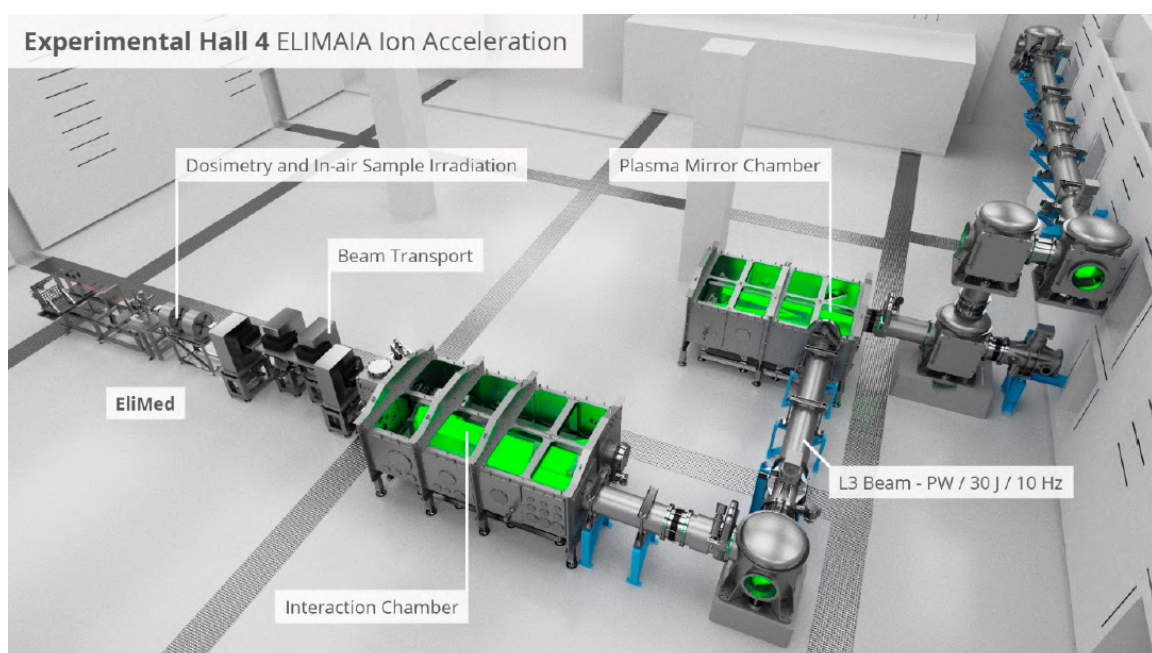

Figure 3.1: 3D rendering of the ELIMAIA beamline in experimental hall E4 [1].

The ELIMAIA beamline is located in experimental hall E4 at the basement of the ELI-beamlines facility. It consists of two main subsystems: (i) the ELIMAIA ion acceleration section and (ii) the beam transport and dosimetry section known as ELIMED (ELI MEDical applications). The beamline is served by two laser systems, called HAPLS and ATON. HAPLS is a PW-class laser with unique features with respect to other PW lasers. The main advantage of the HAPLS laser is its ability to operate up to 10 Hz repetition rate, thus making it the world's highest average power, PW laser system [1]. The ATON 10-PW laser system will also be available at the ELIMAIA hall in the future. This laser is designed to deliver extremely high peak power with shot rate 1/min and will be used to explore new acceleration regimes (e.g. RPDA).

The laser beam enters the experimental hall from the eastern wall (top right corner of figure 3.1). It is first transported through a series of elements that make up the ion accelerator sub-system. These include the double plasma mirror chamber, a laser diagnostics station and, finally, the interaction chamber in which the laser-plasma interaction and ion acceleration take place. The plasma mirror system that will be implemented in the near future will improve the laser contrast and allow irradiation of ultra-thin (< 100 nm) foils. In the laser diagnostic section (between plasma mirror and interaction chambers), a set of basic laser parameters (spatial profile and energy) are monitored in air. Inside the interaction chamber, a set of mirrors and an off-axis-parabola (OAP) transport and focus the laser beam down to a few micrometers on the target with the aid of a dedicated alignment/monitoring system. Laser pulse duration and focal spot are also monitored inside the interaction chamber. Two distinct target delivery systems can be implemented: (i) translational target tower with fast refresh rate for accommodating planar foil targets of various thickness and geometry and (ii) a cryogenic ribbon for continuous flow of a solid-H_2 slab [51] which is currently being developed. Depending on the arrangement of the different components inside the interaction chamber, the accelerated ions can be either directed to the ELIMED beam transport for application experiments or directed to an array of different diagnostic inside the interaction chamber for source development experiments. The typical arrangements of the interaction chamber for source development and application experiments are shown in figure 3.2. The experiment can be safely controlled from a shielded control room next to E4, where a suite of user-friendly software allows direct control of the equipment and online shot-to-shot monitoring of the ion beams using a range of diagnostics.
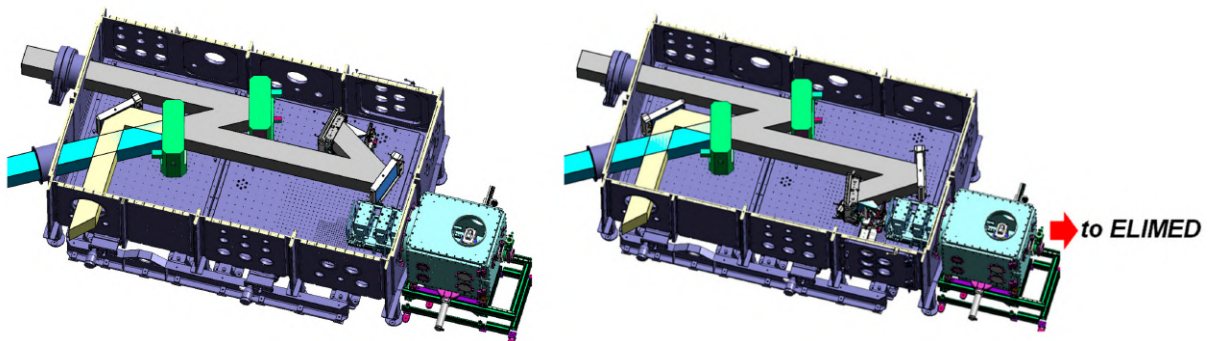

Figure 3.2: Top-down view of the interaction chamber in the configuration for source development experiments (**left**) and the configuration for application experiments (**right**). The laser beam enters from the left side (grey path) [1].

The interaction chamber is where the laser-plasma ion acceleration takes place. Pumps are used to create and maintain a vacuum inside the chamber (operational regime 10^{-6} Pa). This prevents unwanted interaction between the laser and ambient air and reduces the chance of collisions between the accelerated ions and air molecules. The target tower can be placed at different positions depending on the type of experiment. If the ion beam is needed for sample irradiation at the end of the ELIMED section, the chamber is configured as depicted in figure 3.2 right. To study laser-driven ion acceleration, the left setup in figure 3.2 is sufficient, since detectors can be mounted inside the vacuum chamber. As shown in figure 3.2, the laser enters the interaction chamber from a special window on the side. Then a series of mirrors direct the laser beam towards the OAP. The HAPLS laser is focused using a $f/1.5$ OAP and the focal spot size on the target plane is measured in order to estimate the laser intensity on target.

3.2 Ion diagnostics for laser-plasma accelerators

Many different types of detectors are required to fully characterize laser-plasma interactions and the resulting ion beams. These detectors are complimentary in the information they provide but also allow the user to cross-check the data from various detectors and calibrate them if necessary. The main diagnostics used are based on the time-of-flight (TOF) technique and on the use of either Faraday Cups (FC) or semiconductor detectors such as diamond and SiC (section 3.2.1). Another important diagnostic tool is the Thomson Parabola Spectrometer (TPS) which is able to detect energy-resolved ion spectra while discriminating ions with different charge-to-mass ratios by means of combined use of electric and magnetic fields (section 3.2.2). Finally, some other types of detectors will be briefly described in section 3.2.3.

3.2.1 Time-of-flight technique and detectors

The TOF technique is one of the most established real-time diagnostics methods as reported in literature [52]. TOF diagnostics coupled with a suitable acquisition system (oscilloscope and electronics) can permit shot-to-shot monitoring of the main ion beam properties up to a repetition rate of 10 Hz. Figure 3.3 shows a typical TOF signal and a sketch of the TOF principle.

The basic idea behind the TOF technique is that different charged species from plasma reach the detector at different times depending on their energy and mass. It is assumed that all particles (photons, electrons, protons and heavier ions) leave the target at the same time, the laser interaction time or time zero (TOF zero in figure 3.3). Different particles are accelerated to different final velocities during the interaction and therefore separate in time and space during propagation in the field-free drift region. Photons arrive first at the detector at time $t_{ph} = d/c$ and the photopeak is registered by the detector. The photon signal then decays exponentially in time (due to the oscilloscope's finite response time) until the fast protons arrive. The proton arrival is marked by an increase in the TOF signal. The inset sketch in figure 3.3 illustrates the beginning of the interaction and the separation of different ion species in space (and time) during propagation from the target to the detector. The kinetic energy of protons, for instance, is then calculated from the measured proton arrival time with respect to the photopeak (t_{ion}), knowing the flight path d and considering the time needed for UV and X-rays to travel the distance from the source to the detector ($t_{ph} = d/c$). Therefore, the time-of-flight of protons can be expressed as $\text{TOF} \equiv \text{t} = \text{t}_{\text{ph}} + \text{t}_{\text{ion}}$ and the kinetic energy can be obtained by the well-known relativistic definition [53]

$$E_p = (\gamma - 1)m_p c^2 \qquad \gamma = \frac{1}{\sqrt{1 - \beta^2}} \qquad \beta = \frac{d}{ct} \quad . \tag{3.1}$$
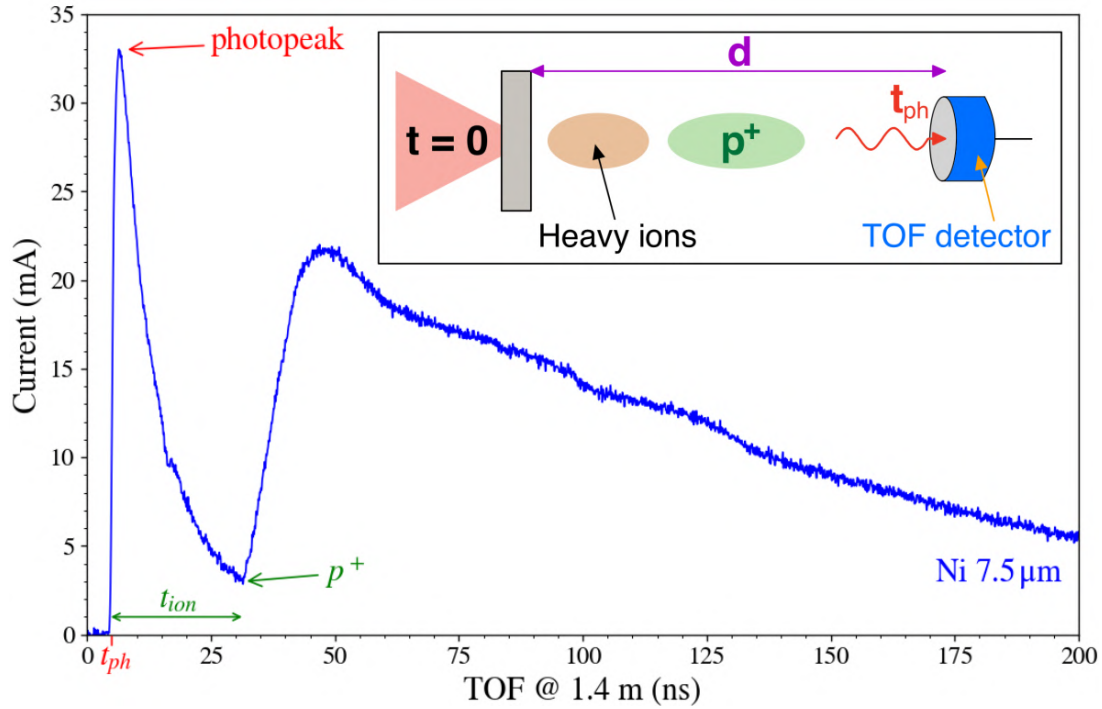
Figure 3.3: Example of TOF signal from a semiconductor detector placed $1.4\,\mathrm{m}$ from the target normal. This signal is from irradiation of a $7.5\,\mu\mathrm{m}$ Nickel foil with $I \sim 10^{21}\,\mathrm{W/cm^2}$. Top right: inset sketch of the TOF principle.

TOF detectors can be classified based on the physical quantity they are sensitive to, either the current of incident particles in the case of the FC or to the energy deposited by particles inside the detector in the case of semiconductor detectors [54]. These two types of TOF detectors are used in laser-driven ion acceleration experiments. FCs are able to detect protons up to approximately 1 MeV of energy. The reason is that FCs are highly sensitive to the electromagnetic pulse (EMP) from the interaction. The EMP results in a powerful and long photopeak which overlaps with and hides any fast proton signal. Semiconductor detectors are better for experiments with PW lasers and multi-MeV protons. Large-bandgap semiconductors can suppress the photopeak by cutting the visible and soft-UV radiation from plasma, thus enhancing the sensitivity to fast protons.

When a beam of positive ions is deposited on the surface of a good conductor (e.g. copper), it gains a small net charge. At the same time, the ions are neutralized by free electrons inside the metal which are attracted to the surface. This is the fundamental physical operation principle of the Faraday cup. If the metal collector is connected to an external circuit, it can then be discharged to measure a current proportional to the rate of arrival of impinging ions, assuming the electronic response can keep up with even the shortest beam pulses. The current signal can be recorded with high precision by a fast storage oscilloscope. Typically, a large bandwidth ($> 500\,\mathrm{MHz}$, ideally GHz level) oscilloscope with a $50\,\Omega$ load impedance is used. The separation of electrons coupled to the ion stream can be achieved by means of a static electric field that exists between either the grounded entrance grid and the negatively biased collector or the grounded entrance grid and the negatively biased control grid (see figure 3.4) [55]. This electric field slows down and stops the incoming primary electrons within distance s and prevents them from reaching the collector.

Energetic ions can cause emission of one (or more) secondary electrons from the metal surface. This process is known as secondary electron emission since a primary/incident particle of high enough energy to overcome the metal's work-function can transfer its
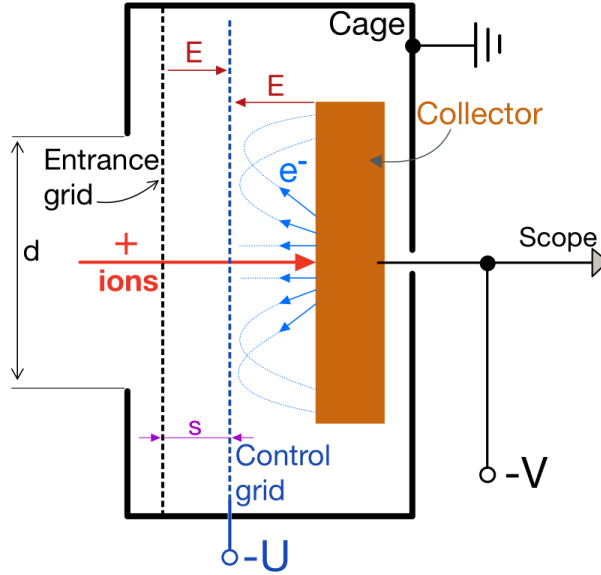
Figure 3.4: Schematic drawing of a FC. The diagram illustrates the basic components of the FC, the ion beam and the secondary electron emission. The collector is negatively biased and the cage is grounded to shield the electronics inside from the EMP [52, 55].

energy to eject a surface electron. This is a problem for the detection of positive ions because, as electrons leave the surface the positive charge on the cup (and thus also the current) becomes overestimated. There exist a number of methods to suppress secondary electron emission. We can construct the cup in a special shape (e.g. cone), in order to confine secondary electrons to the cup or introduce active electrostatic suppression of secondary electrons in the form of a control grid, as shown in figure 3.4.
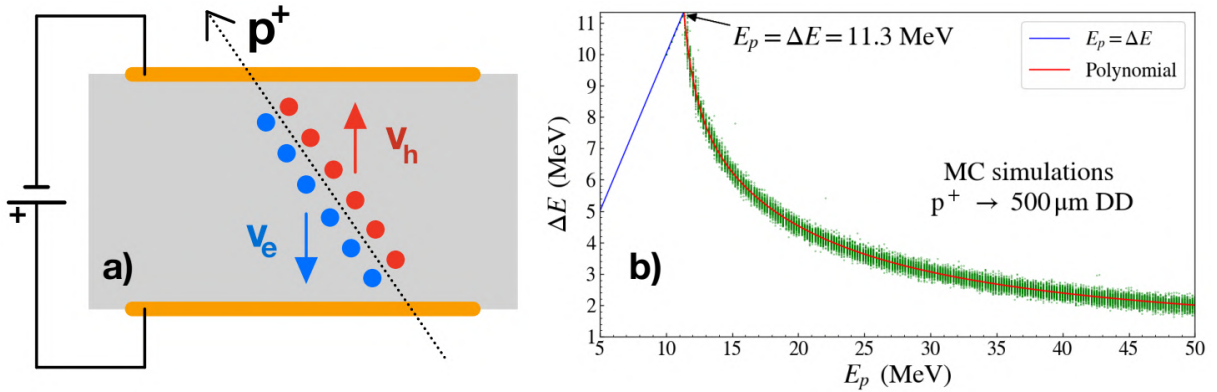

Figure 3.5: Operation principle of a semiconductor detector. a) Electron-hole pair creation and drift. b) SRIM/Monte-Carlo simulations [56] for the energy deposition in diamond. E_p is the incident energy of protons before entering the active layer and ΔE is the deposited energy inside the active layer.

Semiconductor detectors operate on the principle that particles will lose energy inside the active layer by generating electron-hole pairs until they are stopped or pass through (figure 3.5a). The number of electron-hole pairs is proportional to the energy released by the particles inside the active layer. As a result, a number of electrons are transferred from the valence band to the conduction band, and an equal number of holes are created in the valence band. Under the influence of an electric field, electrons and holes drift to opposite electrodes and a current pulse can be measured in an outer circuit. Typical bandgap values are of the order of $1-10\,\mathrm{eV}$, so a proton with energy $1\,\mathrm{MeV}$ will create $\sim 10^5 - 10^6$

electron-hole pairs before it stops (assuming the detector material is thick enough to stop such a proton). By applying a voltage on the faces of the active layer, these electrons and holes drift to opposite electrodes and current flow is observed. Consequently, the current response of such detectors is proportional to the energy deposition rate inside the active layer. Two semiconductor detectors that have been tested extensively in laser-ion acceleration experiments are Silicon Carbide (SiC) and Diamond Detectors (DD) [52].

Having obtained the TOF signal, we can evaluate the energy spectrum of the ions, which provides information on the number of ions and the cutoff energy. The energy spectrum reconstruction process differs between FC and semiconductor detectors because of the different physical mechanisms involved in the detection process. For a FC the proton energy spectrum can be obtained by transforming the current signal in the following way:

$$E_p = \frac{m_p d^2}{2t^2} \quad \Rightarrow \quad \frac{\mathrm{d}N_p}{\mathrm{d}E_p} = \frac{\partial N_p}{\partial t}\frac{\partial t}{\partial E_p} = \frac{d m_p^{1/2} i(t)}{e(8E_p)^{3/2}} . \tag{3.2}$$

Thin metal foil filters are often placed in front of FC to stop heavy ions and suppress the low-energy light particles. The only effect of these filters on FCs is to set the minimum detectable proton energy. For a filter of certain material and thickness, the maximum proton energy that can be stopped by the filter can be estimated using Monte-Carlo simulations. Otherwise, such filters have no effect on the FC energy spectrum reconstruction process because FCs are sensitive to charge, not energy.

The energy spectrum reconstruction process is significantly more complicated for semiconductor detectors because of their energy sensitivity. The detector response is a function of incident proton energy E_p (and thus time) and can only be estimated using Monte-Carlo simulations. One such simulation is illustrated in figure 3.5b for protons incident on $500\,\mu$m DD. The charge collected in semiconductor detectors due to N_p incident protons, depositing energy $\Delta E \equiv f(E_p) \equiv g(t)$, is expressed as

$$Q = \frac{eN_p(\Delta E)}{\epsilon_g} \quad , \tag{3.3}$$

where ϵ_g is the electron-hole pair creation energy or bandgap ($\epsilon_g = 13\,$eV for diamond). By performing the derivative of the previous equation with respect to t, it is possible to obtain the proton energy spectrum for a semiconductor detector:

$$\frac{\mathrm{d}N_p}{\mathrm{d}E_p} = -\frac{\epsilon_g\, i(t)\, t}{2e(\Delta E)^2} \quad . \tag{3.4}$$

Additional filters placed before a semiconductor detector must also be taken into account during the energy spectrum reconstruction process. For a certain time t, the energy of protons incident on the active layer is not simply $m_p d^2/2t^2$ but is, in fact, the residual kinetic energy after passing through the filter. In this case, ΔE is a function both of t and filter thickness/material. Monte-Carlo simulations can be used to calculate the minimum energy a proton must have in order to pass through the filter and the residual energy after the filter. For example, SRIM simulations [56] show that protons with energy $3\,$MeV or less are completely stopped by $50\,\mu$m Al foil but a $6.5\,\mu$m Al foil only stops protons with energy up to $0.5\,$MeV.

Figure 3.6 shows an example proton spectrum reconstructed from the TOF signal of a DD after irradiation of a $12\,\mu$m Al foil using a PW laser. Notice that the minimum detectable energy of protons is $0.5\,$MeV due to a $6.5\,\mu$m Al filter placed in front of the detector. The energy spectrum can provide information on the number of protons in any energy range (area under the spectrum) and the proton cutoff/maximum energy (sharp drop at $13\,$MeV).
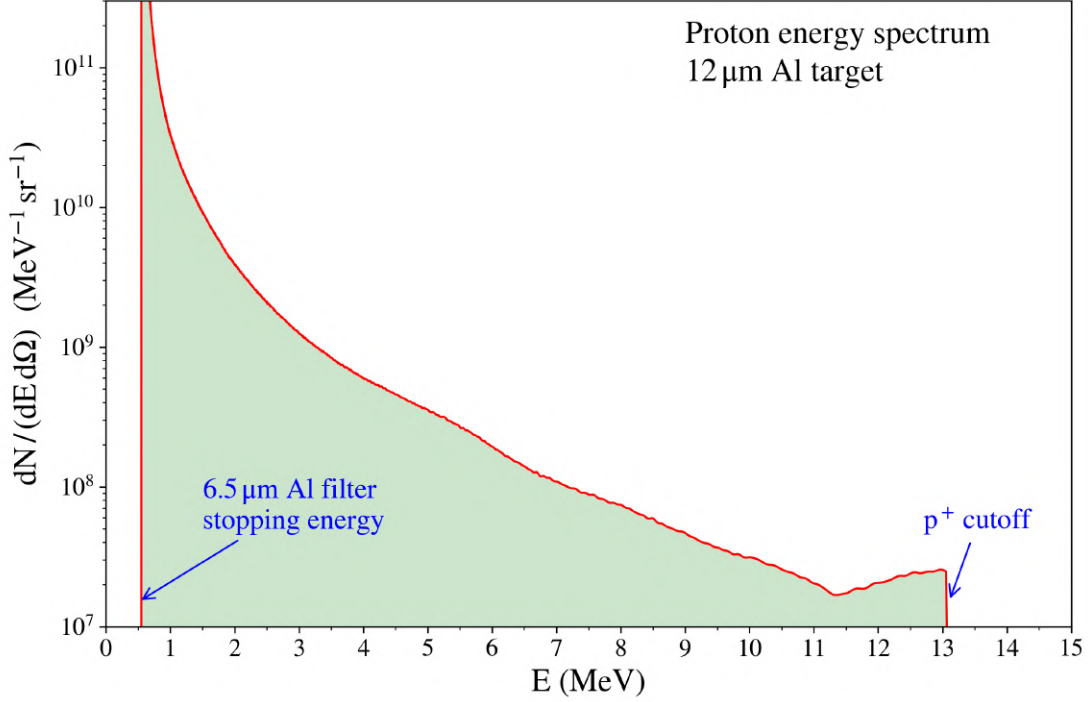
Figure 3.6: Proton energy spectrum reconstruction from a diamond detector (with $6.5\,\mu$m Al filter) placed $1.4\,$m from the target normal. This data is from irradiation of a $12\,\mu$m Al foil target using intensity $I \sim 10^{21}\,\text{W/cm}^2$.

3.2.2 Thomson Parabola Spectrometer

The main components of the the Thomson Parabola spectrometer (TP) are shown in figure 3.7a. In TP, the ion beam is selected by a pinhole located at its entrance. The charged particles travels through regions of parallel magnetic and electric fields (red and blue regions in figure 3.7a) applied transversely to the beam axis and are deflected by the Lorentz force $\mathbf{F} = q(\mathcal{E} + \mathbf{v} \times \mathcal{B})$ [55]. Deflected ions are observed and amplified by means of a micro channel plate (MCP) and are sent to a phosphor screen, thus producing an image of the energy-resolved ion spectra. This image can subsequently be recorded by a CCD camera. Several other detectors can be used instead of MCP. The TP can also be fitted with radiochromic films (RCF) or an Imaging Plate (IP). The Thomson parabola spectrometer is used as a charged particle analyzer for the quantitative analysis of ion beams emerging from a laser-plasma. The deflection of charged particles in homogeneous magnetic and electric fields provides simultaneously their energy, momentum, and mass-to-charge ratio [57].

From the solution of the motion equation of a charged particle entering at the normal direction into the region of parallel fields, $\mathcal{E}$ and $\mathcal{B}$, we can obtain the coordinates of the points in which the ions of some parameters (charge-state Z, mass m and energy E) will be located in the recording plane:

$$\left(x = \frac{\beta eZ|\mathcal{B}|}{\sqrt{mE}} \,,\; y = \frac{\alpha eZU}{E} \right) \quad \Rightarrow \quad y = \frac{m}{Z} \cdot \left(\frac{\alpha U}{\beta^2 e\mathcal{B}^2} \right) x^2 \;. \tag{3.5}$$

Variable U is the potential difference between the electrostatic deflecting plates while α and β are geometrical constants of the TP. These coordinates define distinct parabolas; all particles of identical mass-to-charge (m/Z) ratio are found on one of these parabolas, with ions of higher energy being located closer to the center of the screen, meaning they are deflected less. Figure 3.7b shows a TP image where tracks of different ion species are clearly separated on different parabolas.
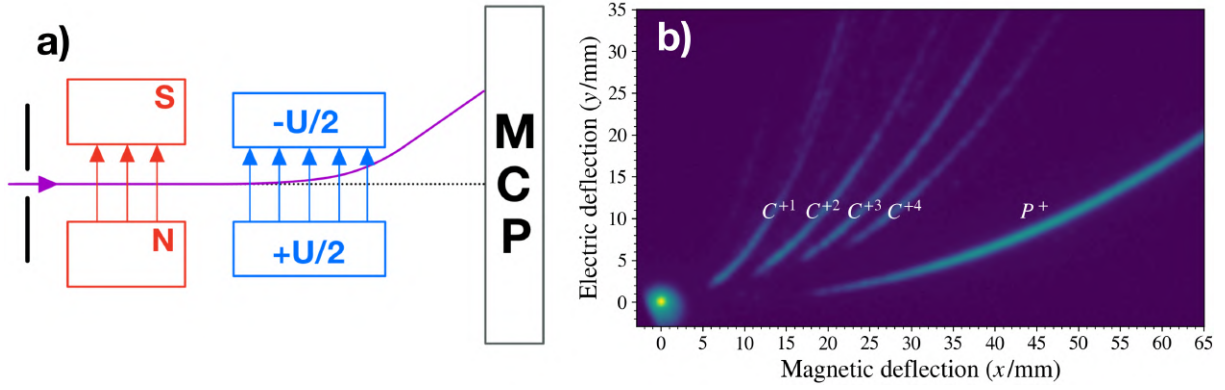
Figure 3.7: Operation principle of the Thomson parabola spectrometer. a) Schematic of the main components including the pinhole, permanent magnets (red), electrodes (blue) and micro channel plate (MCP). b) Example image recorded by TP. The bright spot at the origin (undeflected trajectory) is due to photons, while protons and carbon ions are found in the annotated parabolas.

From relation 3.5, it should be observed that a fixed y coordinate corresponds to a fixed ratio $E/Z = \alpha eU/y = const.$ on all parabolas. Moreover, points of different parabolas lying on a vertical line ($x = const.$) share the common ratio $m\mathrm{v}/Z = \sqrt{2}\beta e|\mathcal{B}|/x$. Finally, the points of intersection of parabolas with the line $y = cx$ (i.e. any line passing through the origin) correspond to ions of fixed velocity, $\mathrm{v} = \sqrt{2}(\alpha/\beta)(U/|\mathcal{B}|)(x/y)$.

The main parameters of the ELIMAIA TP are as follows: the diameter of the pinhole is set to be $200\,\mu$m. The permanent magnets are $5\,$cm in length and allow reaching a magnetic field strength of about $1.2\,$T. The maximum voltage that can be applied on the $20\,$cm long electrodes is $\pm15\,$kV. The MCP is $77\,$mm in active diameter and consists of a lead glass plate including an array of electron multipliers with $21\,\mu$m tube diameter. The channel axes are biased by a small angle ($6°$) to optimize secondary electron emission in the channels [1]. Note that the TP also has a minimum energy of protons it can detect. This minimum energy depends on the spatial extent of the MCP and the strength of the deflecting fields used.

3.2.3 Passive ion detectors

Passive detectors are also important because they provide unambiguous measurements of maximum ion energy, charge and beam divergence and can therefore be used to cross-calibrate the measurements performed by active detectors (e.g. TOF and TP diagnostics) [1]. It is common practice for laser-driven ion acceleration to use radiochromic films (RCF) and nuclear track detectors (typically CR39). It is also possible to use such detectors in stack geometry to provide a rough measurement of the ion energy spectrum. These detectors operate on the principle that some materials, when exposed to ionizing radiation, undergo chemical reactions which change their physical appearance permanently. Below we briefly discuss the processes that allow these materials to detect energetic particles and their advantages compared to other diagnostics.

Charged particles passing through certain materials (such as organic polymer plastics) produce microscopic trails (less than $10\,$nm in diameter) of continuous damage along their path. These trails consist of broken polymeric bonds, forming a so-called latent track. The length of damage trails is equal to the range of the particle in the medium under consideration. No track formation occurs, unless the rate of energy dissipation exceeds a critical value. These latent tracks can be observed under an optical microscope after chemically etching the material because the damaged parts of the material react more

intensely with the etching agent than the undamaged parts. The track position shows where the particles were incident, and the track diameter will depend on the incident energy and how the material is processed. Before these parameters can be used to discriminate the particles produced by a high-intensity laser experiment, the detector must be carefully calibrated in experiments with particles of well-known energy, to determine the relationship between the etching parameters (etching time, temperature, solution concentration etc) and the measured dimensions for any type of particles [58, 59].

The CR39 polymer has been widely employed as a nuclear track detector. CR39 is a clear and rigid plastic polymer. When particles enter normally to the surface of the CR39, the track forms a conical pit after etching in chemical solutions (e.g. NaOH or KOH). As long as the etching depth is smaller than the particle range, the diameter and depth of the track increase with the increase in etching time [59]. An advantage of CR39 detectors is that they are not sensitive to EMPs or X-rays. It also has a high spatial resolution and wide dynamic range. However, they require careful calibration and a considerable time and effort before any results are obtained. Figure 3.8 shows sample CR39 images recorded using a microscope and the corresponding calibration curves. Notice how the track diameters depends on the incident energy and the etching time in solution. Finally, it is also possible to stack multiple CR39 layers for energy resolved measurements.
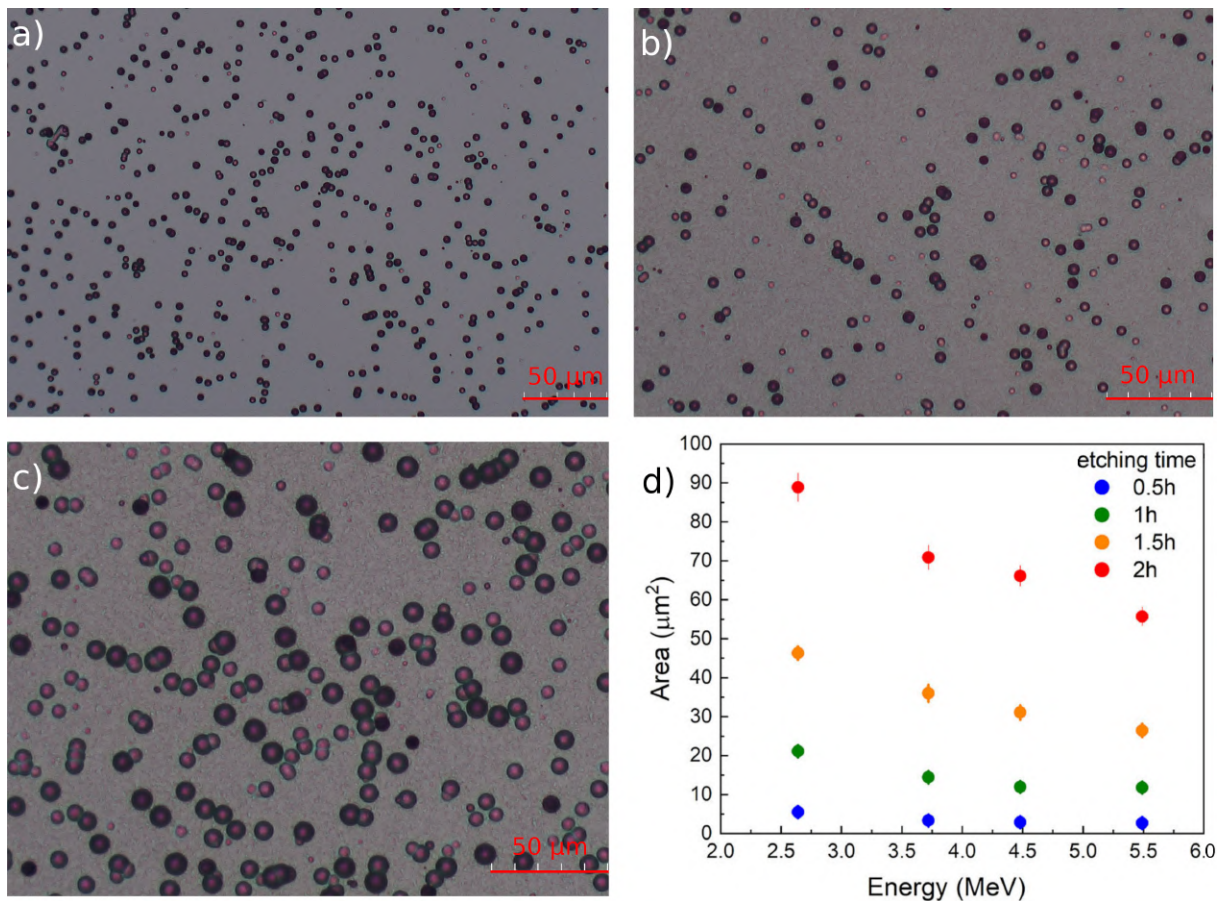

Figure 3.8: Example of CR39 showing α-particle tracks at the optical microscope after (a) 60 min, (b) 90 min and (c) 120 min etching. (d) Calibration curves for CR39 etched using KOH 6M solution at 70°C with α-particles emitted by a $241Am$ source [60].

Radiochromic dosimeters are frequently used for ion beam characterization (energy spectrum and spatial beam profile). They are part of a broader family of detectors known as coloration detectors. RCFs are increasingly being used in a range of applications for the measurement of 2D dose distributions and give 2D ion beam spatial profile with good spatial resolution. When exposed to radiation, the active material in these films undergoes a polymerization reaction, which results in a chromatic (color) change depending on their specific composition. The feature of RCFs that makes them so useful as a dosimeter is that the amount of color change or darkening is proportional to the absorbed dose. Ionizing radiation dose is measured in units of Gray (Gy) and is defined as the absorption of one joule of radiation energy per kilogram of matter. After exposure, the films can be scanned and the images analyzed with image processing software. Similarly to CR39 detectors, RCFs also need to be calibrated using ion beams of known energy. Film colorization is quantified in terms of the fraction of incident light which is transmitted by the film [61, 62]. A widely used RCF is known as GAFchromic^{TM}, based on polydiacetylene. All currently available forms of this film consist of basically the same sensitive emulsion and differ in film construction and emulsion thickness, resulting in different sensitivity to the radiation dose, radiation type and energy. Some commonly used film types are the XR, EBT, MD and HD models.

Figure 3.9: Example of EBT stack irradiated with one shot during the ELIMAIA commissioning experiment. Layer **1** is at the front and layer **6** at the back. The films are also annotated with the absorbed dose in cGy. A $45\,\mu$m Al filter was placed in front of the stack to block heavy ions and low energy protons.

RCFs are often layered into a stack with metal filters. Typically, protons are the only ions to propagate beyond the very front of the stack due to their lower rate of dose deposition, and so RCF stacks are mainly useful in characterizing large energy spread proton beams [63]. Low energy protons are stopped early in the stack whereas high-energy protons deposit little energy in the front layers of RCF due to their energy deposition pattern dominated by a Bragg peak (i.e. assume a proton deposits all its energy at the point in the stack where it stops). The physical reason is that the energy loss is dominated by Coulomb collisions for which the cross section strongly grows with decreasing energy, so that the stopping process becomes progressively more and more efficient [2]. Hence the beam profile in any given layer is dominated by protons close to their stopping range in that piece of film. Knowing the stopping power of the radiation in each layer (using for example Monte-Carlo simulations), we can accurately estimate the energy of particles deposited in each layer. With sufficient layers of RCFs a spatially resolved ion spectrum can be retrieved [63]. An example of a RCF stack is shown in figure 3.9.

Many more specialized diagnostics are available at the ELIMAIA beamline. These include optical probes, electron spectrometers, X-ray cameras, electromagnetic probes and target current probes. These tools are important for a complete understanding of the laser-plasma interaction but are not directly related to the detection of laser-accelerated ions. Therefore, these diagnostics will not be discussed further in this thesis.

Chapter 4

ELIMAIA commissioning experiment and particle-in-cell simulations

This chapter is concerned with the commissioning experiment of the ELIMAIA beamline laser-plasma accelerator, using the high-repetition-rate, high peak-power HAPLS laser system. This experiment was carried out over several weeks in the fall of 2021 with the aim of optimizing the ion accelerator performance. The laser beam (10 J, 30 fs) was tightly focused ($\sim 2\,\mu$m FWHM) to reach ultrahigh intensity on target ($\sim 10^{21}\,$W/cm^2). The performance of thin Aluminum foil targets ($2 - 25\,\mu$m) was investigated and assessed. The proton beam characteristics were monitored using a complete set of ion diagnostics. In the following pages, the most important results from Diamond Detector (DD) and Thomson Parabola (TP) diagnostics are presented and later interpreted with the help of 2D particle-in-cell simulations.

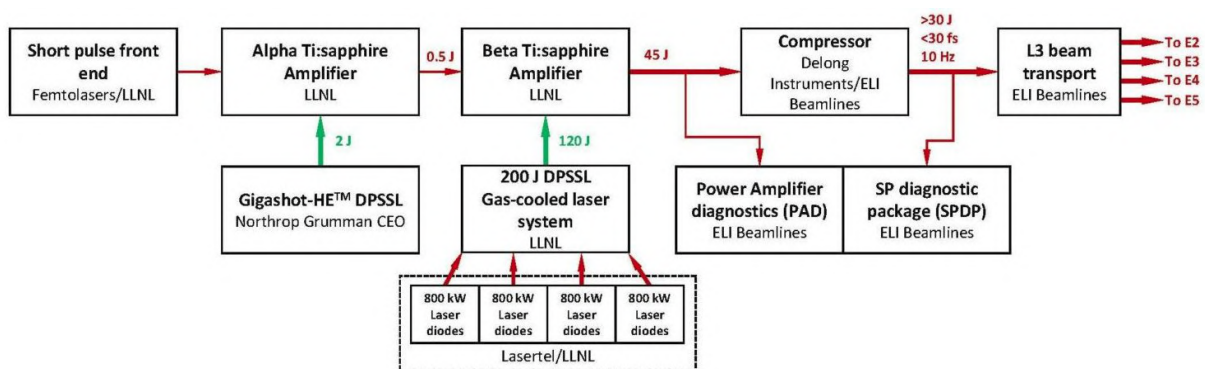## 4.1 High-Rep-Rate Advanced PW Laser System

Figure 4.1: Block scheme of the HAPLS laser. All pump units use DPSSL (Diode-Pumped Solid-State Laser) technology providing the system with high pulse-to-pulse stability, robustness, low maintenance and scalability to higher peak power and rep rates [64].

The laser system called HAPLS (for High-Repetition-Rate Advanced Petawatt Laser System), is designed to deliver PW pulses with energy of at least 30 J and duration < 30 fs, at a repetition rate of 10 Hz. It is the first all diode-pumped, high-energy femtosecond PW laser system in the world. The laser was developed at the Lawrence Livermore National Laboratory, with ELI-Beamlines cooperating on the development of the short-pulse diagnostics and of the short-pulse subsystem controls and timing [64].

This laser achieves ultrashort pulses with high peak power by using a mode-locked Ti:Sapphire seed oscillator and Chirped Pulse Amplification through a chain of amplifiers. The PW vacuum compressor of the laser has size of approximately $5.2 \times 2.4 \times 2.2\,$m and besides diffraction gratings includes a number of optical, optomechanical and

Table 4.1: Design parameters for HAPLS.

Output pulse energy	$> 30\,\text{J}$
Repetition rate	$10\,\text{Hz}$
Peak power	$1\,\text{PW}$
Pump technology	DPSSL
Pulse duration	$< 30\,\text{fs}$ FWHM
Short pulse technology	Ti:sapphire & CPA

electro-optical elements [64]. The design parameters of the HAPLS laser are given in the table above. Some of these parameters have not yet been achieved. The exact laser parameters used in the commissioning experiment will be discussed in the next section.

4.2 Experimental arrangement

During the commissioning experiment, the interaction chamber was set-up as shown schematically in figure 4.2. In this configuration, the accelerated ions are not directed towards that ELIMED section but are instead detected by diagnostics mounted in or around the interaction chamber. Laser pulses from HAPLS were tightly focused on thin Aluminum foil targets using an off-axis parabola (OAP) having f-number of 1.5 (focal length is around 30 cm), to reach an estimated peak intensity above $10^{21}\,\text{W/cm}^2$ in FWHM on target. The incidence angle relative to the target normal was 15° and the laser beam was s-polarized. A set of diagnostics were positioned all around the target to monitor the interaction, including RCF and CR39 detectors placed inside the chamber. DD1 was placed on the rear side at a distance of 1.39 m along the target normal. Data from this DD will be presented later in this chapter. The entrance of DD1 was covered with either 6.5 μm or 50 μm Aluminum filters, which can stop protons with energy lower than 0.5 MeV and 2 MeV, respectively. These filters were used to cut low energy protons and heavier ions, in order to reduce the risk of saturating the detector signal with a large number of low-energy particles. The TP was also placed on the rear side. Data from the TP will also be presented later in this chapter. Filters are not needed in the case of the TP because this diagnostic can separate photons and different ion species. More importantly though, the TP has a series of pinholes that reduce the number of particles reaching the detector, so there are no saturation issues. Additionally, the laser-target interaction and plasma features were characterized through various other optical and X-ray diagnostics.
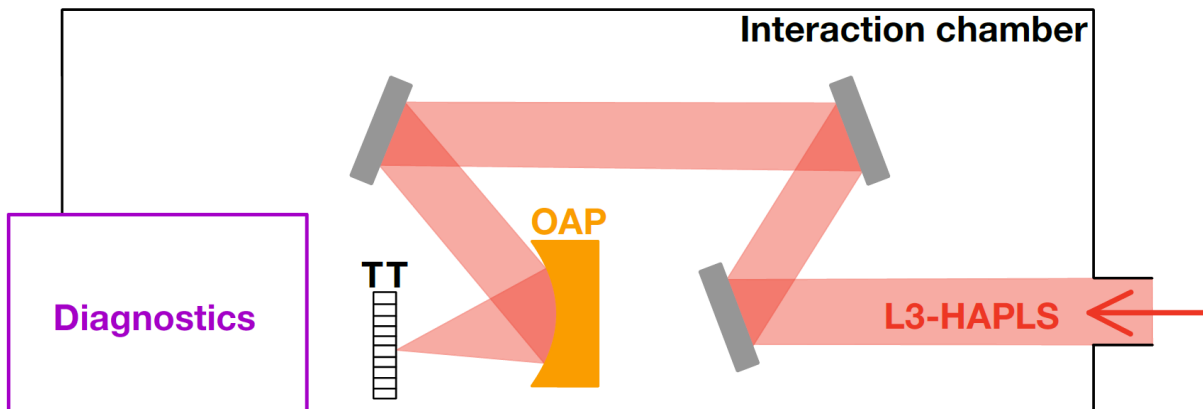

Figure 4.2: The experimental setup used for the commissioning experiment. The abbreviation TT stands for the target tower where thin foil targets are mounted and OAP is the off-axis parabola that focuses the laser.

The main pulse has maximum delivered energy $\sim 10\,\mathrm{J}$ and pulse length $\sim 30\,\mathrm{fs}$. The main laser pulse was focused down to $\sim 2\,\mu m$ FWHM and during the experiment, most laser pulses were delivered in single shot mode. An image of the alignment laser intensity profile in focus is shown in figure 4.3. This alignment laser is low power and only used during the alignment phase. The laser shows good focusability with small focal spot on target (FWHM), reaching intensity $10^{21}\,\mathrm{W/cm^2}$ at 10 J energy. However, only a small amount of this energy (around 20%) is encircled inside the FWHM main spot. In the temporal domain a number of prepulses have been observed. Two prepulses were measured at $10\,\mathrm{ns}$ and $7\,\mathrm{ns}$ before the main pulse. These prepulses appear as short pulses with duration below the photodiode response time ($\sim 1\,\mathrm{ns}$). Moreover, there is an ASE pedestal starting a few nanoseconds ($\sim 6\,\mathrm{ns}$) before the main pulse (exact timing is determined by the HAPLS Pockels cell delay and response curves) and growing rapidly in time. The intensity contrast of ASE to the main pulse has been measured as $\sim 2 \times 10^{-9}$. Consequently, it is expected that a preplasma will form in front of the target before the main pulse arrives. The exact density profile and scale-length of this preplasma is hard to estimate without more information on the ultrashort prepulses (measured at 10 ns and 7 ns before the main pulse). Moreover, it is known that prepulses can also cause a rear-side plasma to form. A more thorough investigation of the effect of prepulses on the target would require hydrodynamic simulations.
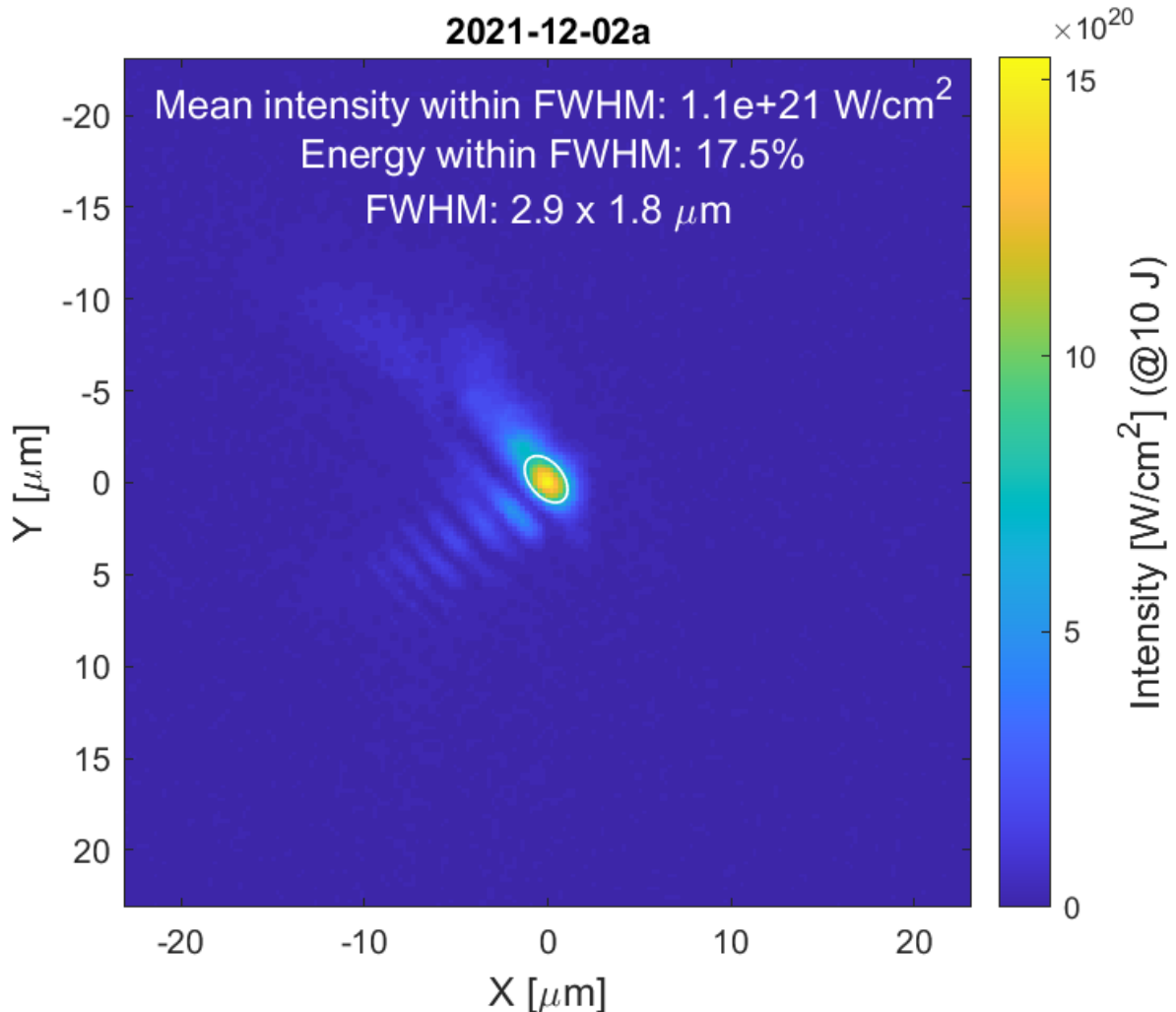

Figure 4.3: Image of the low-power alignment laser intensity profile at the focus. The white contour marks the FWHM intensity level and the values are calculated for a 10 J pulse with duration 30 fs FWHM.

4.3   DD and TP data analysis

In this section, the experimental methodology will be described, followed by the presentation and discussion of the data analysis from diamond detectors (DD) and Thomson parabola (TP) diagnostics. Aluminum thin (μm) foil target is one standard target type used in the field of laser-driven ion acceleration. The aim of this experimental work was to optimize the fast proton signal while trying to understand and minimize any possible negative preplasma effects. The philosophy of this experiment relies on using targets of different thicknesses and defocusing the laser beam. The thickness scan defines the optimal thickness that minimizes the preplasma effects. For each thickness, defocusing the beam (relative to the target surface) is used to modulate the laser intensity on target and reduce the prepulse intensity, in order to optimize and minimize the preplasma effects. This methodology leads to the most favorable conditions for proton acceleration. The maximum (or cutoff) ion energy is arguably the most important figure-of-merit for laser-driven ion acceleration experiments and is therefore used to compare different experimental conditions. Additionally, the total particle flux (number of particles per shot per unit solid angle) is a quantity of interest.
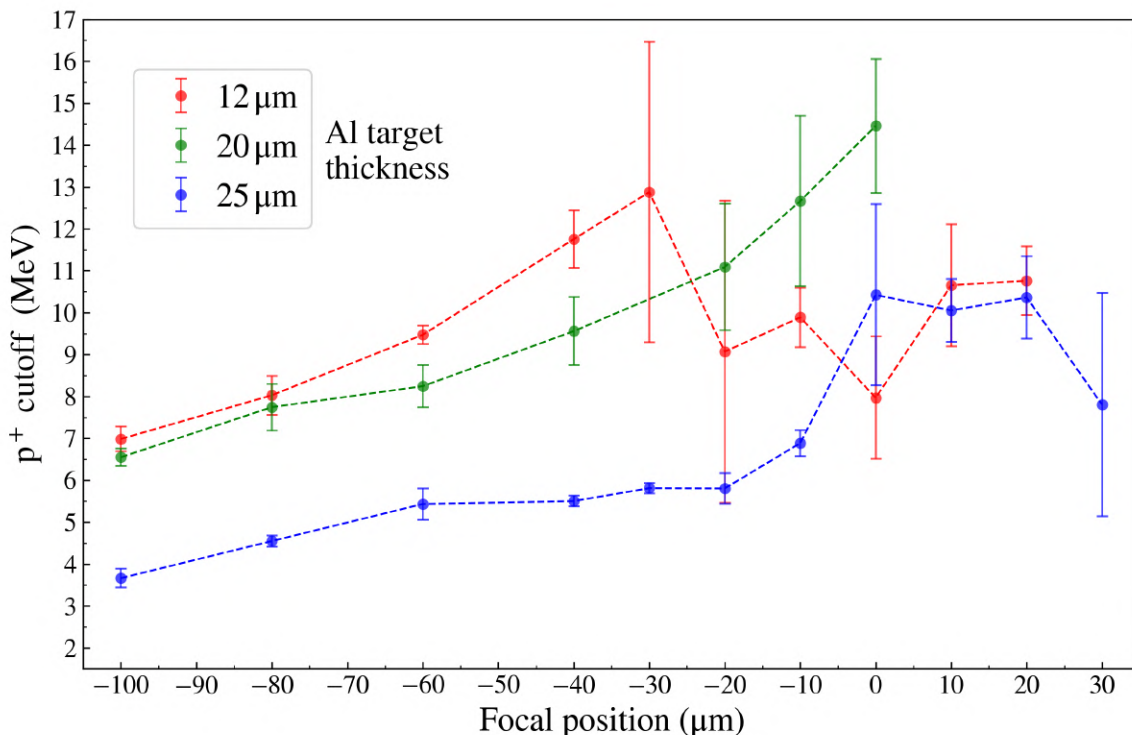

Figure 4.4: Focal position scan using 10 J, 30 fs laser pulse for three Al target thicknesses. The 0 point marks the surface of the target, as determined by the alignment and monitoring system. The negative direction corresponds to front side (laser side). Each datapoint is averaged over $5 - 10$ laser shots. Data from DD1.

The focal position of the laser beam relative to the target surface is a crucial parameter for the laser-plasma interaction. Firstly, the state of the preplasma depends on the focusing of the prepulses. For example, if the prepulse is focused on the target surface, a longer preplasma would be expected due to the higher intensity on target. Secondly, the hot electron temperature is a function of the laser intensity, so it is important that the main pulse is focused somewhere where this heating can take place effectively. A large part of the electron heating inside the preplasma occurs near the relativistic critical density surface where electron density is high. Thus, it is reasonable to assume that the laser energy coupling to hot electrons will be most efficient if the laser is focused in the vicinity of that critical surface. An additional effect that has to be taken into account is self-focusing in preplasma [65]. This can give rise to even higher intensities but it can also shift the position of the focus. Consequently, the focal position affects the laser-plasma interaction in various significant ways and should therefore be optimized for any target thickness.

The process of optimizing the proton acceleration for different target thicknesses using this focusing method is demonstrated in figure 4.4. In all cases, the maximum proton energy increases as the focal spot moves towards the surface of the target (0 point). For $20\,\mu$m Al, the proton cutoff energy increases from around $6.5\,$MeV ($-100\,\mu$m) to around $14.5\,$MeV ($0\,\mu$m), an energy enhancement of $8\,$MeV. However, the behaviour is not identical for different thicknesses. For the $12\,\mu$m Al target, the best results are achieved when focusing around $-30\,\mu$m. For the $20\,\mu$m and $25\,\mu$m Al targets, the highest proton energies are closer to $0\,\mu$m. This highlights the importance of finding the best focal position individually for each thickness. Another point to note is that as the focal position moves to more positive values, the error bars on the maximum proton energy increase and get especially large for specific values close to 0. For example in the case of $20\,\mu$m Al, the level of fluctuations in the proton energy is 4% at $-100\,\mu$m but gradually increases to as high as 20% for $-10\,\mu$m. This energy instability suggests that there are strong preplasma effects. Additionally, the $12\,\mu$m target shows stronger fluctuations compared to the thicker targets (around 40% for $-20\,\mu$m, energy range $5.5 - 12.5\,$MeV). In comparison, for the $20\,\mu$m target at $-20\,\mu$m, the energy range is much smaller (around 14% fluctuation between $9.5 - 12.5\,$MeV). This highlights the importance of studying the effect of thickness during the optimization process.
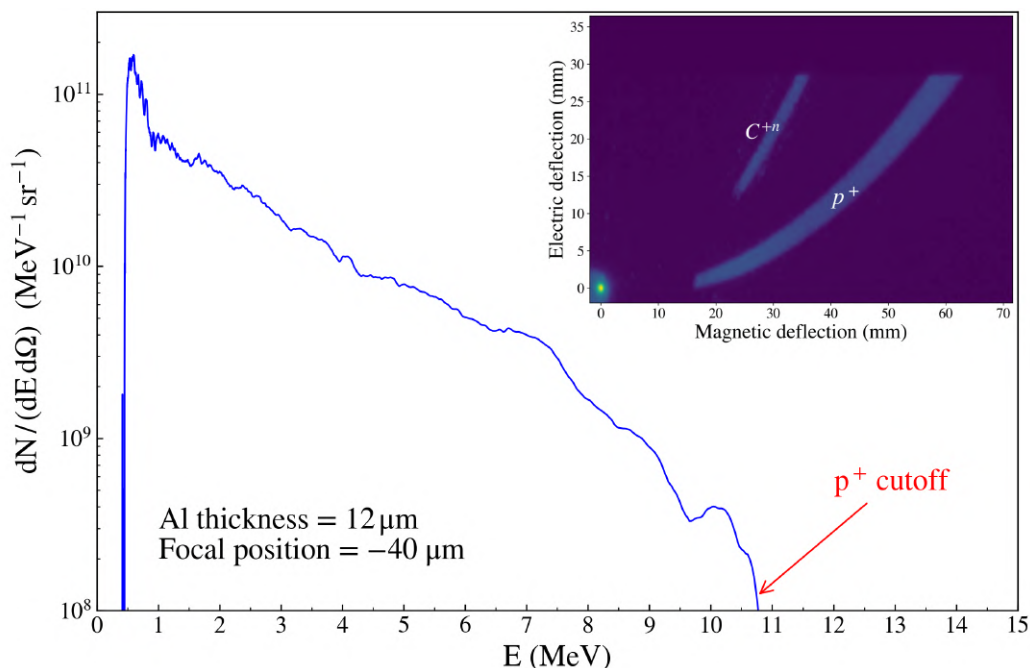

Figure 4.5: Proton energy distribution obtained from Thomson Parabola inset image.

A sample energy distribution obtained from a TP image is shown in figure 4.5. The raw image data is analyzed using dedicated software which is cross-calibrated with other ion diagnostics. The shot presented here is using a $10\,\mathrm{J}$, $30\,\mathrm{fs}$ laser pulse focused at $-40\,\mu\mathrm{m}$ relative to $12\,\mu\mathrm{m}$ Al. The proton energy cutoff can be identified as the point where there is a sudden, sharp drop in the spectrum. In this case the cutoff energy is around $11\,\mathrm{MeV}$, which agrees with the results from DD1 for the same laser shot. The energy distribution has a broad profile up to the cutoff energy, which is a typical signature of the TNSA mechanism. The vast majority of protons is found in the range $0.5 - 3\,\mathrm{MeV}$. Higher energy protons have flux which is orders of magnitude lower.
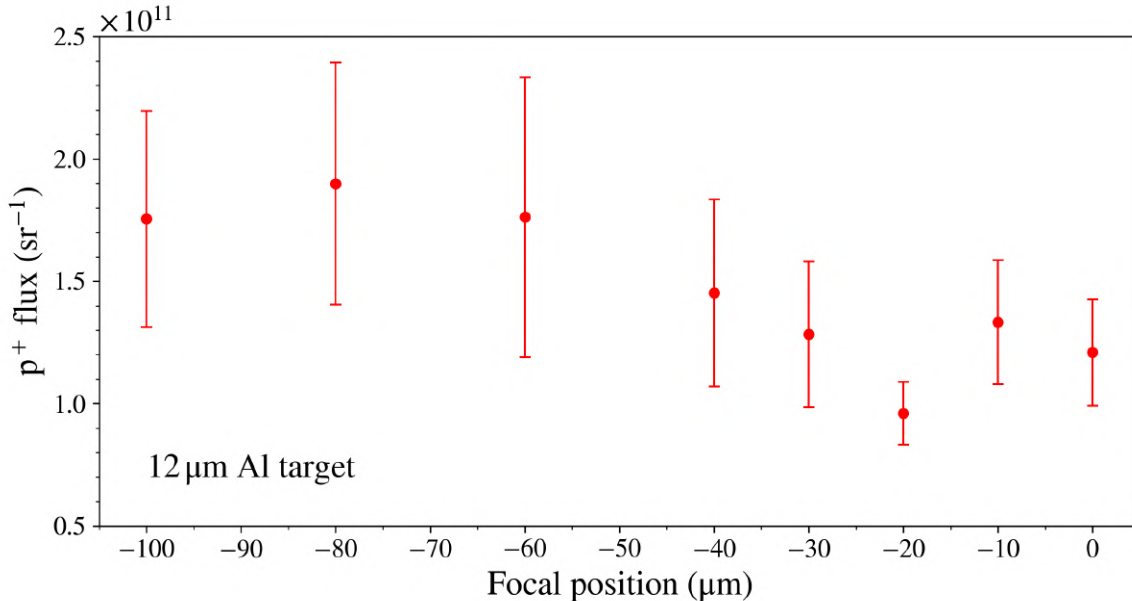

Figure 4.6: Proton flux vs focal position scan using $10\,\mathrm{J}$, $30\,\mathrm{fs}$ laser pulse on $12\,\mu\mathrm{m}$ Al target. Each datapoint is averaged over $5 - 10$ laser shots. Data from TP.

The total flux of protons can be calculated by integrating the area under the energy distribution. Figure 4.6 shows the dependence of the proton flux on the focal position for the $12\,\mu\mathrm{m}$ Al target. The flux seems to be approximately constant with focal position, when taking into account the large fluctuations (up to 25%) in the data. Therefore, the focal position appears to have little impact on the proton flux. A similar behavior in observed with other thicknesses. It is found that the proton flux for all experimental conditions fluctuates between 1×10^{11} p$^+$/shot/sr and 2×10^{11} p$^+$/shot/sr, with no obvious dependence on the parameters (thickness, focal position). The only exception to this is the $2.4\,\mu\mathrm{m}$ Al target, for which the flux drops by one order of magnitude to $\sim 1 \times 10^{10}$ p$^+$/shot/sr. This is an indication that the ASE pedestal causes partial target destruction in the case of the thinnest target, making the TNSA process less efficient.

Figure 4.7 shows the variation of maximum proton energy with thickness for three different focal positions. For focal position $0\,\mu\mathrm{m}$ proton energy increases with increasing thickness, from around $2\,\mathrm{MeV}$ for $2\,\mu\mathrm{m}$ Al up to $14.5\,\mathrm{MeV}$ for $20\,\mu\mathrm{m}$ Al, where it reaches a maximum. This kind of thickness scaling which shows better results for thick targets again suggests strong preplasma effects. For the other two focal positions ($-40\,\mu\mathrm{m}$ and $-100\,\mu\mathrm{m}$), this pattern is less pronounced and the maximum proton energy seems to be around $12\,\mu\mathrm{m}$ Al. This information can reveal important clues about the interaction.

The choice of target thickness depends on many factors but the main factor is laser contrast. The main problem for low-contrast laser pulses is target destruction. If the target is too thin, the entire target can be reduced to an underdense plasma before arrival
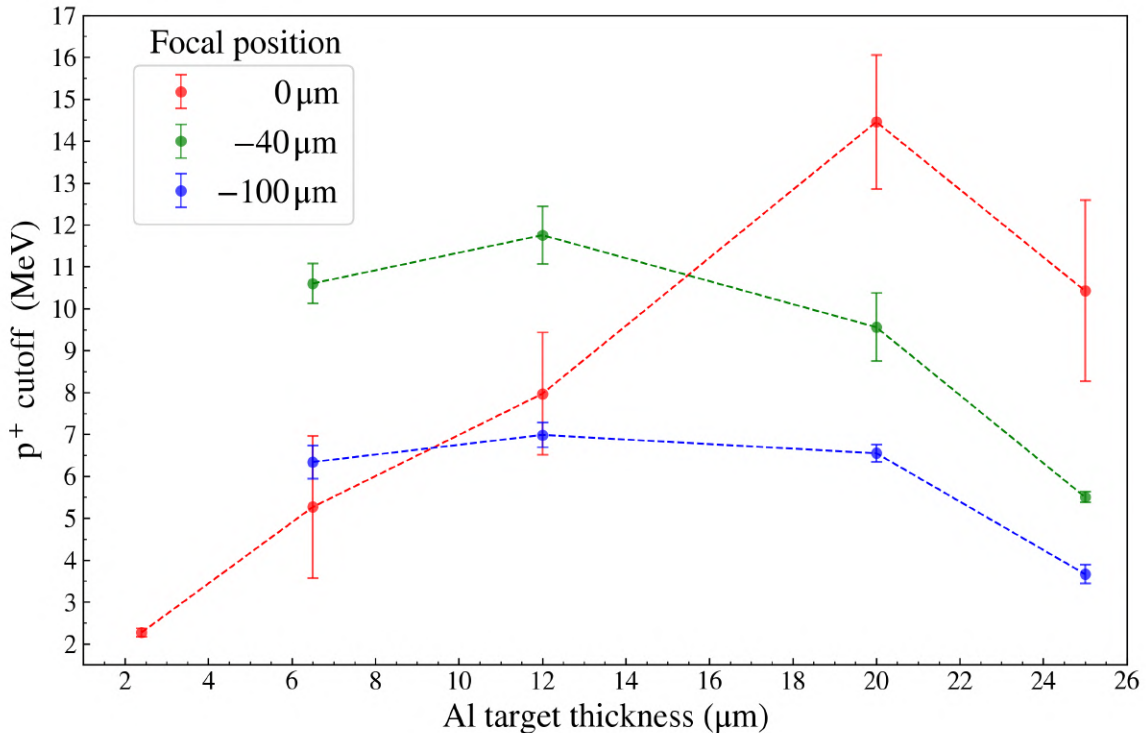
Figure 4.7: Thickness scan using 10 J, 30 fs laser pulse focused on three different positions relative to the target. Each point is averaged over $5 - 10$ laser shots. Data from DD1.

of the main pulse, in which case proton acceleration would effectively stop. On the other hand, if the target is sufficiently thick to sustain a high-density (overdense) plasma after the prepulse, then rear-side plasma plays an important role. In this case (figure 4.7) it is not obvious from the data alone which other effects are competing with target thickness. There must be strong front side preplasma effects due to the ASE pedestal. However, the possibility of rear-side plasma for thinner targets cannot be excluded.

Returning back to figure 4.7, the best target thickness appears to be $20\,\mu m$ because the energy is the highest for focal position $0\,\mu m$. However, it is also possible that some other thickness between 12 and $20\,\mu m$ would be the optimal target for the ASE conditions of this experiment. Below this optimal thickness, the proton energy begins to decrease. One possible hypothesis is that, for thicknesses below $20\,\mu m$, the shock wave break-out occurs before the main pulse reaches the target. The resulting rear-side plasma and partial target destruction inhibit the accelerating field and reduce the proton energy cutoff. This hypothesis is supported by publications, where even for a small rear plasma scale-length of the order of the laser wavelength ($\sim 1\,\mu m$), a significant negative effect on the generated protons via TNSA was evident [41]. Above $20\,\mu m$, the shock wave does not reach the rear-side in time so no plasma forms and the target is not destroyed. Thus increasing the thickness further acts to reduce the proton cutoff energy. Based on the above observations and hypothesis, for a given set of conditions, there exists some optimal target thickness for which the target is not destroyed and no rear side plasma forms. At this laser energy level and intensity, the expected performance of TNSA ion accelerators (according to experimental data and empirical $I^{1/2}$ scaling laws [28]) is around $30\,\mathrm{MeV}$ protons. The results presented here show much lower maximum energy, far from this standard, which suggests that more improvements are required. The main way to optimize the interaction would be to improve the laser contrast, which would permit use of thinner targets with reduced risk of partial or total target destruction.
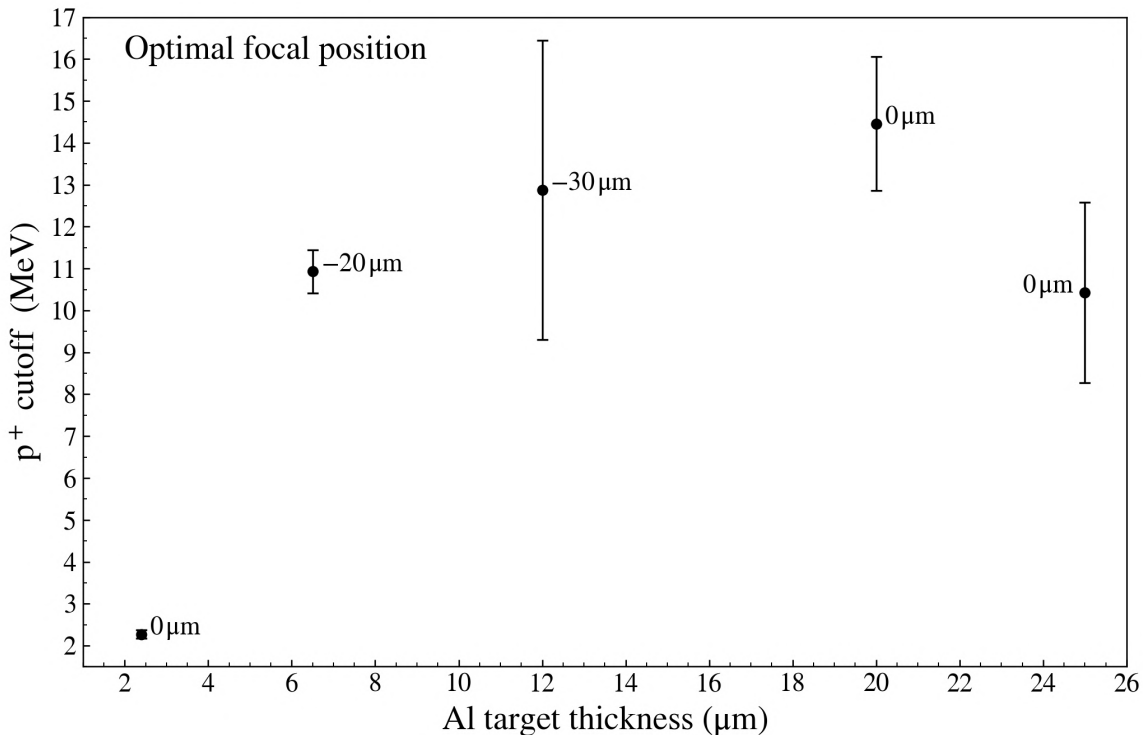
Figure 4.8: Aluminum target thickness vs maximum proton energy for the best focal position in each case. Data from DD1.

Figure 4.8 summarizes the achievements in the optimization of the maximum proton energy. The maximum proton energy that was measured during the commissioning was 14.5 ± 1.5 MeV. The Al target thicknesses that showed the best results were 12 and 20 μm. On the other hand, the energy yield from the 2 μm target was much lower, which suggests that TNSA is inefficient in this case. This could be due to a variety of reasons connected to the effect of the ASE pedestal on the target. The combination of strong ASE pedestal (low laser contrast) and thin target can lead to formation of rear-side plasma and partial target destruction or, in the worst case, total target disintegration if the entire target thickness is reduced to underdense plasma that expands further. Such prepulse effects would certainly justify the poor performance of TNSA for the thinnest target and the sub-optimal maximum proton energy achieved for other thicknesses.

4.4 Theoretical interpretation based on simulations

Experimental data alone cannot provide the full picture of what is happening inside the target during all stages of the interaction. Therefore, the reliability of any conclusions made from experimental data regarding the physics of the interaction and the physical interpretation of the results is limited. Numerical simulations can provide evidence to support or debunk any theory about the data and are a tool frequently used by experimentalists to cross-check real-life experimental results. In order to study and understand laser-driven proton acceleration in the regime of the experiment described above, 2D particle-in-cell simulations were performed using the PIC code Smilei [46]. The main aim of this investigation is two-fold: firstly to identify the ion acceleration mechanism in this experiment and secondly to study the effect of target thickness and rear-side plasma (also known as skirt). The geometry and target chosen for the simulation were simplified (compared to the experiment) in order to speed up the computation while preserving the qualitative features of the interaction. The simulation input file with brief comments is provided in appendix A.

A linearly p-polarized laser pulse with $\lambda = 800\,\text{nm}$ and peak intensity of $10^{21}\,\text{W/cm}^2$ (i.e., with dimensionless pulse amplitude $a_0 = 21.6$) was incident on a target with preplasma in front of a dense thin foil. For simplicity, plasma containing only electrons and protons was used. The density of overdense foil was $30n_{cr}$ (which corresponds to fully ionized hydrogen in the density of solid state), where n_{cr} is the critical density. The scale-length of the exponentially increasing density of preplasma ($n = n_{cr} \times \exp[x/L]$ for $-40\,\mu\text{m} < \text{x} \leq 0\,\mu\text{m}$) was $L = 7\,\mu\text{m}$, until the overdense part of the target with constant maximum density (density plateau) located at $0\,\mu\text{m} < \text{x} < \text{t}_\text{p}$ was reached, where t_p is the plateau thickness. A preplasma of the order of tens of micrometers is typical for nanosecond ASE pedestal [66]. In order to investigate the effect of rear-side plasma ($n = n_{cr} \times \exp[-(x - t_p)/l_p]$), two cases were studied: firstly the case of a step-like profile ($l_p = 0\,\mu\text{m}$) and secondly a short scale-length plasma ($l_p = 1\,\mu\text{m}$), where l_p is the rear-side plasma scale-length. The plasma profile on both front and rear is truncated where $n_e = 0.1\,n_{cr}$. Figure 4.9 shows a 1D slice of the plasma profile used in the simulations.
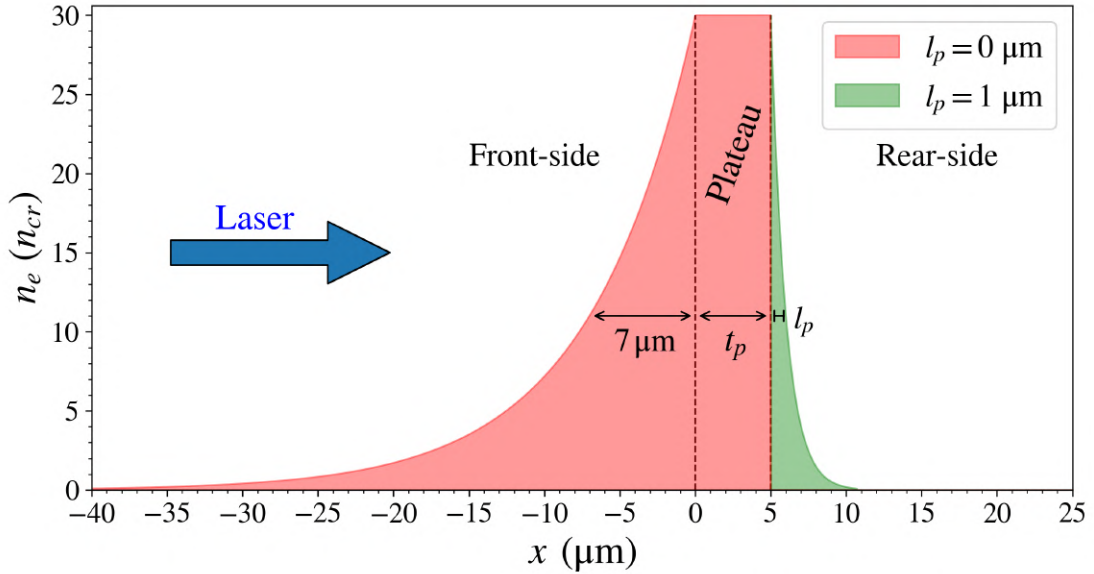

Figure 4.9: Density profile of target in PIC simulations including a step-like rear side ($l_p = 0\,\mu\text{m}$) or a short scale-length plasma ($l_p = 1\,\mu\text{m}$). The preplasma scale-length ($7\,\mu\text{m}$) on the front-side is identical for all simulations. Note that the laser can penetrate beyond the classical critical density $n_e = n_{cr}$ due to relativistic transparency effects.

The size of the grid cell was set to $16\,\text{nm} \times 16\,\text{nm}$, 60 macroparticles per cell were used for the plateau and the preplasma contained an exponentially decreasing number of macroparticles per cell due to its lower density (1 particle per cell at $0.1\,n_{cr}$). The cell size was set to be about 2/3 of the skin depth in order to resolve the relevant physics. The simulation box size was set to $\sim 102\,\mu\text{m} \times 33\,\mu\text{m}$, which means that it contains 6400×2048 cells and a total of ~ 200 million macroparticles, half of which are electrons and half are protons. The macroparticles were initialized at random positions within each cell, with momentum taken from the Maxwell-Jüttner distribution of temperature $3\,\text{keV}$. The dense foil (plateau of maximum density) was placed $55\,\mu\text{m}$ from the left boundary of the box, at the position defined as $x = 0$. A 30 fs (FWHM) Gaussian pulse propagated along the target normal in the x-direction from the left boundary of the box located at $x_{min} = -55\,\mu\text{m}$. The beam had a Gaussian transversal spatial profile with waist projected on the foil surface at position (0,0). The beam waist diameter (intensity FWHM) on the foil surface was set to $5\,\mu\text{m}$ at focus. The total simulation duration was $500\,\text{fs}$ and the timestep was chosen as $0.8\times$CFL condition (30 attoseconds), in order to temporally resolve the propagation of electromagnetic waves through one cell.

Compared with 3D simulations, 2D simulations exhibit artificial heating in the simulation plane because the energy is effectively distributed among only two degrees of freedom. Consequently, the electron density, temperature and sheath field are higher compared to the 3D case, which results in overestimation of the maximum accelerated proton energy by up to 50%. Anyway, 2D simulations still give the correct behaviour, i.e., if a 2D simulation gives a higher energy cutoff for a given set of parameters, this will remain true in 3D. In summary, a 2D simulation cannot be used directly for quantitative comparison with experimental data, but rather only as a tool to qualitatively understand the interaction and compare different sets of parameters [67, 68, 69].
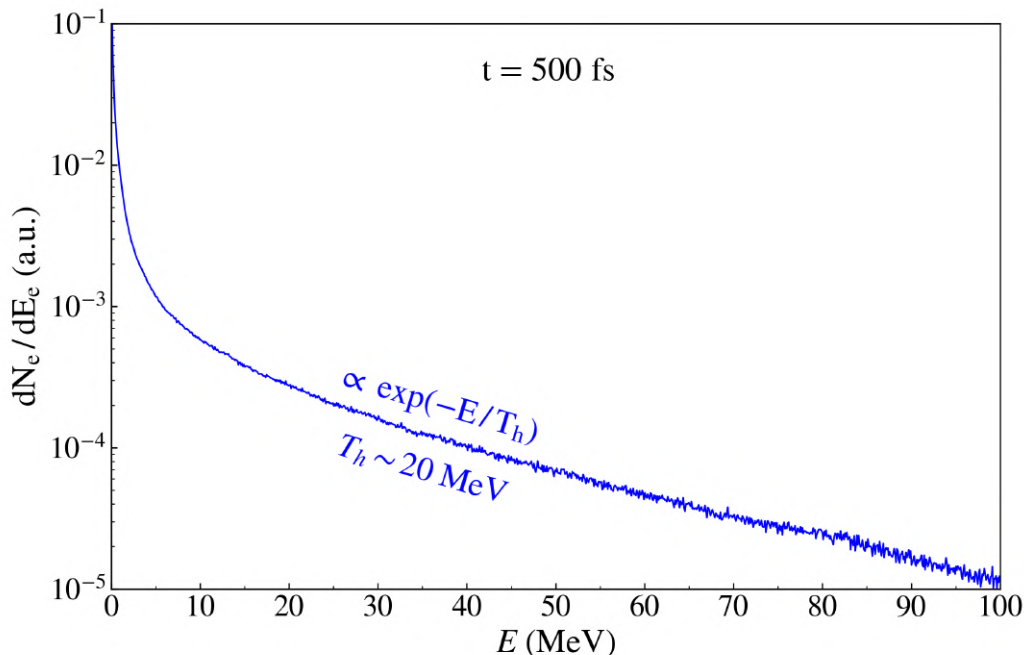

Figure 4.10: Energy distribution of electrons accelerated in the forward direction.

Three different simulations were carried out with the aim to understand the effect of rear-side plasma scale-length l_p and target thickness t_p. The preplasma was the same in all cases and therefore electron heating was found to be identical. The electron energy spectrum is roughly the same for all simulations (because these electrons are generated inside the preplasma which has the same parameters for all simulations) and is shown in figure 4.10. From the Maxwell-Boltzmann law, the hot electron temperature is calculated to be $\sim 20\,\mathrm{MeV}$, around 3 times greater that the temperature predicted by the ponderomotive scaling equation (1.20). This discrepancy is partially due to 2D effects but mostly due to stochastic heating which is able to heat electrons above ponderomotive scaling [11]. Note that all simulations were performed using 0° angle of incidence, although it was verified using an independent simulation that changing the angle to 15° (as in the experiment) did not make any difference to the results, either qualitatively or quantitatively.

The ion acceleration mechanism was identified as TNSA. Signs for the presence of TNSA can be found both in figure 4.11, which shows the longitudinal electric field at 5 time instants for the case of a $5\,\mu$m target with $1\,\mu$m scale-length rear plasma, and in figure 4.12, which shows the balance between kinetic and electromagnetic energy inside the simulation box. Looking first at figure 4.11, the top panel shows the laser pulse entering the simulation box. In panel 2, the ponderomotive force in front of the pulse pushes electrons in the preplasma and creates a charge-separation field which can accelerate protons. In panel 3, the pulse has reached the relativistically overdense plasma and hot electrons propagate to the right.
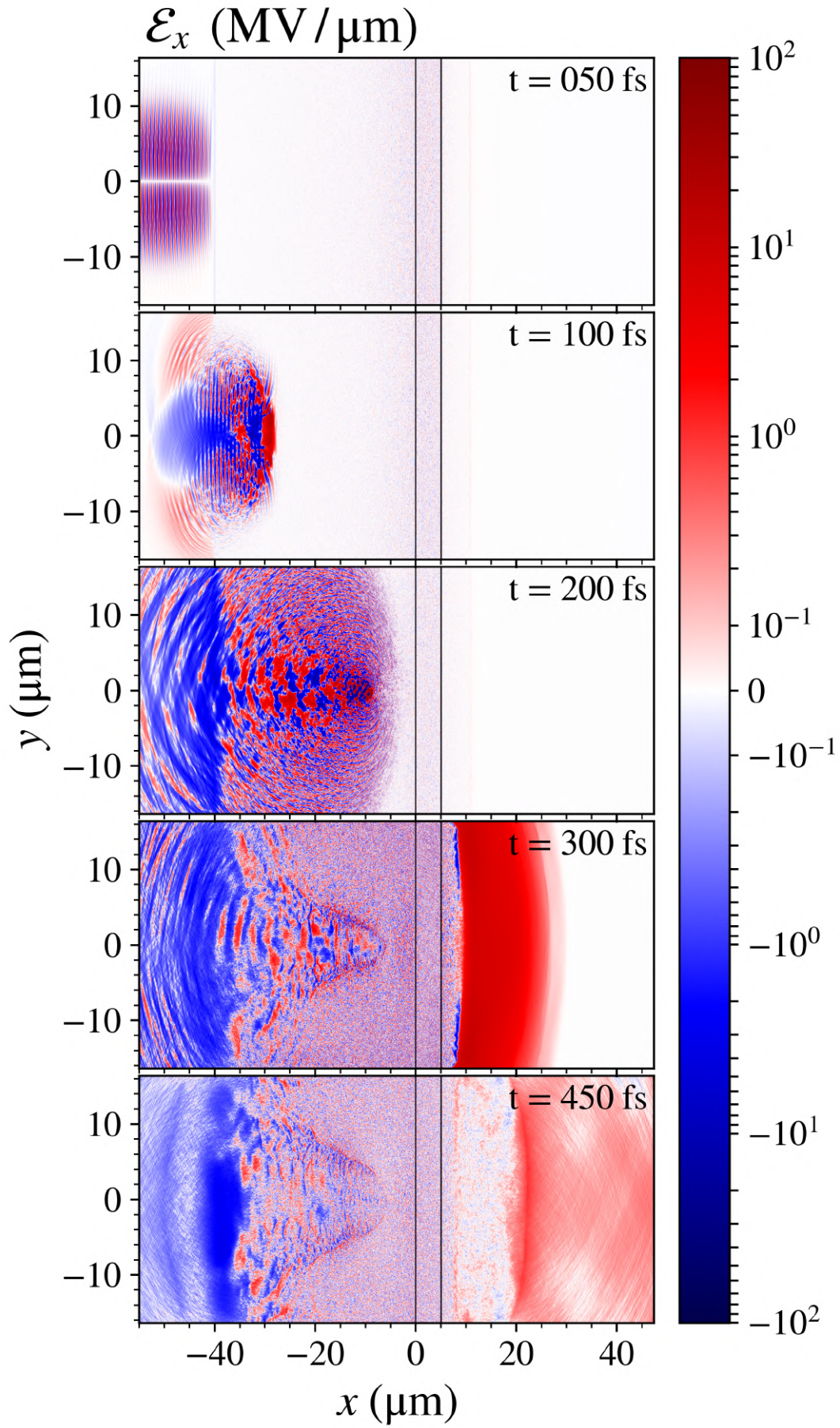
Figure 4.11: Time development of the longitudinal electric field $\mathcal{E}_x$.

In panel 4, the hot electrons generated in the preplasma escape into vacuum from the target rear and setup a strong quasi-static accelerating sheath field which accelerates protons from the rear surface of the target. Finally, panel 5 shows the proton ion front moving to the right. Figure 4.11 clearly depicts the whole process of TNSA. The energy balance in figure 4.12 shows that between $100 - 200\,$fs the electromagnetic energy is transferred to hot electron kinetic energy in the preplasma. These electrons then escape into the vacuum behind the target at different times, depending on target thickness and the presence or not of plasma on the rear. When they escape, charge neutrality is violated and an electric field is generated. Therefore, some of the electron kinetic energy is transferred to this quasi-static field (electromagnetic energy bump between $250 - 300\,$fs), which is in turn used to accelerate protons. In summary, laser energy is coupled to hot electrons in preplasma which transfer part of their energy to protons by the charge-separation field on the target rear side.
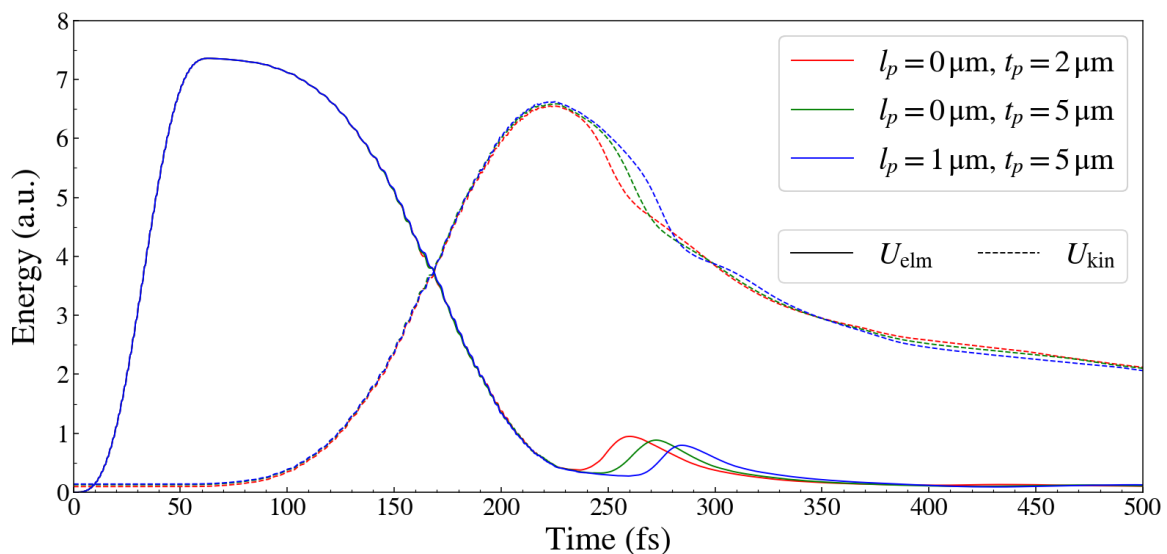

Figure 4.12: Energy balance inside the simulation box for the 3 simulation cases: (red) $2\,\mu$m target without skirt, (green) $5\,\mu$m target without skirt and (blue) $5\,\mu$m target with short scale-length plasma on rear.

Figure 4.13 shows the energy spectra of protons accelerated by the TNSA mechanism from the target rear side. The three cases correspond to: (red) $2\,\mu$m target without skirt, (green) $5\,\mu$m target without skirt and (blue) $5\,\mu$m target with short plasma on rear. It is apparent that even a short plasma on the rear-side has a detrimental effect on acceleration by the TNSA mechanism, with the proton cutoff energy decreasing almost by half. The explanation for this difference in energy in demonstrated in figure 4.14. This figure shows a 1D slice of the accelerating field at the time instant when the field reaches its maximum value. The difference in the field between the two cases suggests that the plasma on the rear hinders the accelerating field and decreases its maximum value. On the other hand, a thinner target appears to significantly enhance the proton energy cutoff. This behaviour can be explained by considering the electron beam divergence, which results in lower electron density after propagation through thick targets. The effect of hot electron re-circulation should not be so important in this case due to the presence of the front-side preplasma instead of vacuum. For completeness, proton acceleration from the front side is also observed but produces less energetic protons. There is acceleration of protons inside the preplasma in the forward direction (ponderomotive acceleration of electrons creates charge separation field which accelerates protons to $7\,$MeV cutoff) and there are also backward accelerated protons ($17\,$MeV cutoff).
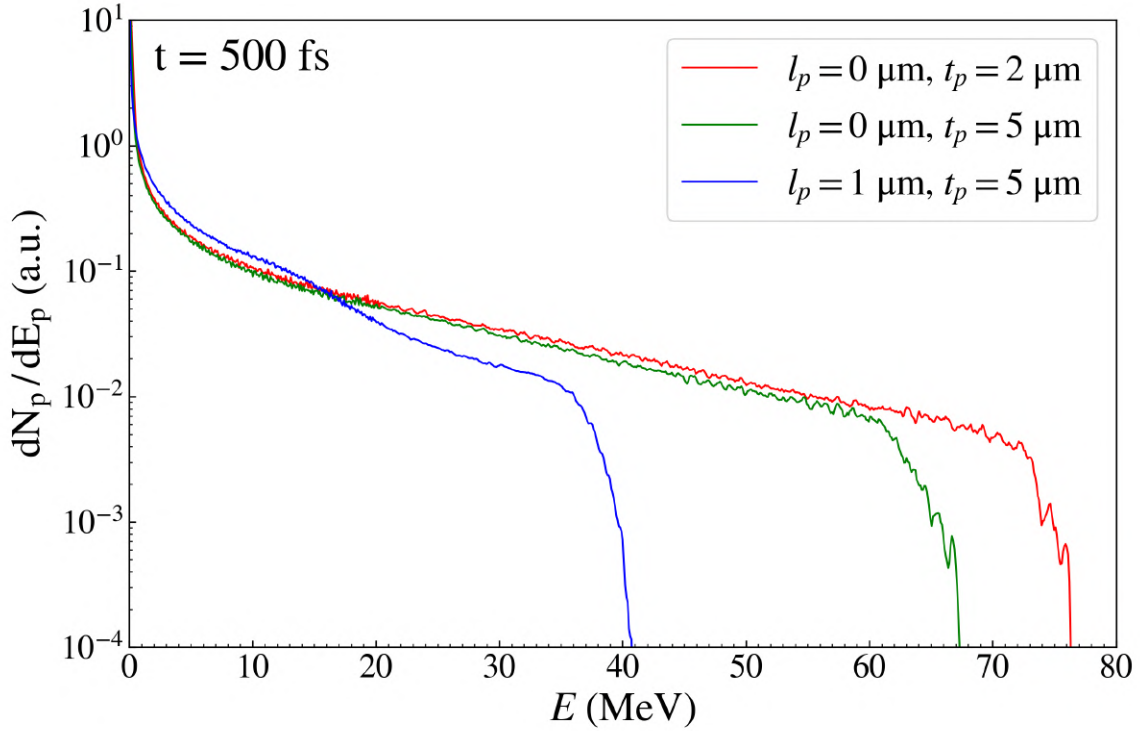
Figure 4.13: Energy spectra of protons accelerated from the target rear-side in the forward direction. The three cases correspond to: (red) $2\,\mu$m target without skirt, (green) $5\,\mu$m target without skirt and (blue) $5\,\mu$m target with short plasma on rear.
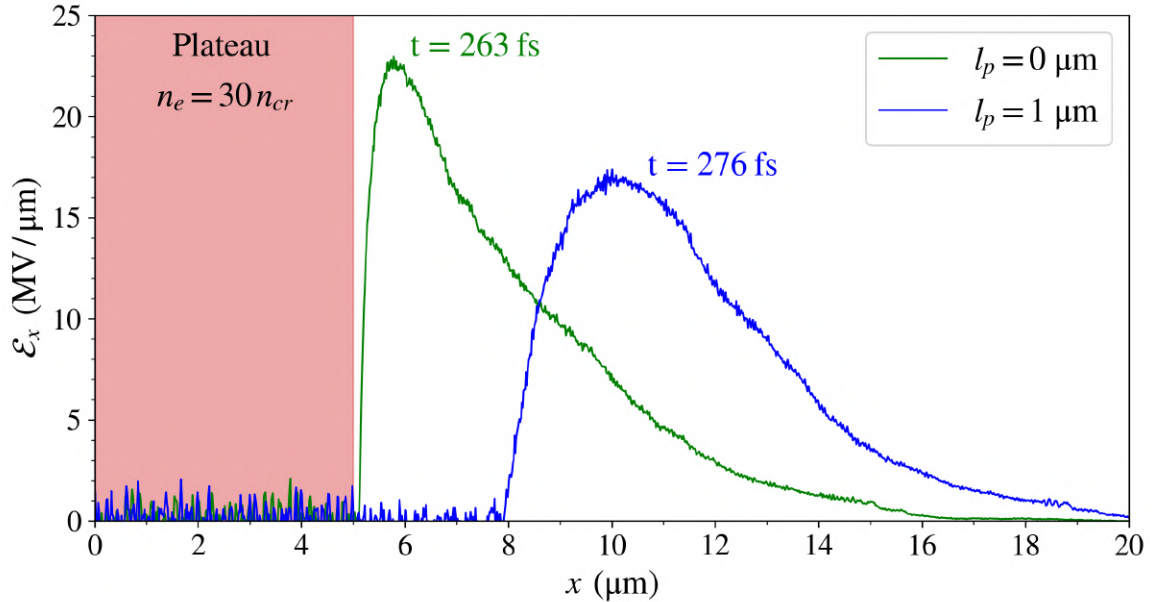
Figure 4.14: Maximum accelerating field on the rear-side of a $5\,\mu$m target for the case of rear plasma (blue) and no rear plasma (green). The curves are 1D snapshots of the fields at the time instants when they reach their maximum value. Plasma inhibits the rear accelerating field and lowers its maximum value.

Conclusion

This thesis has demonstrated the critical importance of target thickness, focal position and rear-side plasma for the TNSA ion acceleration mechanism. In particular, the significance of improving the laser prepulse characteristics and laser contrast for the ELIMAIA ion accelerator has been stressed, since even short scale-length plasma on the target rear (created by the shock wave triggered by the prepulse) has severe negative impact on the accelerating fields and, thus, on the maximum ion energy. The evidence suggests that rear-side plasma is likely present for Aluminum targets as thick as $\sim 20\,\mu$m. Despite this obstacle, the experimental results from the ELIMAIA ion accelerator commissioning are very promising, with protons of maximum energy 14.5 ± 1.5 MeV being detected by numerous diagnostics, including semiconductor time-of-flight detectors and Thomson parabola spectrometer. Moreover, the total proton flux measured was $(1.5 \pm 0.5) \times 10^{11}$ p$^+$/shot/sr. However, this performance is not close to the proton cutoff energy expected by empirical scaling laws for the laser energy and intensity levels used in the commissioning. According to data from other experiments and empirical $I^{1/2}$ scaling laws [28], the maximum proton energy is expected to be around 30 MeV. This means that more work is still required in order to optimize the laser-target interaction and improve the performance of the ELIMAIA ion accelerator (laser contrast improvements and better target optimization - target thickness and material type selection).

Although the effects of target thickness and rear-side plasma have been investigated in previous studies, this work remains relevant because it verifies the existing theoretical understanding but for the particular set of experimental condition used at the ELIMAIA ion accelerator. Therefore, it provides insight into the laser-plasma interaction and can be used to inform future steps to improve and optimize the performance of this laser-driven beamline. In the following years, the field of laser-driven ion acceleration will mature and multidisciplinary applications will begin to test the potential of this technology. The ELIMAIA beamline, with its unique capabilities and user-oriented approach, is set to lead the scientific community into a future where laser-driven beamlines will have a prominent place in industry and society. The author firmly believes that the work presented in this thesis will facilitate the further advancement of the ELIMAIA ion accelerator and contribute to improved understanding of the TNSA mechanism as a whole.

Appendix A

Smilei input code

The input Python script with some brief comments explaining the different parameters is presented below. For more details on the available options and diagnostic tools please refer to the online Smilei documentation at https://smileipic.github.io/Smilei/ and article [46].

```python
# ----------------------------------------------------------------------------
#                 SIMULATION PARAMETERS FOR THE PIC-CODE SMILEI
# ----------------------------------------------------------------------------

import numpy as np


# CONSTANTS
################################################################################
l0 = 2.0*np.pi                  # wavelength [code units] ; (= 800 nm)
t0 = 2.0*np.pi                  # optical period [code units] ; (= 2.66 fs)

Lsimx = 128.*l0                 # length of the simulation box in x (= 102.4 um)
Lsimy = 40.96*l0                # length of the simulation box in y (= 32.768 um)
Tsim = 187.51*t0                # duration of the simulation (= 500 fs)

resx = 50.                      # nb of cells per wavelength in x
resy = 50.                      # nb of cells per wavelength in y
rest = resx/0.8                 # nb of timesteps in one optical period
dt = t0/rest/np.sqrt(2.0)       # time step [code units] ; (= 0.03017 fs)

ne = 30.0                       # electron density [code units]
Te = 0.00587                    # electron thermal energy [code units] ; (= 3 KeV)
nppc = 60                       # number of particles-per-cell
mp = 1836.                      # proton mass [code units]

FWHMinI = 6.25*l0               # gaussian beam waist [code units] ; (= 5 um)
waistinI = FWHMinI/(2.0*np.sqrt(np.log(2.0)))
waistinE = FWHMinI/np.sqrt(2.0*np.log(2.0))

FWHMtinI = 11.25*t0             # pulse duration [code units] ; (= 30 fs)
FWHMtinE = FWHMtinI*np.sqrt(2.0)

diagEvery  = int(3.75*t0/dt) # frequency of outputs for DiagField (= 10 fs)
################################################################################
```

```python
# INITIAL DENSITY PROFILE
################################################################################
l1 = 8.75*l0           # exp preplasma scale-length = 7 um
l2 = 1.25*l0           # exp skirt scale-length = 1 um
plaS = 68.75*l0        # plateau start
total_pla = 6.25*l0    # plateau tkickness = 5 um
plaE = plaS+total_pla  # plateau end

cutoff1 = plaS - l1*np.log(10*ne) # preplasma cutoff at 0.1 nc
cutoff2 = plaE + l2*np.log(10*ne) # skirt cutoff at 0.1 nc

p1 = (plaS - cutoff1)/np.log(nppc) # preplasma ppc scale-length
p2 = (cutoff2 - plaE)/np.log(nppc) # skirt ppc scale-length

def ndens(x,y):
    D = np.zeros(x.shape)
    mask1 = (x>=cutoff1) & (x<plaS) # preplasma mask
    mask2 = (x>=plaS) & (x<plaE)    # plateau mask
    mask3 = (x>=plaE) & (x<cutoff2) # skirt mask
    D[mask1] = ne*np.exp((x[mask1]-plaS)/l1)
    D[mask2] = ne
    D[mask3] = ne*np.exp((plaE-x[mask3])/l2)
    return D

def ppc(x,y):
    P = np.zeros(x.shape)
    mask1 = (x>=cutoff1) & (x<plaS) # preplasma mask
    mask2 = (x>=plaS) & (x<plaE)    # plateau mask
    mask3 = (x>=plaE) & (x<cutoff2) # skirt mask
    P[mask1] = nppc*np.exp((x[mask1]-plaS)/p1)
    P[mask2] = nppc
    P[mask3] = nppc*np.exp((plaE-x[mask3])/p2)
    return P
################################################################################



# DEFINING SMILEI's VARIABLES
# All in "blocks"
# -------------------------
################################################################################

Main(
    geometry = "2Dcartesian",
    interpolation_order = 4,
    timestep = dt,
    simulation_time = Tsim,
    cell_length = [l0/resx,l0/resy],
    grid_length = [Lsimx,Lsimy],
    number_of_patches = [256,64],
    EM_boundary_conditions = [ ["silver-muller","silver-muller"],
                               ["silver-muller","silver-muller"] ],
    print_every = 50,
    random_seed = 0
)
```

```python
Species(
    name = "electron",
    position_initialization = "random",
    momentum_initialization = "maxwell-juettner",
    particles_per_cell = ppc,
    mass = 1.0,
    charge = -1.0,
    number_density = ndens,
    temperature = [Te],
    thermal_boundary_temperature = [Te],
    boundary_conditions = [ ["remove"], ["thermalize"] ],
)




Species(
    name = "proton",
    position_initialization = "random",
    momentum_initialization = "maxwell-juettner",
    particles_per_cell = ppc,
    mass = mp,
    charge = 1.0,
    number_density = ndens,
    temperature = [Te],
    thermal_boundary_temperature = [Te],
    boundary_conditions = [ ["remove"], ["thermalize"] ],
)




LaserGaussian2D(
    box_side       = "xmin",
    a0             = 21.61, # peak intensity 1e21
    omega          = 1.,
    focus          = [plaS, Main.grid_length[1]/2.],
    waist          = waistinE,
    incidence_angle = 0.,
    polarization_phi = 0.,
    ellipticity    = 0.,
    time_envelope = tcosine(base=0., start=0., duration=24.*t0,
                            phi=np.pi/2., freq=1./(24.0*2.0))
)




LoadBalancing(
    initial_balance = True,
    every = 50
)
##########################################################################
```

```python
# DIAGNOSTICS
##############################################################################

DiagScalar(
    every = 10,
    vars = ["Utot", "Ukin", "Uelm"]
)


DiagFields(
    every = diagEvery,
    fields = ["Ex","Ey","Rho_electron","Rho_proton"]
)


DiagParticleBinning(
    deposited_quantity = "weight",
    every = diagEvery,
    time_average = 1,
    species = ["electron"],
    axes = [ ["x",0,Lsimx,1000],
             ["ekin", 0., 200., 1000] ]
)


DiagParticleBinning(
    deposited_quantity = "weight",
    every = diagEvery,
    time_average = 1,
    species = ["proton"],
    axes = [ ["x",0,Lsimx,1000],
             ["ekin", 0., 200., 1000] ]
)


DiagScreen(
    deposited_quantity = "weight",
    every = diagEvery,
    shape = "plane",
    point = [plaS+total_pla/2, Main.grid_length[1]/2.],
    vector = [1., 0.],
    direction = "forward",
    species = ["electron"],
    axes = [ ["ekin", 0., 200., 1000] ]
)
##############################################################################
```

Bibliography

[1] D. Margarone, G. Cirrone, G. Cuttone, A. Amico, L. Andò, M. Borghesi, S. S. Bulanov, S. V. Bulanov, D. Chatain, A. Fajstavr, *et al.*, "Elimaia: A laser-driven ion accelerator for multidisciplinary applications," *Quantum Beam Science*, vol. 2, no. 2, p. 8, 2018.

[2] A. Macchi, M. Borghesi, and M. Passoni, "Ion acceleration by superintense laser-plasma interaction," *Reviews of Modern Physics*, vol. 85, no. 2, p. 751, 2013.

[3] L. Keldysh *et al.*, "Ionization in the field of a strong electromagnetic wave," *Sov. Phys. JETP*, vol. 20, no. 5, pp. 1307–1314, 1965.

[4] P. Gibbon, *Short pulse laser interactions with matter: an introduction.* World Scientific, 2005.

[5] K. Amini, J. Biegert, F. Calegari, A. Chacón, M. F. Ciappina, A. Dauphin, D. K. Efimov, C. F. de Morisson Faria, K. Giergiel, P. Gniewek, *et al.*, "Symphony on strong field approximation," *Reports on Progress in Physics*, vol. 82, no. 11, p. 116001, 2019.

[6] P. Mulser and D. Bauer, *High power laser-matter interaction*, vol. 238. Springer, 2010.

[7] A. Macchi, *A superintense laser-plasma interaction theory primer.* Springer Science & Business Media, 2013.

[8] R. Fitzpatrick, *Plasma physics: an introduction.* Crc Press, 2014.

[9] S. Eliezer, *The interaction of high-power lasers with plasmas.* CRC press, 2002.

[10] R. W. Boyd, *Nonlinear optics.* Academic press, 2020.

[11] R. Babjak and J. Pšikal, "The role of standing wave in the generation of hot electrons by femtosecond laser beams incident on dense ionized target," *Physics of Plasmas*, vol. 28, no. 2, p. 023107, 2021.

[12] H. Daido, M. Nishiuchi, and A. S. Pirozhkov, "Review of laser-driven ion sources and their applications," *Reports on progress in physics*, vol. 75, no. 5, p. 056401, 2012.

[13] H.-P. Schlenvoigt, O. Jäckel, S. M. Pfotenhauer, and M. C. Kaluza, "Laser-based particle acceleration," in *Advances in Solid State Lasers Development and Applications*, IntechOpen, 2010.

[14] F. Brunel, "Not-so-resonant, resonant absorption," *Physical review letters*, vol. 59, no. 1, p. 52, 1987.

[15] S. Wilks, W. Kruer, M. Tabak, and A. Langdon, "Absorption of ultra-intense laser pulses," *Physical review letters*, vol. 69, no. 9, p. 1383, 1992.

[16] G. Malka and J. Miquel, "Experimental confirmation of ponderomotive-force electrons produced by an ultrarelativistic laser pulse on a solid target," *Physical review letters*, vol. 77, no. 1, p. 75, 1996.

[17] A. Pukhov, Z.-M. Sheng, and J. Meyer-ter Vehn, "Particle acceleration in relativistic laser channels," *Physics of Plasmas*, vol. 6, no. 7, pp. 2847–2854, 1999.

[18] A. Pukhov, "Strong field interaction of laser radiation," *Reports on progress in Physics*, vol. 66, no. 1, p. 47, 2002.

[19] A. Arefiev, V. Khudik, A. Robinson, G. Shvets, L. Willingale, and M. Schollmeier, "Beyond the ponderomotive limit: Direct laser acceleration of relativistic electrons in sub-critical plasmas," *Physics of Plasmas*, vol. 23, no. 5, p. 056704, 2016.

[20] J. Pšikal, V. Tikhonchuk, J. Limpouch, A. Andreev, and A. Brantov, "Ion acceleration by femtosecond laser pulses in small multispecies targets," *Physics of Plasmas*, vol. 15, no. 5, p. 053102, 2008.

[21] J. Pšikal, *Ion Acceleration in Small-size Targets by Ultra-intense Short Laser Pulses (Simulation and Theory)*. PhD thesis, Bordeaux, ČVUT (Prague), 2009.

[22] S. V. Bulanov, J. J. Wilkens, T. Z. Esirkepov, G. Korn, G. Kraft, S. D. Kraft, M. Molls, and V. S. Khoroshkov, "Laser ion acceleration for hadron therapy," *Physics-Uspekhi*, vol. 57, no. 12, p. 1149, 2014.

[23] K. Lezhnin, F. Kamenets, V. Beskin, M. Kando, T. Z. Esirkepov, and S. Bulanov, "Effect of electromagnetic pulse transverse inhomogeneity on ion acceleration by radiation pressure," *Physics of Plasmas*, vol. 22, no. 3, p. 033112, 2015.

[24] S. Wilks, A. Langdon, T. Cowan, M. Roth, M. Singh, S. Hatchett, M. Key, D. Pennington, A. MacKinnon, and R. Snavely, "Energetic proton generation in ultra-intense laser–solid interactions," *Physics of plasmas*, vol. 8, no. 2, 2001.

[25] P. G. Thirolf, "Particle acceleration driven by high-power, short pulse lasers," in *The Euroschool on Exotic Beams-Vol. 5*, pp. 255–292, Springer, 2018.

[26] O. Klimo, *Simulations of Ultrashort-Pulse Laser Solid-Target Interactions*. PhD thesis, ČVUT (Prague), 2007.

[27] P. Mora, "Plasma expansion into a vacuum," *Physical Review Letters*, vol. 90, no. 18, p. 185002, 2003.

[28] M. Zimmer, S. Scheuren, T. Ebert, G. Schaumann, C. Rödel, M. Roth, B. Schmitz, V. Bagnoud, and J. Hornung, "Analysis of laser-proton acceleration experiments for development of empirical scaling laws," *Physical Review E*, vol. 104, no. 4, 2021.

[29] Y. Sentoku, T. Cowan, A. Kemp, and H. Ruhl, "High energy proton acceleration in interaction of short laser pulse with dense plasma target," *Physics of plasmas*, vol. 10, no. 5, pp. 2009–2015, 2003.

[30] D. Batani, R. Jafer, M. Veltcheva, R. Dezulian, O. Lundh, F. Lindau, A. Persson, K. Osvay, C. Wahlström, D. Carroll, *et al.*, "Effects of laser prepulses on laser-induced proton generation," *New Journal of Physics*, vol. 12, no. 4, p. 045018, 2010.

[31] T. Esirkepov, M. Borghesi, S. Bulanov, G. Mourou, and T. Tajima, "Highly efficient relativistic-ion generation in the laser-piston regime," *Physical review letters*, vol. 92, no. 17, p. 175003, 2004.

[32] O. Klimo, J. Pšikal, J. Limpouch, and V. Tikhonchuk, "Monoenergetic ion beams from ultrathin foils irradiated by ultrahigh-contrast circularly polarized laser pulses," *Physical Review Special Topics-Accelerators and Beams*, vol. 11, no. 3, 2008.

[33] D. Strickland and G. Mourou, "Compression of amplified chirped optical pulses," *Optics communications*, vol. 55, no. 6, pp. 447–449, 1985.

[34] P. Maine, D. Strickland, P. Bado, M. Pessot, and G. Mourou, "Generation of ultrahigh peak power pulses by chirped pulse amplification," *IEEE Journal of Quantum electronics*, vol. 24, no. 2, pp. 398–403, 1988.

[35] S. A. Reed, T. Matsuoka, S. Bulanov, M. Tampo, V. Chvykov, G. Kalintchenko, P. Rousseau, V. Yanovsky, R. Kodama, D. W. Litzenberg, *et al.*, "Relativistic plasma shutter for ultraintense laser pulses," *Applied physics letters*, vol. 94, no. 20, p. 201117, 2009.

[36] M. Zhou, J. Bin, D. Haffa, X. Yan, and J. Schreiber, "The impact of femtosecond pre-pulses on nanometer thin foils for laser-ion acceleration," *Plasma Physics and Controlled Fusion*, vol. 59, no. 5, p. 055020, 2017.

[37] F. Wagner, C. Brabetz, O. Deppert, M. Roth, T. Stöhlker, A. Tauschwitz, A. Tebartz, B. Zielbauer, and V. Bagnoud, "Accelerating ions with high-energy short laser pulses from submicrometer thick targets," *High power laser science and engineering*, vol. 4, 2016.

[38] E. G. Gamaly, A. V. Rode, B. Luther-Davies, and V. T. Tikhonchuk, "Ablation of solids by femtosecond lasers: Ablation mechanism and ablation thresholds for metals and dielectrics," *Physics of plasmas*, vol. 9, no. 3, pp. 949–957, 2002.

[39] T. Z. Esirkepov, J. K. Koga, A. Sunahara, T. Morita, M. Nishikino, K. Kageyama, H. Nagatomo, K. Nishihara, A. Sagisaka, H. Kotaki, *et al.*, "Prepulse and amplified spontaneous emission effects on the interaction of a petawatt class laser with thin solid targets," *Nuclear Instruments and Methods in Physics Research Section A: Accelerators, Spectrometers, Detectors and Associated Equipment*, vol. 745, pp. 150–163, 2014.

[40] L. A. Gizzi, E. Boella, L. Labate, F. Baffigi, P. J. Bilbao, F. Brandi, G. Cristoforetti, A. Fazzi, L. Fulgentini, D. Giove, *et al.*, "Enhanced laser-driven proton acceleration via improved fast electron heating in a controlled pre-plasma," *arXiv preprint arXiv:2106.00814*, 2021.

[41] A. Higginson, R. Wilson, J. Goodman, M. King, R. Dance, N. Butler, C. Armstrong, M. Notley, D. Carroll, Y. Fang, *et al.*, "Influence of target-rear-side short scale length density gradients on laser-driven proton acceleration," *Plasma Physics and Controlled Fusion*, vol. 63, no. 11, p. 114001, 2021.

[42] P. McKenna, D. Neely, R. Bingham, and D. Jaroszynski, *Laser-plasma interactions and applications.* Springer, 2013.

[43] Y. L. Klimontovich, *The Statistical Theory of Non-Equilibrium Processes in a Plasma.* Pergamon Press, 1967.

[44] D. R. Nicholson and D. R. Nicholson, *Introduction to plasma theory*, vol. 582. Wiley New York, 1983.

[45] T. Arber, K. Bennett, C. Brady, A. Lawrence-Douglas, M. Ramsay, N. Sircombe, P. Gillies, R. Evans, H. Schmitz, A. Bell, *et al.*, "Contemporary particle-in-cell approach to laser-plasma modelling," *Plasma Physics and Controlled Fusion*, vol. 57, no. 11, p. 113001, 2015.

[46] J. Derouillat, A. Beck, F. Pérez, T. Vinci, M. Chiaramello, A. Grassi, M. Flé, G. Bouchard, I. Plotnikov, N. Aunai, *et al.*, "Smilei: A collaborative, open-source, multi-purpose particle-in-cell code for plasma simulation," *Computer Physics Communications*, vol. 222, pp. 351–373, 2018.

[47] H. Ueda, Y. Omura, H. Matsumoto, and T. Okuzawa, "A study of the numerical heating in electrostatic particle simulations," *Computer physics communications*, vol. 79, no. 2, pp. 249–259, 1994.

[48] C. K. Birdsall and A. B. Langdon, *Plasma physics via computer simulation*. CRC press, 2018.

[49] T. Z. Esirkepov, "Exact charge conservation scheme for particle-in-cell simulation with an arbitrary form-factor," *Computer Physics Communications*, vol. 135, no. 2, pp. 144–153, 2001.

[50] K. Yee, "Numerical solution of initial boundary value problems involving maxwell's equations in isotropic media," *IEEE Transactions on antennas and propagation*, vol. 14, no. 3, pp. 302–307, 1966.

[51] A. Girard, D. Margarone, P. Bonnay, S. Michaux, N. Luchier, and D. Chatain, "Cryogenic hydrogen targets for proton beam generation with ultra-intense lasers.," in *IOP Conference Series: Materials Science and Engineering*, vol. 502, p. 012160, IOP Publishing, 2019.

[52] D. Margarone, J. Krása, L. Giuffrida, A. Picciotto, L. Torrisi, T. Nowak, P. Musumeci, A. Velyhan, J. Prokůpek, L. Láska, *et al.*, "Full characterization of laser-accelerated ion beams using faraday cup, silicon carbide, and single-crystal diamond detectors," *Journal of Applied Physics*, vol. 109, no. 10, p. 103302, 2011.

[53] G. Milluzzo, V. Scuderi, A. Alejo, A. Amico, N. Booth, M. Borghesi, G. Cirrone, G. Cuttone, D. Doria, J. Green, *et al.*, "A new energy spectrum reconstruction method for time-of-flight diagnostics of high-energy laser-driven protons," *Review of Scientific Instruments*, vol. 90, no. 8, p. 083303, 2019.

[54] J. Krása, "Gaussian energy distribution of fast ions emitted by laser-produced plasmas," *Applied surface science*, vol. 272, pp. 46–49, 2013.

[55] E. Woryna, P. Parys, J. Wołowski, and W. Mroz, "Corpuscular diagnostics and processing methods applied in investigations of laser-produced plasma as a source of highly ionized ions," *Laser and Particle beams*, vol. 14, no. 3, pp. 293–321, 1996.

[56] J. F. Ziegler, M. D. Ziegler, and J. P. Biersack, "Srim–the stopping and range of ions in matter (2010)," *Nuclear Instruments and Methods in Physics Research Section B: Beam Interactions with Materials and Atoms*, vol. 268, no. 11-12, pp. 1818–1823, 2010.

[57] R. Prasad, D. Doria, S. Ter-Avetisyan, P. Foster, K. Quinn, L. Romagnani, C. Brenner, J. Green, P. Gallegos, M. Streeter, *et al.*, "Calibration of thomson parabola—mcp assembly for multi-mev ion spectroscopy," *Nuclear Instruments and Methods in Physics Research Section A: Accelerators, Spectrometers, Detectors and Associated Equipment*, vol. 623, no. 2, pp. 712–715, 2010.

[58] A. Bhagwat, "Solid state nuclear track detection: Theory and applications," tech. rep., Indian Society for Radiation Physics, 1993.

[59] Y. Zhang, H.-W. Wang, Y.-G. Ma, L.-X. Liu, X.-G. Cao, G.-T. Fan, G.-Q. Zhang, and D.-Q. Fang, "Energy calibration of a cr-39 nuclear-track detector irradiated by charged particles," *Nuclear Science and Techniques*, vol. 30, no. 6, pp. 1–9, 2019.

[60] D. Margarone, A. Morace, J. Bonvalet, Y. Abe, V. Kantarelou, D. Raffestin, L. Giuffrida, P. Nicolai, M. Tosca, A. Picciotto, *et al.*, "Generation of α-particle beams with a multi-kj, peta-watt class laser system," *Frontiers in Physics*, p. 343, 2020.

[61] M. Williams and P. Metcalfe, "Radiochromic film dosimetry and its applications in radiotherapy," in *AIP Conference Proceedings*, vol. 1345, pp. 75–99, American Institute of Physics, 2011.

[62] C. G. Soares, "Radiochromic film dosimetry," *Radiation Measurements*, vol. 41, pp. S100–S116, 2006. The 2nd Summer School on Solid State Dosimetry: Concepts and Trends in Medical Dosimetry.

[63] G. S. Hicks, N. P. Dover, R. Nichols, P. Posocco, Z. Najmudin, and J. S. Green, "Proton spectra calculation from Radiochromic Film stacks with high-energy proton correction," tech. rep.

[64] B. Rus, P. Bakule, D. Kramer, J. Naylon, J. Thoma, M. Fibrich, J. Green, J. Lagron, R. Antipenkov, J. Bartoníček, *et al.*, "Eli-beamlines: progress in development of next generation short-pulse laser systems," in *Research Using Extreme Light: Entering New Frontiers with Petawatt-Class Lasers III*, vol. 10241, pp. 14–21, SPIE, 2017.

[65] L. Torrisi, D. Margarone, L. Laska, J. Krasa, A. Velyhan, M. Pfeifer, J. Ullschmied, and L. Ryc, "Self-focusing effect in au-target induced by high power pulsed laser at pals," *Laser and Particle Beams*, vol. 26, no. 3, pp. 379–387, 2008.

[66] F. Wagner, S. Bedacht, A. Ortner, M. Roth, A. Tauschwitz, B. Zielbauer, and V. Bagnoud, "Pre-plasma formation in experiments using petawatt lasers," *Optics Express*, vol. 22, no. 24, pp. 29505–29514, 2014.

[67] D. J. Stark, L. Yin, B. J. Albright, and F. Guo, "Effects of dimensionality on kinetic simulations of laser-ion acceleration in the transparency regime," *Physics of Plasmas*, vol. 24, no. 5, p. 053103, 2017.

[68] J.-L. Liu, M. Chen, J. Zheng, Z.-M. Sheng, and C.-S. Liu, "Three dimensional effects on proton acceleration by intense laser solid target interaction," *Physics of Plasmas*, vol. 20, no. 6, p. 063107, 2013.

[69] A. Héron, J. Adam, and P. Mora, "Generation of ultra-energetic ions by interaction of petawatt lasers with micrometer-scale foils," *Physics of Plasmas*, vol. 27, no. 1, p. 013103, 2020.